THE ANALYSIS, SIMULATION AND TESTING OF AN EXPERIMENTAL TRAVELLING-WAVE TUBE

by

CHRISTOPHER GARTH REYNOLDS

submitted in partial fulfilment of the
requirements for the degree of

DOCTOR OF PHILOSOPHY

in the Faculty of Electronic Engineering
in the University of Natal, Durban,
SOUTH AFRICA

May, 1994

ABSTRACT

As a design and analysis aid for the development of an experimental TWT, a computer program is written which allows the small-signal gain to be computed for various operating conditions, such as various conditions of tube bias (beam voltage and current) and frequency. In order to arrive at a value for the gain, a number of parameters need first to be defined or calculated.

Using the method (Approach II) of Jain and Basu [17] which is applicable to a helix with a free-space gap between it and circular dielectric support rods surrounded by a metal shell, the dielectric loading factor (DLF) for the structure is found and the dispersion relation then solved to obtain the radial propagation constant γ and axial propagation constant β. The method is tested for a helix with measured data and found to be acceptably accurate.

Helix losses are calculated for the low-loss input and output sections of the helix, using the procedures developed by Gilmour *et al* [14,18], from which values are found for the helix loss parameter d. Another value for d, obviously much larger, is also found for the lossy attenuator section of the helix. Here measured data for the attenuator is used as a basis for a polynomial which models the attenuator loss as a function of frequency.

The Pierce gain parameter C is found using the well-known equations of Pierce [21,22,26], and then the space-charge parameter Q. Here knowledge of the space-charge reduction factor F is required to find Q, and a simple non-iterative method is presented for its calculation, with some results. From the other parameters already calculated the velocity parameter, b, is then found.

Since sufficient information is now available, the electronic equations are solved. These equations are in a modified form, better accounting for the effects of space-charge than the well-known standard forms. Results are compared and slight differences found to exist in the computed gain. Now that the x's and y's (respectively the real and imaginary parts of the complex propagation constants for the slow and fast space-charge waves) are known the launching loss can be calculated. Launching losses are found for the three space-charge waves, not just for the gaining wave.

The gain of the TWT is not found from the asymptotic gain equation but from a model which includes the effects of internal feedback due to reflections at the ports and attenuator. Values of reflection coefficients are modelled on the results of time-domain measurements (attenuator) and found by calculation (ports). This model permits the unstable behaviour of the tube to be predicted for various conditions of beam current and voltage and anticipates the frequencies at which instability would be likely. Results from simulations are compared with experimental observations.

The need to pulse the experimental tube under controlled conditions led to the development of a high-voltage solid-state pulse modulator providing regulated output pulses of up to 5000V and 200mA directly, without the use of transformers. The pulse modulator design embodies two unusual features a) its operation is bipolar, delivering positive or negative output pulses, depending only on the polarity of the rectifier input, and b) the use of multiple regulating loops and stacked pass elements to achieve high-voltage operation. Some results are presented.

DEDICATION

THIS work is dedicated to the LORD God Almighty, and to his Son the Lord Jesus Christ, in recognition of assistance and guidance received during the course of this project.

Zech 4 : 6 (KJV) " Not by might, nor by power, but by my spirit, saith the LORD of hosts."

PREFACE

I declare that this whole thesis is my own work, except where specifically stated to the contrary in the text, and has not been submitted in part, or in whole, to any other University.

ACKNOWLEDGMENTS

Many persons, directly or indirectly, provided in some way support, encouragement and guidance during the course of this project, and thanks are due to them all.

In particular, a special word of thanks and appreciation is due to my wife, Jenni, for many long months of support and encouragement, and for the many sacrifices she and the children, Sally and Dean, made during this period.

Also, I wish especially to thank my supervisor, Prof H L Nattrass, for valuable guidance during the course of the work, and also for his practical wisdom and skills in the laboratory in getting things to work.

I am grateful also to my fellow students Nikos Vassilopoulos and Bruce Foulis whose skills, hard work, and dedication were so vital in fabricating and testing the experimental tubes.

Thanks are also due to Clive Booth and Clyde Johnson for practical assistance in the laboratory and for the fabrication of often difficult and delicate parts for the TWT's.

I am indebted to Gunther Vath for his patience, experience, and enthusiasm in assisting with the development of the high voltage pulse modulator, and with the assembly of the automatic test facility.

My thanks are due also to the Division for Microelectronics & Communications Technology, CSIR, for funding the project without which support it could not

have proceeded, and also to ESD (Pty) Ltd for personal financial support.

C.G.Reynolds
Pretoria
May, 1994

TABLE OF CONTENTS

CHAPTER 3 - TWT DESIGN

CHAPTER 4 - AN AUTOMATED TEST FACILITY

CHAPTER 5 - SIMULATIONS AND MEASURED RESULTS

LIST OF TABLES AND FIGURES

LIST OF SYMBOLS USED

a : helix radius (metres)

A : launching loss (dB), generally referring to that of the growing wave

A_{L1} : launching loss of the gaining slow wave (dimensionless), given by the ratio V_1/V

A_{L2} : launching loss of the decaying slow wave (dimensionless), given by the ratio V_2/V

A_{L3} : launching loss of the fast wave (dimensionless), given by the ratio V_3/V

α : attenuation constant (nepers/metre), generally applicable to the cold helix loss

α_1 : attenuation constant (nepers/metre) for the input and output sections of the helix.

α_2 : attenuation constant (nepers/metre) for the attenuator section of the helix

b : TWT velocity parameter (dimensionless)

b : inner radius of TWT barrel or metal shell (metres)

Bpk : peak value magnetic field (weber/m^2) on the beam axis

B : travelling-wave tube gain parameter (nepers), defined as $B = 20(2\pi)\log_{10}(e).x_1$

B : bandwidth (Hz). Resolution bandwidth of a spectrum analyser

β : axial phase constant (radians/metre) for all electromagnetic slow waves travelling in the direction of the beam axis (z-axis).

β_o : beam phase constant, or d.c. beam propagation constant, (radians/metre), equal to ω/uo where ω is the applied radian frequency and u_o is the mean or d.c. beam velocity (metres/sec)

β_1 : axial phase constant (radians/metre) for region internal to the helix

β_2 : axial phase constant (radians/metre) for region between the helix and tube barrel

β_p : plasma phase constant (radians/metre), equal to $(eJ_o/m\epsilon_o u_o^3)$ or ω_p/u_o

β_q : plasma phase constant (radians/metre), associated with the effective plasma frequency, ωq. Equal to $\omega q/u_o$. Relates specifically to wave propagation inside the beam.

c : velocity of light in vacuo = 2.998×10^8 metres/sec

C : Pierce gain parameter (dimensionless), being defined as $C^3 = K.Io/4.Vo$

C : distributed capacitance (Farads/metre) of the helix, dielectrically loaded and enclosed in a metal shell

C_o : distributed capacitance (Farads/metre) of the helix in free space

C_s : shunt capacitance of the TEM connect for the input and output ports (Farads)

d : helix loss factor (nepers), $d = \alpha/\beta C$

d_1 : helix loss factor (nepers) for the input and output sections of the helix

d_2 : helix loss factor (nepers) in the attenuator section of the helix

d : diameter (metres) of the helix support rods

d : distance (metres) from the centre of the TEM connect conductor to the tube barrel

δ_1 : complex propagation constant (nepers/metre) for the growing slow space charge wave, $\delta_1 = x_1 + jy_1$

δ_2 : complex propagation constant (nepers/metre) for the decaying slow space charge wave, $\delta_2 = x_2 + jy_2$

δ_3 : complex propagation constant (nepers/metre) for the fast space charge wave, $\delta_3 = x_3 + jy_3$

D : dielectric loading factor (DLF)

e : charge of an electron = -1.6021×10^{-19} Coulombs

E : magnitude of the electric field (volts/metre) at the input to the helix

E_o : electric field (volts/metre) at input to helix

E_1 : initial magnitude (volts/metre) of the growing slow wave at the input to the helix

E_2 : initial magnitude (volts/metre) of the decaying slow wave at the input to the helix

E_3 : initial magnitude (volts/metre) of the fast wave at the input to the helix

E_z : combined magnitude (volts/metre) of the three waves at point z along the beam axis

ϵ_o : permittivity of free space = 8.854×10^{-12} (Farads/metre)

ϵ_r : relative dielectric constant of the helix support rods

ϵ_{r2} : mean value of dielectric constant in the region between helix and metal shell

η : electron charge-to-mass ratio, 1.759196×10^{11}coul/kg

f : frequency (Hz)

F : spacecharge reduction factor (dimensionless), also called plasma frequency reduction factor, being a function of signal frequency, helix and tube radii, and beam velocity. Magnitude always less than unity.

F : noise factor (dimensionless) of an amplifier

$F(\gamma a)$: Pierce's Impedance Function (dimensionless)

$F(\gamma r)$: Pierce's Impedance Reduction Factor. (dimensionless)

G_{ss} : small-signal (asymptotic) gain (dB)

G_{att} : small-signal gain/loss (dB) in the attenuator region

γ : radial propagation constant (rads/metre), relating to radial coordinates and dimensions in the drift space, r, a, and b.

γ_o : propagation constant of the helix,(rads/metre).

Γ_1 : propagation constant of the gaining slow wave, (rads/metre)

Γ_2 : propagation constant of the decaying slow wave, (rads/metre)

Γ_3 : propagation constant of the fast wave,(rads/metre)

I_{oa} : modified Bessel function, first kind, order zero, argument γa

I_{ob} : modified Bessel function, first kind, order zero, argument γb

I_{1a} : modified Bessel function, first kind, first order, argument γa

I_b, I_o : d.c. beam current (Amperes)

J : a.c. current density (Amps/m^2)

J_o : peak value of d.c. current density (Amps/m^2) in the electron beam

$J_o(\gamma r)$: Bessel function, first kind, order zero, argument γr

$J_1(\gamma r)$: Bessel function, first kind, first order, argument γr

k : Boltzmann's constant, 1.3805×10^{-23} joules/°K

k_o : phase constant of electromagnetic waves in free space (radians/metre). Defined as $k_o = \omega/c$

k_1 : phase constant of electromagnetic waves (radians/metre) travelling along the conducting direction of the helix, for the region inside the helix.

k_2 : phase constant of electromagnetic waves (radians/metre) travelling along the conducting direction of the helix, for the region outside the helix between the helix and barrel.

K : interaction impedance (ohms)of a sheath helix in free space

K_s : interaction impedance (ohms) of a dielectrically-loaded helix in a metal shell

K_{oa} : modified Bessel function, second kind, order zero, argument γa

K_{ob} : modified Bessel function, second kind, order zero, argument γb

K_{1a} : modified Bessel function, second kind, first order, argument γa

K_{1b} : modified Bessel function, second kind, first order, argument γb

L : length of the slow-wave structure (metres)

L_1 : length of the input section of the helix (metres)

L_2 : length of the output section of the helix (metres)

L_{as} : effective length of the attenuator section of the helix (metres)

L : distributed inductance of the helix (henries/metre), dielectrically loaded and surrounded by a metal shell

L_o : distributed inductance of the helix in free space (henries/metre)

L_T : inductance (Henries) of the tail conductor of the helix

m : mass of an electron = 9.107×10^{-31} kg

N_o : noise power (watts)

N : number of ceramic support rods

N_g : number of wavelengths contained in the cold circuit over the length of the helix

N : number of slow-wave wavelengths contained in the beam over the interaction distance

μ_o : permeability of free space = $4\pi \times 10^{-7}$ (Henries/metre)

ω : angular signal frequency (radians/sec)

ω_p : plasma frequency (radians/sec), natural frequency of oscillation of electrons in an infinitely large plasma of uniform charge density.

ω_q : effective plasma frequency (radians/sec), for a plasma with defined boundaries. Always less than ω_p by the plasma reduction factor F.

p : propagation constant (radians/metre) associated with waves propagating inside the helix in the absence of spacecharge

p : helix pitch (metres)

P : perveance of the electron gun, defined by $P = I_b/V^{3/2}$, (μpervs)

Ψ : helix pitch angle (radians, degrees)

Q : Pierce spacecharge parameter (dimensionless), being defined by the relation $4QC^3 = (\omega_q/\omega)$

Q_o : space-charge parameter (dimensionless) for a magnetically confined electron beam

r : radial parameter (metres)

r_o : electron beam radius (meters)

R : radius (metres) of the TEM connect conductor

R_a : skin effect resistance (ohms) of the helix material, usually tungsten

R_b : skin effect resistance (ohms) of the material of the inner surface of the metal shell, in this case molybdenum

Rpk : peak value of the normalised beam radius for a magnetically confined beam

ρ : a.c. charge density (coulombs/m^3) in the electron beam

ρ_o : d.c. charge density (coulombs/m^3) in the electron beam

ρ_a : surface resistivity of the helix (ohm.cm)

ρ_b : surface resistivity of the inner surface of the metal shell (ohm.cm)

ρ_s : a.c. surface charge density (coulombs/m^2)in the electron beam

ρ_1 : reflection coefficient between input section of the helix and input port

ρ_2 : reflection coefficient between input helix section and input to the attenuator

ρ_3 : reflection coefficient between output helix section and attenuator output

ρ_4 : reflection coefficient between output helix section and the output port

s : helix wire radius (metres)

u_o : mean beam velocity in the drift space (metres/sec)

T : absolute temperature (°K)

v_g : group velocity (metres/sec) in a slow-wave structure. It is the rate at which signal energy is transported in the SWS, and is defined as $v_g = d\omega/d\beta$

v_p : phase velocity (metres/sec). Defined as ω/β

V_{ps} : phase velocity (metres/sec) for slow space-charge waves

V_{pf} : phase velocity (metres/sec) for fast space-charge wave

V_o : beam voltage (volts)for which the growing slow-wave has the same velocity as the cold circuit wave

V_1 : applied beam voltage (volts)

x_1 : real part of the complex propagation constant of the growing space-charge wave, $x_1 = Re(\delta_1)$ (nepers/metre). Same for the input and output helix sections.

x_{1a} : real part of the complex propagation constant of the growing slow wave in the attenuator region, (nepers/metre)

x_2 : real part of the complex propagation constant of the decaying space-charge wave, $x_2 = Re(\delta_2)$, (nepers/metre). Same for the input and output sections of the helix.

x_{2a} : real part of the complex propagation constant of the decaying space-charge wave (nepers/metre) in the attenuator region.

x_3 : real part of the complex propagation constant of the fast space-charge wave, $x_3 = Re(\delta_3)$ (nepers/metre). Same for the input and output sections of the helix.

x_{3a} : real part of the complex propagation constant of the fast space-charge wave (nepers/metre) in the attenuator region.

X_c : capacitive coupling coefficient (dimensionless) between helix and surrounding metal shell

X_L : inductive coupling coefficient (dimensionless) between helix and surrounding metal shell

y_1 : imaginary part of the complex propagation constant of the growing space-charge wave, $y_1 = Im(\delta_1)$, (rads/metre).Same for the input and output sections of the helix.

y_{1a} : imaginary part of the complex propagation constant of the growing space-charge wave (rads/metre) in the attenuator region.

y_2 : imaginary part of the complex propagation constant of the decaying space-charge wave, $y_2 = Im(\delta_2)$, (rads/metre). Same for the input and output sections of the helix.

y_{2a} : imaginary part of the complex propagation constant of the decaying space-charge wave (rads/metre) in the attenuator region.

y_3 : imaginary part of the complex propagation constant of the fast space-charge wave, $y_3 = Im(\delta_3)$, (rads/metre).Same for the input and output sections of the helix.

y_{3a} : imaginary part of the complex propagation constant of the fast space-charge wave (rads/metre) in the attenuator region.

Z_{att} : attenuator impedance (ohms)

Z_0, Z_s : characteristic impedance (ohms) of the dielectrically-loaded helix in a metal shell

Z_H : complex helix impedance (ohms) as presented to the input or output port, modified by the attenuator impedance

Z_o : helix characteristic impedance (ohms) in free space $Z_o = (L_o/C_o)^{1/2}$

LIST OF ABBREVIATIONS

PPM	Periodic Permanent Magnet
SWS	Slow Wave Structure
TWT	Travelling-Wave Tube
DLF	Dielectric Loading Factor
CSIR	Council for Scientific and Industrial Research

CHAPTER I

INTRODUCTION

1.1.History

The domain of telephony and communication had been dominated by conventional tubes for a few decades, covering frequencies up to a few hundred megahertz. Transit-time effects and general degradation in performance parameters at higher frequencies, leading to reduced gain and lower output powers, fixed the upper frequency limit for these tubes. The demand for more space in the frequency spectrum inevitably pushed the frequency limit higher, and led to a search for a new generation of microwave devices not plagued by the limitations of conventional gridded tubes. The advent of radar during World War II also highlighted the need for devices which could provide higher signal powers at microwave frequencies.

The travelling-wave tube was invented by Kompfner[1] in 1943 and demonstrated by him the same year at Birmingham University. Early travelling-wave tubes, designed at Standard Telephones and Cables in the U.K., first saw service in 1952 in a television relay link between Manchester and Edinburgh. These pioneer tubes had power outputs of 2 watts at 4000MHz and exhibited a gain of 25dB over a 20% bandwidth. Ten years later the first TWT went into space aboard the Telstar television satellite as a broad-band power amplifier.

1.2 Some Advantages and Applications

In the past TWT's were unsurpassed in being able to offer at the same time medium output power and high gain over a wide bandwidth. In more recent times the TWT has been overtaken in performance by solid-state GaAs amplifiers, especially in terms of parameters such as very low noise, very wide bandwidth, modest power requirements, and low weight and small size. However, solid-state amplifiers, despite the great advances made in recent times, cannot rival the TWT in the area of broadband power, especially at frequencies above L-band. Furthermore, broadband solid-state linear amplifiers with output powers of a few watts are poor in efficiency, frequently as low as 5%, and this is easily surpassed by the TWT.

The main characteristics of interest in the TWT are medium to high output powers combined with relatively wide bandwidth and moderate to high gain[2][3]. Smaller helix-type TWTs with continuous output powers of a few tens of watts can be designed to operate over an octave bandwidth or greater, while the larger tubes with peak output powers of some hundreds of kilowatts may have bandwidths of only a few percent. Hybrid tubes also exist, such as the Twystron which combines the input section of a klystron with the clover-leaf or coupled-cavity output section of a TWT to generate peak powers of several megawatts,[2].

TWTs are used in the output and driver stages of coherent pulse-compression radar transmitters. The transmitted signal is not only pulse-modulated but also contains complex FM or phase-modulated information[4]. Modern surveillance radars are frequently fully coherent and require instantaneous bandwidths of at least 15%, sometimes at peak output powers between a few hundred kilowatts and a megawatt. Satellite earth stations use TWT transmitters with continuous output powers of up to

several kilowatts operating at C-band [5]. Here linearity is important in order to achieve very low levels of intermodulation, since many channels may be present. In communications satellite transponders very reliable space-qualified TWTs are used to provide sources of broadband power up to a few hundred watts at very low intermodulation levels over 500MHz of bandwidth.

In 64QAM digital radio links intermodulation levels are required to be kept extremely low and very linear TWTs [6] are used with output levels of some tens of watts. Third order intercepts frequently exceed 50dBm.

Due to the ease with which their phase may be electronically controlled, TWTs are frequently employed as output amplifiers and phase-shifters in electronically steerable phased array antennas. The US Air Force Cobra Dane phased-array radar[7] uses 96 TWTs, each with a peak power of 175kW and an average power of 10.5kW, operating over the frequency band 1175MHz-1375MHz.This radar is designed to monitor ballistic missile reentry vehicles and employs pulse widths of up to 2000μs.

1.3 Travelling-Wave Tube Design Aids

The travelling wave tube has been in existence for nearly five decades and has been referred to as "a constructed complication."[8] While it is structurally quite a simple device its behaviour is indeed complicated and difficult to model or analyse mathematically with any degree of accuracy. The theory presented in this work describes the small-signal operation of a helix TWT and is a fairly simple theory.

In view of the fact that a TWT is theoretically extremely complex, software aids are essential if any attempt is to be made to optimise various parameters for a certain

design application. Such software aids are also of great use as design aids and checks, allowing predictions to be carried out timeously on the performance of a prospective TWT before it is fabricated, thus highlighting possible weaknesses in the design.

Software packages for TWT design are usually proprietary and are often very large (up to 200,000 lines of Fortran), and are operated on fast mainframe computers. Such packages provide very effective and detailed characterisations of TWTs at a drawing-board level and are sufficiently powerful to allow many aspects of the tube development, and problems associated with such development, to be resolved prior to any prototypes being made.

Quite plainly such aids, and the development of such, is quite beyond the scope of the project, but some modest aids are possible, if not indispensable, for the project. A program has been written which can predict with reasonable accuracy, in particular, the gain of the prospective tube as a function of a number of parameters, such as frequency, beam voltage, current, and radius, helix dimensions such as pitch, radius, wire thickness, and overall length, inner radius of the TWT barrel, surface resistivity of the helix and barrel, etc. The program predicts only the small-signal performance of the tube, large-signal and non-linear effects being beyond its scope.

1.4 Overview of this Document

In Chapter II the basic small-signal gain equation is introduced and each building-block (A,B,C,and N) examined in some detail. These parameters in turn are scrutinised and other parameters identified which are essential for the analysis of these building-blocks. Firstly, the radial

propagation constant γ is discussed for the case of a sheath helix surrounded by a dielectric medium and metal shell. Then γ is found for a wire helix in the same environment in place of the sheath helix, using the method of Jain and Basu [17], offering a more accurate and realistic result at the price of greater complexity. Then the helix losses are investigated using the work of A.S.Gilmour *et al* [18],leading to a result for the helix loss parameter d, which although small is still required for the solution of the electronic and circuit equations. Next, the gain parameter C is evaluated using the well-known approach of Pierce [21], and this is followed by an investigation into the space-charge parameter Q which is a function of the plasma frequency and space-charge reduction factor F. Here, a new and more direct approach is presented in finding F which turns out to be reasonably accurate, and results are presented. Building on the work done so far in calculating parameters required for the solution of the electronic and circuit equations the velocity parameter b is then treated. At this stage all the information required for solving the electronic and circuit equations is available. The electronic and circuit equations are solved in a slightly different form which better takes into account the effects of space-charge and the parameter C. Although the effects are not dramatic compared with the standard forms of the equations it does make a modest difference to estimating the gain of the TWT, perhaps a dB or two. Two kinds of regions within the TWT are identified, namely, the low-loss input and output sections of the tube, and the high-loss attenuator region. The equations are solved separately for these two situations since the behaviour of the space-charge waves is expected to be quite different.

Once the electronic and circuit equations have been solved and the x's and y's (respectively the real and imaginary parts of the complex propagation constants for the slow

and fast space-charge waves) are known the parameters A (launching loss) and B (gaining wave parameter) may be assessed and the gain of the tube calculated. The gain calculation would be fairly straightforward were it not for the fact that a considerable amount of signal feedback can and, in this case, does exist within the tube. The effect of this feedback on the gain and stability of the tube is assessed, having calculated and estimated the reflection coefficients at the various points of reflection. Since the solution of the circuit and electronic equations also yields information on the behaviour of the other two space-charge waves, these two waves are also taken up in the feedback model, not just the gaining wave. It was felt that this would only improve the feedback model. The feedback model provides insight into the unstable behaviour of the device and allows frequency bands to be identified where such instability would be likely to occur. Varying the beam current and voltage also affects the internal feedback, determining the onset of instability.

In Chapter III a simple specification for the TWT is outlined. Historically, certain objectives had been decided upon, and these were taken up in the specification. The rest of the chapter deals with the fabrication of the TWT in its various parts without too much detail. Detailed treatments on the design and fabrication of the TWT are to be found elsewhere[9],[10].

In Chapter IV an automated measurement set-up for the TWT is described. This set-up is decribed in greater detail in [9].

In Chapter V simulated results on the behaviour and performance of the tube are presented and then compared with practical measured results. Measured results for phase velocity in a slow-wave structure are compared with

computed values as a means of testing the model developed for calculating the axial propagation constant. The internal feedback in the experimental TWT is estimated for various values of beam current and voltage and used as a criterion for determining whether the tube is likely to be unstable or not, and if so at what frequency. These findings are then compared with experimental observations. The small-signal gain of the experimental TWT is computed for a couple of different values of beam current and voltage and then compared with practical measurements.

Chapter VI presents discussion of these results and comparisons between theory and practice and certain conclusions are drawn.

The design and development of a high-voltage solid-state pulse modulator was entered into and is described in some detail in Chapter VII. Also included briefly in this chapter is the design of a grid modulator for switching the tube at the modulating electrode. The requirements for such modulators and the modes in which they should operate are described. Two unusual features of the high-voltage pulse modulator are described,(i) the operation of the modulator is bipolar, the polarity of the rectifier input determining the polarity of the output pulse, with automatic switching-over of polarity-sensitive circuits when the rectifier voltage is applied, and (ii) the use of multiple loops and stacked pass elements for voltage-sharing, enabling 5000V 200mA pulses to be generated directly without the use of transformers. The pulses are regulated in amplitude, providing good line and load regulation, and the amplitude can be adjusted continuously between 0V and 5000V. The configuration adopted is such that the modulator is capable of operating as a d.c. regulator as well, with outputs up to 5000V although at reduced current. Some of the difficulties encountered during the development are briefly described, such as

unstabilities in the multiple loops, and how they were resolved. Finally, some test results are presented showing the pulse shapes achieved at 5000V.

CHAPTER II

INTRODUCTION TO TRAVELLING-WAVE THEORY

2.1. Introduction

The interaction between an electron beam and a surrounding helix, especially for the case where the velocity of the electrons is comparable with the velocity of the wave in the helix, gives rise to certain phenomena which need to be understood and described before the behaviour and performance of a TWT can be estimated. Some of the more important processes and parameters will now be described.

a) Space-charge Waves

The periodic modulation of the charge density in the beam gives rise to so-called space-charge waves. There is always some oscillatory movement of electrons radially because of the imperfect confinement of the beam by the static magnetic field. This may be interpreted as a displacement current flowing between beam and helix. There are, however, also axial space-charge variations which constitute waves travelling at approximately the same velocity as the unperturbed electron beam and these are known as space-charge waves.

In terms of the simple theory describing these space-charge waves, there are three waves which are launched near the input to the interaction region, propagating in the same direction as the electron beam. Two of these waves, here designated E_1 and E_2, are slow waves and the third, E_3, is a fast wave. The two slow waves travel at the same velocity and are so called because of the fact that their velocity is a little lower than the unperturbed beam

velocity. The fast wave travels at a velocity a little greater than the unperturbed beam velocity.

The energy required to launch the three waves is shared more or less equally, so that the initial magnitudes are the same :

$$E_1 = E_2 = E_3 = \frac{1}{3}E_0 \quad \ldots\ldots\ldots (2.1)$$

Due to different interactions between beam and helix the magnitudes of these three waves do not remain equal. One of the slow waves, E_1, begins to increase exponentially with distance along the beam axis, while the other slow wave, E_2, decays exponentially. The fast wave travels along the beam with very slight decay in amplitude, and this is due mostly to losses in the slow wave structure.

b) Propagation of Space-charge Waves

The propagation constants, Γ_1, Γ_2, and Γ_3, respectively of the gaining slow wave, the decaying slow wave, and the fast wave may be expressed as follows [11]:

$$-\Gamma_1 = -j\beta_0 + \beta_0 C\left(\frac{\sqrt{3}}{2} - \frac{1}{2}j\right)$$

$$-\Gamma_2 = -j\beta_0 + \beta_0 C\left(-\frac{\sqrt{3}}{2} - \frac{1}{2}j\right)$$

$$-\Gamma_3 = -j\beta_0 + j\beta_0 C$$

$$\ldots\ldots\ldots (2.2)$$

where β_o is the d.c. beam phase constant, and C is the Pierce gain parameter. The propagation constants are complex for the first two waves, but for the third wave it is purely imaginary. The first wave is the gaining wave showing exponential growth with distance z along the beam, proportional to the Pierce gain parameter C and the d.c. phase constant β_o. The second wave shows decay at a rate proportional to the same parameters, while the third wave shows no change in amplitude.

c) Phase Velocities

The phase velocity of the first and second slow waves is the same and can be found by inspection of equation 2.2 above. Here it can be seen that the phase constant is slightly greater than the d.c. beam phase constant, β_o, being given as :

$$\beta = \beta_0(1 + \frac{C}{2}) \quad \ldots\ldots\ldots [2.3]$$

and from this the phase velocity is given by :

$$v_{ps} = \frac{\omega}{\beta_0(1 + \frac{C}{2})} \quad \ldots\ldots\ldots (2.4)$$

The phase velocity of the two waves is slightly lower than the beam velocity and they are known therefore as slow waves. In a similar fashion the phase constant for the third wave can be expressed as follows :

$$\beta = \beta_0(1 - C) \quad \ldots\ldots\ldots [2.5]$$

It is somewhat less than the d.c. beam phase constant, β_o, and for the third wave the phase velocity is therefore somewhat higher than the beam velocity and it is known as a fast wave :

$$v_{pf} = \frac{\omega}{\beta_0 (1 - C)} \quad \ldots\ldots\ldots (2.6)$$

d) Small-signal Gain

The signal power present at some point z on the beam is obtained by combining the contributions from the three waves, and a quantity proportional to small-signal power gain is obtained by dividing the resultant signal power at this point, proportional to $(E_z)^2$, by the square of the input magnitude E, [12]:

$$\left(\frac{E_z}{E}\right)^2 = \left(\frac{1}{9}\right).\left(1 + 4\cos(3\pi CN).\cosh(\sqrt{3}\pi CN) + \ldots \left(2\cosh(\sqrt{3}\pi CN)\right)^2\right)$$

$$\ldots\ldots\ldots (2.7)$$

where Pierce's $\beta_e z$ (the overall phase shift the wave undergoes in distance z along the beam axis) has been replaced by $2\pi N$, N being the number of wavelengths in distance z. The last term in the expression above dominates over the first two, and $\cosh(\sqrt{3}\pi CN)$ tends to $(1/2).\exp(\sqrt{3}\pi CN)$ for large values of $\sqrt{3}\pi CN$. Expressed in decibels the asymptotic gain is :

$$G_{ss}(dB) = 20\log\left(\frac{1}{3}\right) + 20.\frac{\sqrt{3}}{2}.2\pi CN.\log_{10}e$$

$$= A + BCN$$

.....(2.8)

where A is the launching loss of the gaining wave, B the gaining wave parameter, C the Pierce gain parameter, and N the total number of wavelengths over the interaction region.

From the above it would appear as though the calculation of the TWT gain would not be too difficult. In reality, though, parameters that appear as constants, like A and B, are in fact not constants at all and need to be more carefully described. Traditionally, under conditions close to ideal, values of A = -9.54dB and B = 47.3 have often been assumed, [13].

2.2 Determination of Parameters

It is evident that in order to estimate the performance of a TWT, such as the small-signal gain, certain parameters such as, for example, B, C, N, β_o, and A will need to be calculated.

2.2.1 The Radial Propagation Constant γ

The radial propagation constant γ is a very important parameter affecting the distribution of the electric fields between the helix and beam, and between the helix and barrel. It is not a simple matter to accurately estimate the propagation constant, however, and

calculation is complicated by the influences on the helix of the barrel and dielectric rods, which aggravate the problem of dispersion. These dispersive effects lead to the propagation constant becoming a rather non-linear function of frequency, which in turn causes the phase velocity also to depend non-linearly on frequency. A reasonably accurate estimate of the propagation constant is needed in helix design and for the calculation of realistic values of small-signal gain and phase when modelling tube performance.

a) Sheath Helix in a Metal Shell

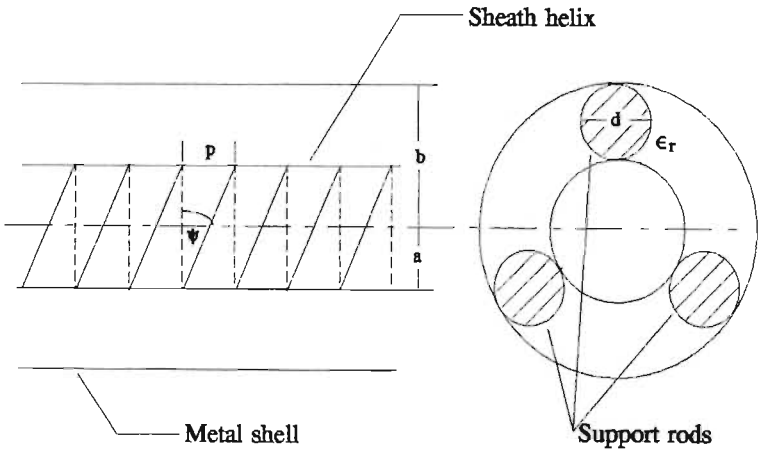

Fig 2.1 : Sheath helix in a metal shell

The case of a sheath helix surrounded by a dielectric medium in a metal shell has been widely treated in the literature. The propagation constant γ for such an enclosed helix may be found from the transcendental characteristic equation,[14], below which relates it to the propagation constant $k_1 \cot\psi$ for the same sheath helix in free space :

$$\frac{k_1^2 \cot^2 \psi}{\gamma^2} = \frac{I_{oa}^{\ 2} - I_{oa} I_{1a} \left(\frac{G_{01}}{G_{11}}\right)}{I_{1a}^2 - \varepsilon_{r2} I_{oa} I_{1a} \left(\frac{G_{10}}{G_{00}}\right)} \quad \ldots\ldots\ldots\ldots (2.9)$$

where k_1 is the phase constant for the region between helix and beam, approximately that of free space, ψ is the helix pitch angle, defined as [15] :

$$\Psi = \cot^{-1}\left[\frac{2\pi a}{p}\right] \quad \ldots\ldots\ldots\ldots [2.10]$$

where a and p are respectively the mean helix radius and pitch. The quantity ε_{r2} is the mean dielectric constant for the region between the helix and the barrel calculated from the dimensions of helix, barrel, and rods, and from the dielectric constant of the rod material. The effective dielectric constant for the region between helix and metal shell is found as follows [16] :

$$\varepsilon_{r2} = 1 + (\varepsilon_r - 1)\left(\frac{N}{4}\right)\left(\frac{d}{d + 2(a + s)}\right) \quad \ldots\ldots\ldots (2.11)$$

where d is the diameter of the ceramic support rods, ε_r is the dielectric constant of the rod material, s is the radius of the helix wire, N is the number of support rods, and a is the mean helix radius.

The G functions are combinations of modified Bessel functions defined as follows [14] :

$$G_{oo} = I_{oa}K_{ob} - K_{oa}I_{ob}$$

$$G_{11} = I_{1a}K_{1b} - K_{1a}I_{1b}$$

$$G_{o1} = I_{oa}K_{1b} + K_{oa}I_{1b} \qquad \text{.....(2.12)}$$

$$G_{1o} = I_{1a}K_{ob} + K_{1a}I_{ob}$$

The characteristic equation as stated above in (2.9) cannot be solved for γ in closed form . It is done numerically using the Newton-Raphson iteration method which is simple and converges rapidly.

The axial propagation constant β is found directly from γ from the following relation :

$$\beta^2 = \gamma^2 + k_1^2$$

From β the phase velocity of the circuit can be found :

$$v_p = \omega/\beta$$

This is in the absence of the beam, and is hence known as the "cold" circuit or unperturbed phase velocity.

b) Wire Helix in a Dielectrically-loaded Metal Shell

Treating a wire helix as a sheath helix of the same mean radius leads to errors in the computation of the radial propagation constant, generally leading to values which are too high. A wire helix, unlike the sheath helix, has a free-space region between turns which diminishes the effect of the dielectric loading between helix and metal shell, and this leads to somewhat higher phase velocities. The wire helix case has been treated in the literature [16,17] and a procedure developed by which the

dielectrically-loaded region between helix and metal shell is divided into a large number of very thin dielectric tubes of differing dielectric constant, the effective dielectric constant for each tube being found from smoothing out the dielectric of the support rods around the tube. The dielectric loading factor (DLF) is then computed by combining successively the contributions of the dielectric tubes, starting from the outermost adjacent to the metal shell and working inwards up to the outer radius of the helix. After the dielectric loading factor is calculated the characteristic equation can be solved numerically for γ. While the procedure is a lot more tedious than in the case for the sheath helix and requires more computer time, the extra effort is rewarded by improved accuracy in determining the phase velocity and assessing dispersive effects.

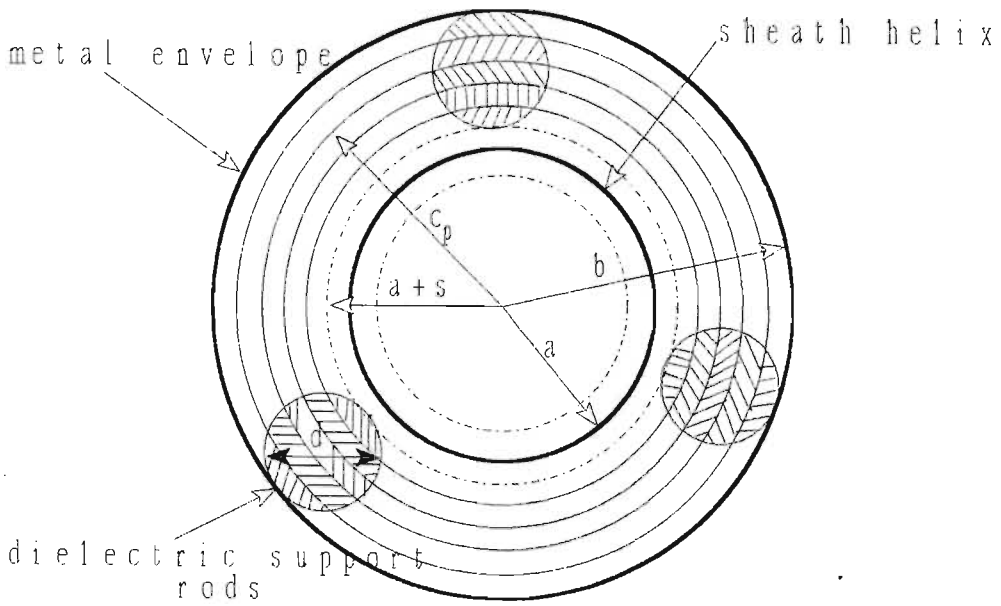

Fig 2.2 : Cross-section of the SWS with helix supported by circular dielectric rods

A cross-section of the helical slow-wave structure with free-space gap is shown in Fig 2.2. Although the space between helix and metal envelope is shown as being divided into only six tubes in the diagram, in effect there are n = 100 to ensure convergence, in agreement with the suggestion in [17]. The diameter of the dielectric rods is d, the dielectric constant of the rod material is ϵ_r, the mean radius of the wire helix is a, and the wire radius is s.

The dispersion relation used in [17] is as follows :

$$\left(\frac{k_1 \cot\psi}{\gamma}\right)^2 = \left(\frac{I_{0a}K_{0a}}{I_{1a}K_{1a}}\right)D^2 \quad \ldots\ldots(2.13)$$

where k_1, ψ, and γ have the usual meanings, as in equation (2.9), and where D is the dielectric loading factor. The dielectric loading factor D for Approach II (circular rods) in [17] is used and is given by :

$$D = \left[\frac{I_{0a}P_0 + K_{0a}Q_0}{K_{0a}Q_0\left(1 - \frac{I_{1a}K_{1b}}{K_{1a}I_{1b}}\right)}\right]^{1/2} \quad \ldots\ldots\ldots(2.14)$$

It will be noted that in the above expression for D, the denominator differs slightly from that used by Jain and Basu in [17] because a different notation has been adopted. In [17] c is used to denote the radius of the metal shell and b_i the radius of the interface between the ith and $i+1$th dielectric tubes, and $b_n = c$. In this work b denotes the radius of the metal shell (which is a more standard practice) and c_i the radius of the interface between the ith and $i+1$th dielectric tubes, and $c_n = b$.

As in [17], i is counted from near the outer radius of the helix (i = 1) to where i = n-1, just short of the metal shell. Because it is the interface between the wire helix and the dielectric region that is of interest in finding the radial propagation constant γ, the process of calculating the dielectric loading factor D commences at i = n-1 and i is progressively decremented to i = 1 near the outer radius $a + s$ of the helix.

The equations for the quantities P and Q which are needed for the computation of D are as follows :

i) for $i = n-1$

$$P_{n-1} = \left[\varepsilon'_{r,n}\left(1 + \frac{I_{1c_{n-1}}K_{0b}}{K_{1c_{n-1}}I_{0b}}\right) - \varepsilon'_{r,n-1}\left(1 - \frac{I_{0c_{n-1}}K_{0b}}{K_{0c_n}I_{0b}}\right)\right]K_{0c_{n-1}}K_{1c_{n-1}} \qquad \ldots\ldots\ldots (2.15a)$$

$$Q_{n-1} = -\left[\varepsilon'_{r,n}I_{0c_{n-1}}K_{1c_{n-1}}\left(1 + \frac{I_{1c_{n-1}}K_{0b}}{K_{1c_{n-1}}I_{0b}}\right) + \varepsilon'_{r,n-1}I_{1c_{n-1}}K_{0c_{n-1}}\left(1 - \frac{I_{0c_{n-1}}K_{0b}}{K_{1c_{n-1}}I_{0b}}\right)\right] \qquad \ldots\ldots\ldots (2.15b)$$

ii) for $1 \le i \le (n-2)$

$$P_i = \left(\varepsilon'_{r,i}I_{0c_i}K_{1c_i} + \varepsilon'_{r,i+1}I_{1c_i}K_{0c_i}\right)P_{i+1} + \left(\varepsilon'_{r,i} - \varepsilon'_{r,i+1}\right)K_{0c_i} \qquad \ldots\ldots\ldots (2.15c$$

$$Q_i = \left(\varepsilon'_{r,i} - \varepsilon'_{r,i+1}\right) I_{0c_i} I_{1c_i} P_{i+1} + \left(\varepsilon'_{r,i} I_{1c_i} K_{0c_i} + \varepsilon'_{r,i+1} I_{0c_i} K_{1c_i}\right) Q_{i+1} \quad \ldots\ldots\ldots (2.15d)$$

from which the following may be obtained before insertion into equation (2.14):

$$P_0 = \left(I_{0c_0} K_{1b_0} + \varepsilon'_{r,1} I_{1c_0} K_{0c_0}\right) P_1 + \left(1 - \varepsilon'_{r,1}\right) K_{0c_0} K_{1c_0} Q_1 \quad \ldots\ldots\ldots (2.15e)$$

$$Q_0 = \left(1 - \varepsilon'_{r,1}\right) I_{0c_0} I_{1c_0} P_1 + \left(I_{1c_0} K_{0c_0} + \varepsilon'_{r,1} I_{0c_0} K_{1c_0}\right) Q_1 \quad \ldots\ldots\ldots (2.15f)$$

For the computation of the P's and Q's above, the effective relative dielectric constant pertaining to each dielectric tube needs to be calculated. The effective dielectric constant for a particular dielectric tube is obtained by smearing the dielectric material uniformly over the cross-section of the dielectric tube. The assumption is made in [17] that the effective dielectric constant is a function of a)the ratio of the area of dielectric material in the dielectric tube to the overall area of the dielectric tube, and b) of the dielectric constant of the rod material. Values of effective

dielectric constant are calculated for i = 1 to i = n-1. For the ith dielectric tube :

$$\varepsilon'_{r,i} = 1 + (\varepsilon_r - 1)\frac{A_{s,i}}{A_i}$$

$$= 1 + (\varepsilon_r - 1)\frac{N\left[\left(a+s+\frac{id}{n}\right)^2\left(\theta_i - \frac{sin2\theta_i}{2}\right) \div \left(\frac{d}{2}\right)^2\left(\varphi_i - \frac{sin2\varphi_i}{2}\right) - A_{s,i-1}\right]}{\pi\left[\left(a+s+\frac{id}{n}\right)^2 - \left(a+s+\frac{(i-1)d}{n}\right)^2\right]}$$

.....(2.15g)

Here $A_{s,i}$ refers to that portion of the cross-sectional area of the ith tube which is occupied by dielectric material, while A_i is the overall cross-sectional area of the ith tube. N is the number of dielectric support rods, in this case 3. Finally, the angles θ_i and ϕ_i are given as follows:

$$\theta_i = \cos^{-1}\left[\frac{\left(a + s + \frac{d}{2}\right)^2 + \left(a + s + \frac{id}{n}\right)^2 - \left(\frac{d}{2}\right)^2}{(2(a + s) + d)\left(a + s + \frac{id}{2}\right)}\right]$$

.....(2.15h)

$$\varphi_i = \cos^{-1}\left[\frac{\left(a + s + \frac{d}{2}\right)^2 + \left(\frac{d}{2}\right)^2 - \left(a + s + \frac{id}{n}\right)^2}{d\left(a + s + \frac{d}{2}\right)}\right]$$

.....(2.15i)

The method of Jain and Basu [17] employs N dielectric tubes in the space between helix and tube barrel. These dielectric tubes are of equal thickness. Investigations carried out varying the number N showed that satisfactory convergence of γ to a final value only occurred for N>100. In practice, N was increased to 200 when most of the simulations were run, although execution time became considerably longer. Examining Fig 2.2 it can be seen that in the middle of the space between helix and tube barrel the width of the dielectric segments contributed by the support rods to the dielectric tubes reaches a maximum, and the mean value of the dielectric constant would also be at a maximum, varying very little from dielectric tube to adjacent dielectric tube.

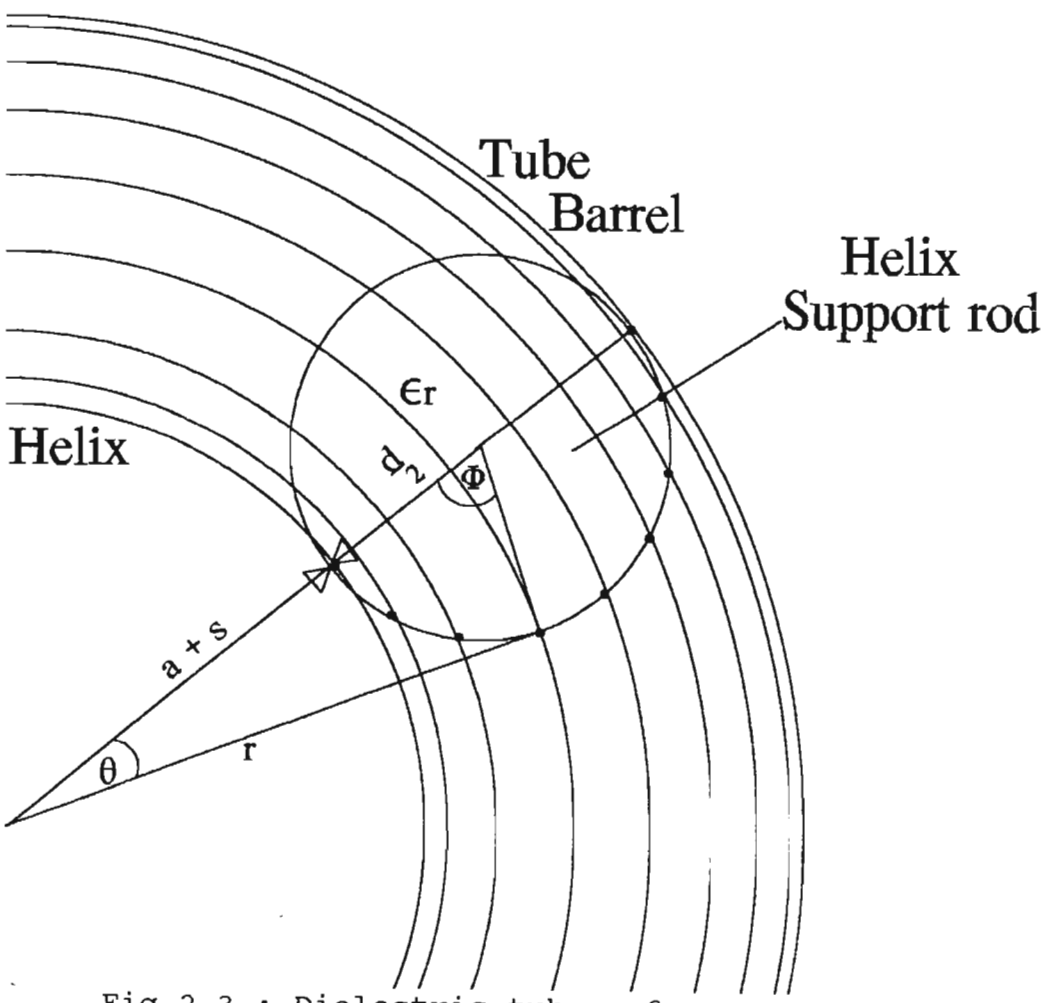

Fig 2.3 : Dielectric tubes of varying thickness

However, near the helix the width of the dielectric segments contributed by the rods falls rapidly towards zero, suggesting that the mean dielectric constant might be more sensitive to radial position near the helix. These considerations led to the decision to use a non-uniform distribution of dielectric tube thicknesses, the thinnest tubes being close to the helix and to the inner surface of the tube barrel, while the thickest would be those in the centre of the space between helix and barrel. The scheme is illustrated in Fig 2.3 where the angles θ and Φ are the same as in [17]. The angle Φ varies from zero at the helix ($r = a + s$) to π at the inner surface of the tube barrel ($r = a + s + d$), and the angular range between 0 and π is divided up into N equal values. Although only eight tubes are shown in the drawing the variation in tube thickness is fairly obvious. Using i as a sequence number as before ranging between 0 and N :

$$\phi_i = \frac{i\pi}{N} \qquad \ldots\ldots\ldots\ldots\ldots\ldots (2.16)$$

and from this

$$\theta_i = \tan^{-1}\left(\frac{\frac{d}{2}\sin\phi_i}{a+s+\frac{d}{2}-\frac{d}{2}\cos\phi_i}\right) \qquad \ldots\ldots\ldots\ldots (2.17)$$

The radial ordinate out to the ith dielectric tube is

$$r_i = \sqrt{(a+s+\frac{d}{2}-\frac{d}{2}\cos\phi_i)^2+(\frac{d}{2}\sin\phi_i)^2} \qquad \ldots\ldots\ldots (2.18)$$

From this point onwards the equations (2.15) are used to compute the relative dielectric constants for the dielectric tubes, and then the P's and Q's are calculated as before, before finally inserting P_o and Q_o into equation (2.14) to find γ.

It was found that for satisfactory convergence N = 200 was still necessary, and that execution was slightly slower than for the first method. However, it may be seen from Fig 2.4 that simulated results for this modified method for v/c using Belohoubek's slow-wave structure measurements differ somewhat from those obtained using the

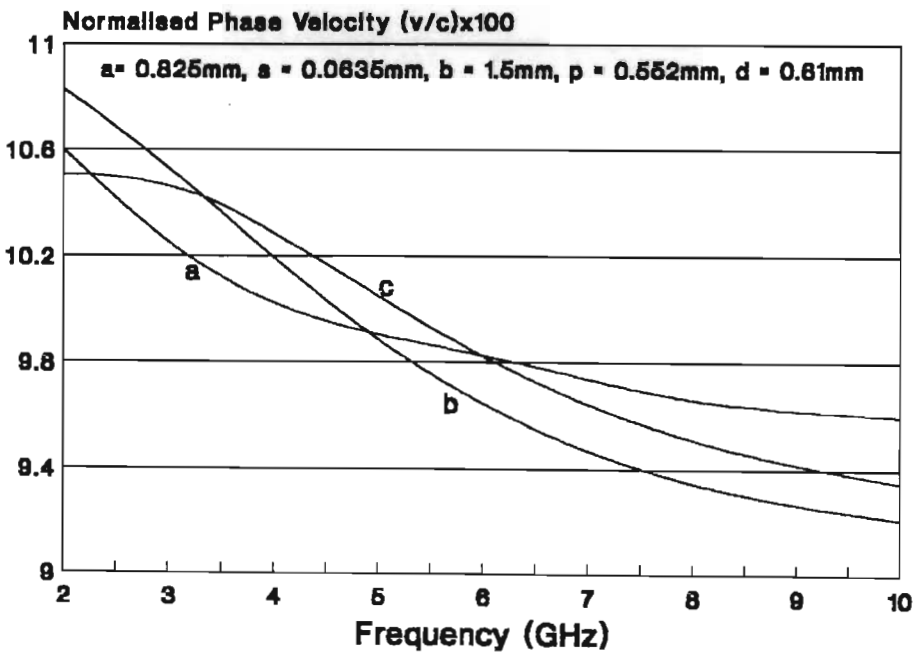

Fig 2.4 : Normalised phase velocity (v/c) Belohoubek's measured data, (a), simulation using the method of [17],(b), and modified method,(c)

method of [17]. At low and high frequencies the modified method compares somewhat better with Belohoubek's measured data than with that of the method of [17], but at other

frequencies the method of [17] looks better. These differences would suggest that results are sensitive to exactly how the method is implemented, and probably also to the number of dielectric tubes, N, into which the space around the helix is divided.

Shown in Fig.2.5 plotted against frequency are the computed propagation constants for a sheath helix, and for a wire helix as used in one of the earlier experimental tube designs, and the difference is quite evident. Later, the design of the helix was revised, reducing the radius and pitch but still optimising the propagation constant for a 4500V beam. A plot of the predicted propagation constant for the redesigned wire helix is shown in Fig 2.6, showing similar characteristics.

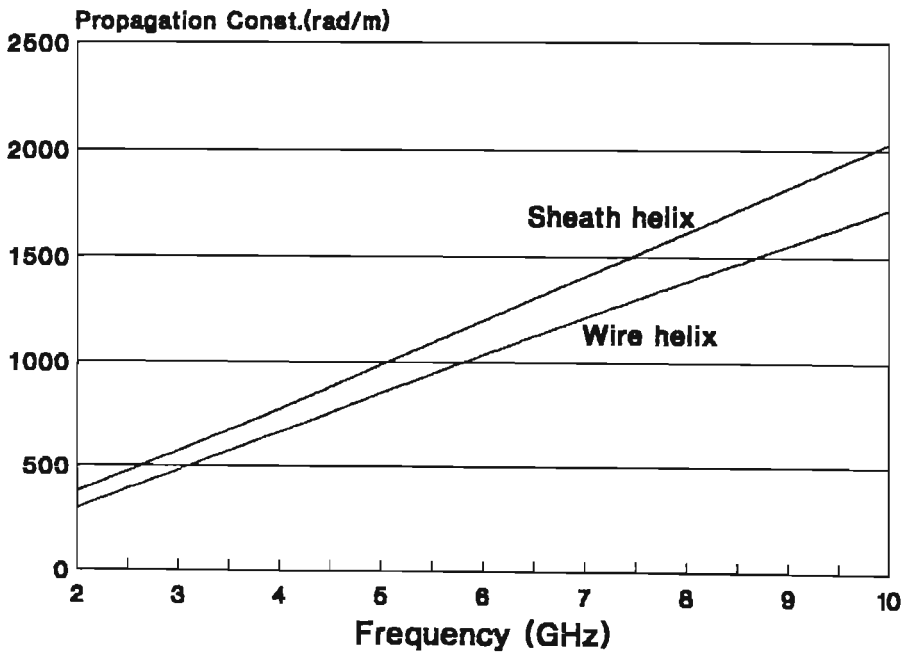

Fig 2.5 : Axial propagation constant for an early experimental tube with a = 1.75mm,p = 1.41mm

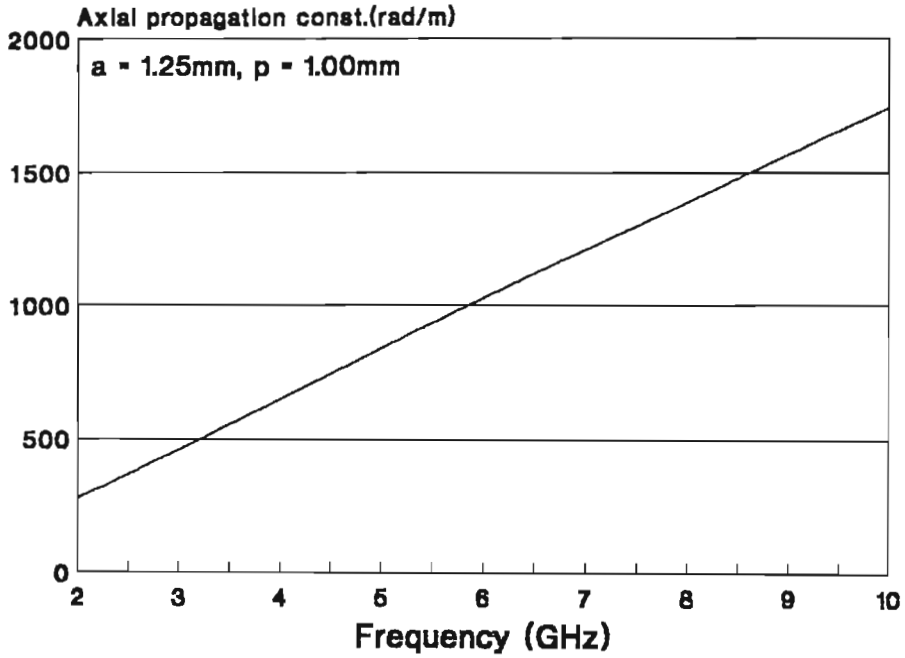

Fig 2.6 : Axial propagation constant for a wire helix with a = 1.25mm, p = 1.00mm

2.2.2 Calculation of Helix Losses

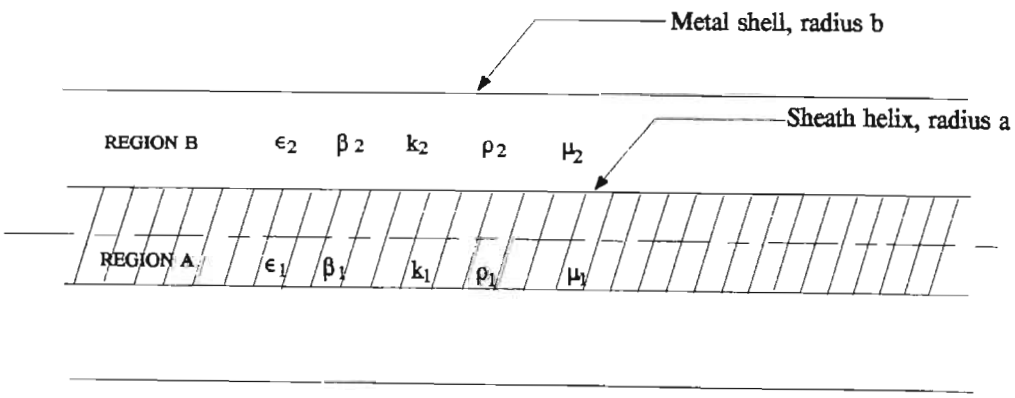

Fig 2.7 : Sheath helix enclosed in a metal shell

Losses in the slow-wave structure are significant in determining the gain of the tube and also the efficiency. The program calculates the axial attenuation constant α, using the equations derived by A.S.Gilmour *et al* in their paper [18]. In this paper two regions are defined as may be seen in Fig 2.7, the first region (Region A) pertaining to the helix and the space within it, where the parameters $\epsilon_1, \beta_1, k_1, \rho_1$, and μ_1 are defined, and the second region, Region B, to the space between helix and barrel, where $\epsilon_2, \beta_2, k_2, \rho_2$, and μ_2 are defined. The losses are calculated separately for the two regions and then combined. These losses arise due to the finite surface resistivity of the helix surface, and also of the inner surface of the barrel. The dielectric losses are not considered. The simulated losses for a particular TWT are compared with measured values, and the measured losses are found to be quite a bit higher than those predicted. Gilmour *et al* put this down to the effects of surface roughness, not accounted for in their theory, which could cause higher resistivity and hence higher losses, while Jain and Basu disagree on this point [19]. Gilmour's equation is somewhat complicated but can be solved directly without resorting to iterative methods [18]:

$$\alpha = \frac{-2k_2 R_a I_{oa}^2}{120\pi a \beta_1 L_T} (\varepsilon_{r2})^{\frac{3}{2}} \left[\frac{b.R_b}{a.R_a} \left\{ \left(\frac{1}{\gamma b G_{00}} \right)^2 + \left(\frac{\gamma}{k_2^2 b G_{11} \cot\psi} \right)^2 \right\} + \ldots \right.$$

$$\left. \ldots + \left(\frac{I_{1a}}{\varepsilon_{r2} I_{0a}} \right)^2 + \left(\frac{\gamma^2 I_{0a}}{k_1^2 \cot\psi \varepsilon_{r2} I_{1a}} \right)^2 + \left(\frac{\gamma^2 G_{01}}{k_2^2 \cot\psi G_{11}} \right)^2 + \left(\frac{G_{10}}{G_{00}} \right)^2 \right]$$

.....(2.19)

where β_1 is the axial phase constant between helix and beam, given by the relation $\beta_1^2 = \gamma^2 + k_1^2$, and R_a and R_b are respectively the skin-effect resistances of the surface of

the helix and the inner surface of the tube barrel, defined as follows :

$$R_a = \sqrt{\pi \mu_0 f \rho_a} \qquad R_b = \sqrt{\pi \mu_0 f \rho_b}$$

where f is the frequency (Hz), μ_o is the permeability of free space, and ρ_a and ρ_b are respectively the surface resistivities of the helix surface and the inner surface of the tube barrel. The function LT is a dimensionless function given below :

$$LT = M(\gamma a)\left[1 + \left(\frac{\gamma I_{0a}}{k_1 \cot\psi I_{1a}}\right)^2\right] + \epsilon_{r2}\frac{\beta_2}{\beta_1} I_{0a}^2 \cdot \left\{\left(\frac{b^2}{a^2}M(\gamma b) - M(\gamma a)\right)\left[\frac{K_{0b}^2}{G_{00}^2} + \left(\frac{\gamma}{k_2 \cot\psi}\right)^2 \frac{K_{1b}^2}{G_{11}^2}\right] + \left(\frac{b^2}{a^2}N(\gamma b) - N(\gamma a)\right)\left[\frac{I_{0b}^2}{G_{00}^2} + \left(\frac{\gamma}{k_2 \cot\psi}\right)^2 \frac{I_{1b}^2}{G_{11}^2}\right] + 2\left(\frac{b^2}{a^2}P(\gamma b) - P(\gamma a)\right)\left[K_{0b}\frac{I_{0b}}{G_{00}^2} - \left(\frac{\gamma}{k_2 \cot\psi}\right)^2 K_{1b}\frac{I_{1b}}{G_{11}^2}\right]\right\} \qquad \ldots(2.20)$$

where β_2 is the axial phase constant for the region between helix and barrel, defined by the relation $\beta_2^2 = \gamma^2 + k_2^2$, and the functions M(x), N(x), and P(x) are defined as follows :

$$M(x) = I_1^2(x) - I_o(x).I_2(x)$$
$$N(x) = K_1^2(x) - K_o(x).K_2(x)$$
$$P(x) = I_1(x).K_1(x) + I_o(x).K_2(x)$$

Shown in Fig 2.8 is a plot of the helix attenuation constant for a = 1.25mm, b = 3mm, and $\rho a = 5.6 \times 10^{-6}$ohm-cm for the tube barrel (molybdenum) and helix (tungsten).

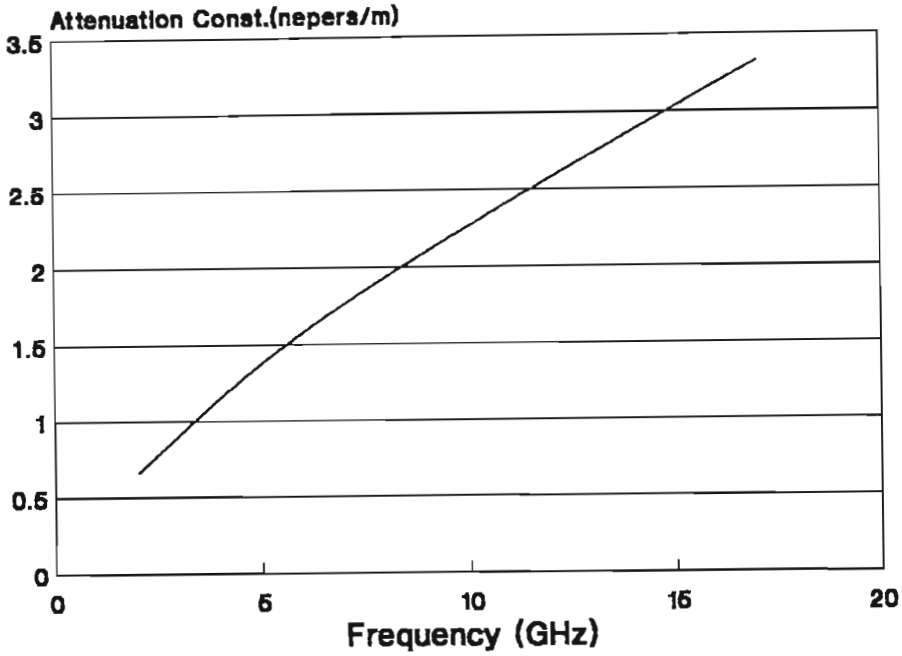

Fig 2.8 : Helix attenuation constant α (nepers/m) for a = 1.25mm

The helix loss factor, d, is defined by the relation [20]

$$\alpha = \beta C d \quad \text{.....(2.21)}$$

where C is the Pierce gain parameter, and ß is the axial propagation constant associated with the helix. For low-loss helices the loss factor d is very small. For the attenuator region where α is usually large, d is correspondingly also much larger leading to a lower gain in this region.

2.2.3 Gain Parameter C and Interaction Impedance

For a sheath helix the Pierce gain parameter C is derived from [21] :

$$C = \left(\frac{\beta_1 I_b}{8 V_1 k_0}\right)^{1/3} . \left(\frac{\gamma}{\beta_1}\right)^{4/3} . F(\gamma a) . F(\gamma r) \quad \ldots\ldots\ldots\ldots\ldots\ldots (2.22)$$

where β_1 and γ are respectively the axial and radial propagation constants, k_0 is the free space propagation constant, and I_b and V_1 are respectively the beam current and voltage. The functions F(γa)(Pierce's Impedance Function) and F(γr)(Impedance Reduction Factor) are defined as follows [22,26] :

$$F(\gamma a) = \left[\frac{\gamma a I_{0a}}{240 K_{0a}}\left[\frac{I_{1a}}{I_{0a}} - \frac{I_{0a}}{I_{1a}} + \frac{K_{0a}}{K_{1a}} - \frac{K_{1a}}{K_{0a}} + \frac{4}{\gamma a}\right]\right]^{-\frac{1}{3}} \quad \ldots\ldots (2.23)$$

$$F(\gamma r) = \left(I_0(\gamma r)^2 - I_1(\gamma r)^2\right)^{1/3} \quad \ldots\ldots\ldots\ldots\ldots\ldots (2.24)$$

The impedance function F(γa) determines the fall-off with increasing frequency of the interaction between helix and beam, due to the fact that the fields are more closely confined to the turns of the helix and the relative field strength on the axis of the beam is reduced as a consequence. The impedance reduction factor F(γr) performs an averaging of the field strength within the cross-section of the beam ; quite plainly it is not uniform and is much higher at the edges of the beam. An average figure for the interaction is required since the gain parameter C is in any case an "average" quantity at any point along the length of the interaction region.

Shown in Fig 2.9 are computed plots of C for the original helix design, a = 1.75mm, p = 1.41mm and for V = 4500V, I = 80mA, and for the revised helix design, a = 1.25mm, p = 1.00mm. A beam radius of 0.7mm was assumed. The improvement in coupling between beam and helix is evident

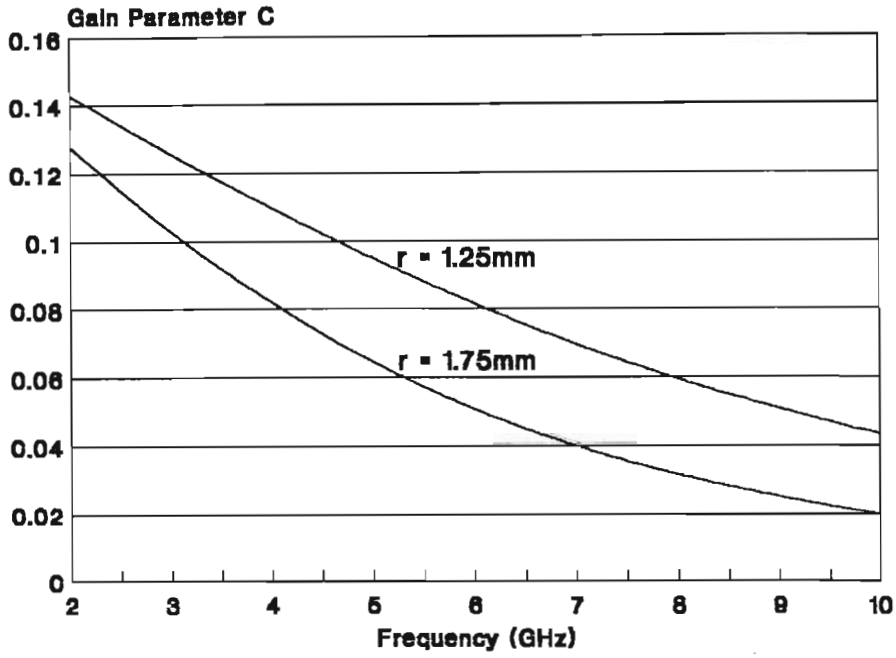

Fig 2.9 : Gain parameter C for two helix designs with a 4500V 80mA beam

for the smaller helix radius, this also leading to higher gain for a given helix length, since the decibel gain of the tube is more or less proportional to C.

The interaction impedance K is chiefly a property of the slow-wave structure in the absence of space charge and is related [22] to the gain parameter C by the following relation:

$$C^3 = \frac{KI_b}{4V_1} \quad \ldots\ldots\ldots\ldots (2.25)$$

For a sheath helix in free space K may be expressed as follows:

$$K = \left(\frac{\beta_1}{2k_0}\right)^{1/3} \cdot \left(\frac{\gamma}{\beta_1}\right)^{4/3} \cdot F(\gamma a) \cdot F(\gamma r) \quad \ldots\ldots\ldots\ldots\ldots\ldots (2.26)$$

For practical wire and tape helices this sheath model gives values of impedance which are too high. Tien [23] shows that reduction factors need to be applied to the above sheath model to account for the effect of dielectric loading on the helix, and for difference between tape and sheath. Singh *et al* [24] have suggested that the fall in interaction impedance due to dielectric loading can be empirically related to ratio of the characteristic impedance with dielectric loading to the characteristic impedance in free space :

$$K_s = K\left(\frac{Z_s}{Z_0}\right)^{\frac{4}{3}} \quad \ldots\ldots\ldots\ldots [2.27]$$

where K_s and Z_s are respectively the interaction and characteristic impedance for the dielectrically loaded structure, and K and Z_o are the same parameters for the helix in free space. Jain and Basu [25] have also suggested that the loss in the helix may somewhat reduce the interaction impedance :

$$K_s = K\left(\frac{\beta_1^2 - \alpha\beta_1 \exp\left(-\frac{\pi\alpha}{2\beta_1}\right)}{\alpha^2 + \beta_1^2}\right) \quad \ldots\ldots\ldots\ldots\ldots\ldots (2.28)$$

where $\alpha + j\beta_1$ is the axial propagation constant for the helix with loss. In low-loss helices the above effect is

negligible, but would play a role in lossy helix sections serving as attenuators.

Shown in Fig 2.10 is a plot of the interaction impedance of the LP10 tube.

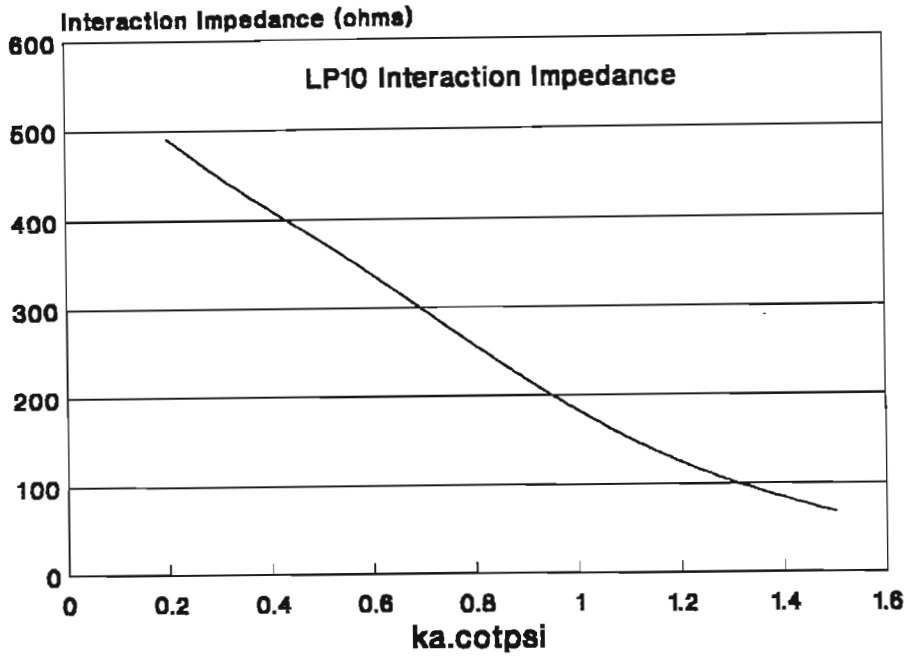

Fig 2.10 : Interaction impedance of the LP10 tube

2.2.4 Space-charge Parameter QC

The parameter QC plays a significant role in the behaviour of space-charge waves and as a consequence affects the gain and phase of the tube. Determination of the factor QC, rather than Q, is indicated since it appears in this form in the electronic and circuit equations. It is defined by the relation :

$$QC = \frac{F^2 . \omega_p^2}{4C^2\omega^2} \quad \ldots\ldots\ldots\ldots\ldots\ldots (2.29)$$

derived from eqn (10-67) in [27]. Here F is the plasma frequency reduction factor (always less than unity) by which $\omega_q = F.\omega_p$. The plasma frequency is given by [28]:

$$\omega_p = \left(\frac{e.I_b}{\pi m \epsilon_0 u_0 r^2}\right)^{1/2} \quad \ldots\ldots\ldots\ldots\ldots\ldots (2.30)$$

where I_b is the beam current, and r is the beam radius. Since the beam current is dependent on the cathode-anode voltage V_1 in terms of the gun perveance P, and the beam velocity u_o is a function of the same voltage, we can express the plasma frequency as a function of the applied beam voltage :

$$\omega_p^2 = 1.0662012x10^{16}.\frac{PV_1}{r^2} \quad \ldots\ldots\ldots (2.31)$$

where $I_b = PV_1^{3/2}$ and $u_o = (2eV_1/m)^{1/2}$, and the constants have been replaced by a single numerical value. Expressing the plasma frequency in this way is useful where the cathode voltage may be used as a variable control on the other tube parameters. For the electron gun being considered, P = .265μPerv, therefore

$$\omega_p = 53155.635.\frac{V_1^{1/2}}{r} \quad \ldots\ldots\ldots\ldots (2.32)$$

The plasma frequency reduction factor F must now be defined before QC can be computed. This factor is found from the relation :

$$F^2 = \frac{p^2}{p^2 + \gamma^2} \quad \ldots\ldots\ldots\ldots\ldots\ldots (2.33)$$

derived from eqns (9.44) to (9-49)in [29]. Here p is the radial propagation constant pertaining to the region without space-charge between the helix and beam, and γ is the radial propagation constant within the helix in the presence of space-charge. The value for γ has by this time already been computed by the program, but p is related to γ by the transcendental equation [29] :

$$\gamma r . \frac{J_1(\gamma r)}{J_0(\gamma r)} = - pr . \left(\frac{I_1(pr) . K_0(pa) + K_1(pr) . I_0(pa)}{I_0(pr) . K_0(pa) - K_0(pr) . I_0(pa)} \right) \quad \ldots\ldots\ldots\ldots (2.34)$$

Normally, this equation would be solved numerically but a direct method has been contrived [Appendix B] whereby

$$F^2 = \left[\frac{p^2 r^2 T}{p^2 r^2 T - 48\left(\frac{T}{4} - \frac{1}{pr}\right) - 48\sqrt{\left(\frac{T}{4} - \frac{1}{pr}\right)^2 + \frac{T^2}{12}}} \right] \quad \ldots\ldots (2.35)$$

and where

$$T = \frac{I_1(pr) . K_0(pa) + K_1(pr) . I_0(pa)}{I_0(pr) . K_0(pa) - K_0(pr) . I_0(pa)} \quad \ldots\ldots\ldots\ldots (2.36)$$

In the program an approximation is made in which β_o replaces p in the above calculation. This is permissible since they are very similar. Shown in Fig 2.11 are plots of the space-charge reduction factor using equations (2.35)and (2.36).

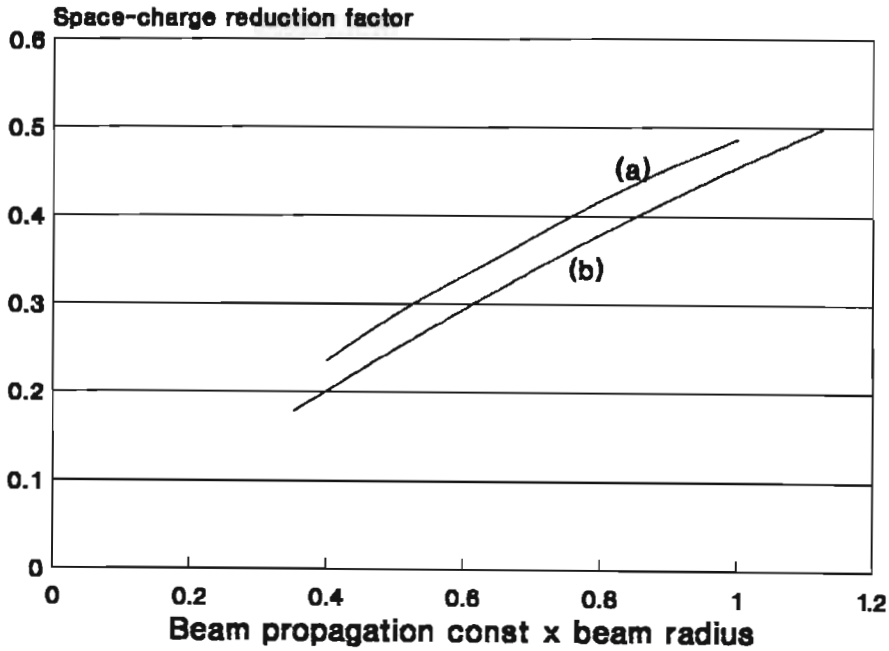

Fig.2.11 : Space charge reduction factor for r/a = .75, (a), Branch Mihran, (b), this simulation

Here for r/a = .75 the results of Branch and Mihran [30] are compared with those obtained by the use of equations (2.35) and (2.36), where the results of this simulation are seen to be consistently about 10% lower.

All the calculations have now been performed which are necessary for the computation of QC.

2.2.5 The Velocity Parameter b

The velocity parameter, b, relates the phase velocity, v_p, of the circuit to the velocity of the beam, u_o and is a

measure of the difference between these velocities. Parameter b is related to these velocities as follows :

$$u_0 = v_p(1 + Cb) \quad \ldots\ldots\ldots\ldots (2.37)$$

The velocity of the slow spacecharge, v_s, is related to the beam velocity, u_o, by the effective plasma frequency, ω_q, so that

$$v_s = \left(1 - \frac{\omega_q}{\omega}\right)u_0 \quad \ldots\ldots\ldots\ldots (2.38)$$

A useful criterion has been proposed [31] if maximum small-signal gain is required whereby the beam velocity could be adjusted such that the slow spacecharge wave has the same velocity v_s as the phase velocity v_p of the "cold" circuit wave. Here b would need to be somewhat positive:

$$b = \frac{\omega_q}{\omega C} \quad \ldots\ldots\ldots\ldots\ldots\ldots (2.39)$$

We may also define a beam voltage V_o as that voltage which would be required to make the beam velocity the same as the cold circuit phase velocity, that is,

$$V_0 = \frac{m}{2e}\cdot\left(\frac{\omega}{\beta_1}\right)^2 \quad \ldots\ldots\ldots\ldots (2.40)$$

and, derived from this,

$$b = \left(\frac{V_1^{1/2}}{V_0^{1/2}} - 1\right).\frac{1}{C} \quad \ldots\ldots\ldots\ldots (2.41)$$

where V_1 is the applied beam voltage. If $V_1 > V_o$ the electrons in the beam go faster than the circuit wave and the parameter b assumes a positive value, while for $V_1 < V_o$ b is then negative.

2.2.6 Solution of the Electronic Equations

The electronic and circuit equations comprise two cubic equations which must be solved simultaneously. The coefficients of these equations are comprised of parameters and factors which by now have been calculated in the program, that is d, b, C, and QC, so that we are now in a position to proceed to the solutions.

The equations used in the program are similar to the well-known forms [32], but those terms containing C and QC^2 have been retained, whereas in the standard forms they have been discarded on the grounds that they are negligible. It was felt that this is frequently not the case and that errors could be aggravated. The equations have been derived in Appendix C and are repeated here :

$$Cy^4 - 2y^3 - (2b + 6Cx^2 - Cd^2 + Cb^2 + 2QC^2)y^2 + (6x^2 + 4dx + 4Cbdx + 4C + 8QC - 16QC^2b)y + (Cx^4 + 2bx^2 - Cd^2x^2 + Cb^2x^2 - 2 - 2Cb - 4QC^2d^2 + 4QC^2b^2 + 8QCb + 20QC^2x^2 + 16QC^2dx) = 0$$

$$\ldots\ldots\ldots\ldots\ldots\ldots\ldots\ldots\ldots\ldots (2.42a)$$

$$(1 - 2Cy)x^3 + (d + Cbd)x^2 - (3y^2 + 2by - 4QC - Cd^2y + Cb^2y - 2Cy^3 - 2C + 8QC^2b - 5Cy)x = 0 \quad \ldots\ldots\ldots\ldots\ldots\ldots (2.42b)$$

where C is Pierce's gain parameter, Q is the space charge parameter, b is the velocity parameter, and d is the helix loss factor. In the program these equations are solved simultaneously using the Newton-Raphson iterative method which is quite fast and converges rapidly. It requires the calculation of the derivative of the function in estimating the next iterate.

The equations are solved twice, once for the low-loss input and output sections of the helix using the helix loss parameter d_1, and a second time for the high-loss attenuator section using the much larger loss parameter d_2.

There are six outputs for each of these solutions, a pair of values (an x and a y) for each of the slow-waves, and a pair for the fast wave. Fig.8.1 of [33]and Figs 10.4 to 10.7 of [34] provide some insight into the behaviour of the waves under various conditions of space charge, loss, and parameter b. The first pair, x_1 and y_1, relate to the gaining slow wave, the second pair, x_2 and y_2, to the decaying slow wave, and x_3 and y_3 to the fast wave. The x values are the real components and relate to the magnitudes of the respective space-charge waves, and the y values are imaginary, determining the phases. In particular, x_1 is significant because it represents the magnitude of the gaining wave and hence determines the gain of the tube. For a tube with some gain x_1 is always positive, necessary for exponential growth of the signal. Its value lies between zero (zero gain) and a maximum value of .866, attained only under conditions where the

space charge QC, the helix loss d, and velocity parameter b are all effectively zero. In practice, its value may peak typically to between 0.5 and 0.6.

For the fast wave the magnitude of x_3 is in reality slightly negative because of the non-zero helix loss, leading to some decay in its magnitude over the length of the interaction region. The value for y_3 is always positive, necessary for a fast wave, and is typically close to unity for conditions of negligible space charge, low loss, and b close to zero.

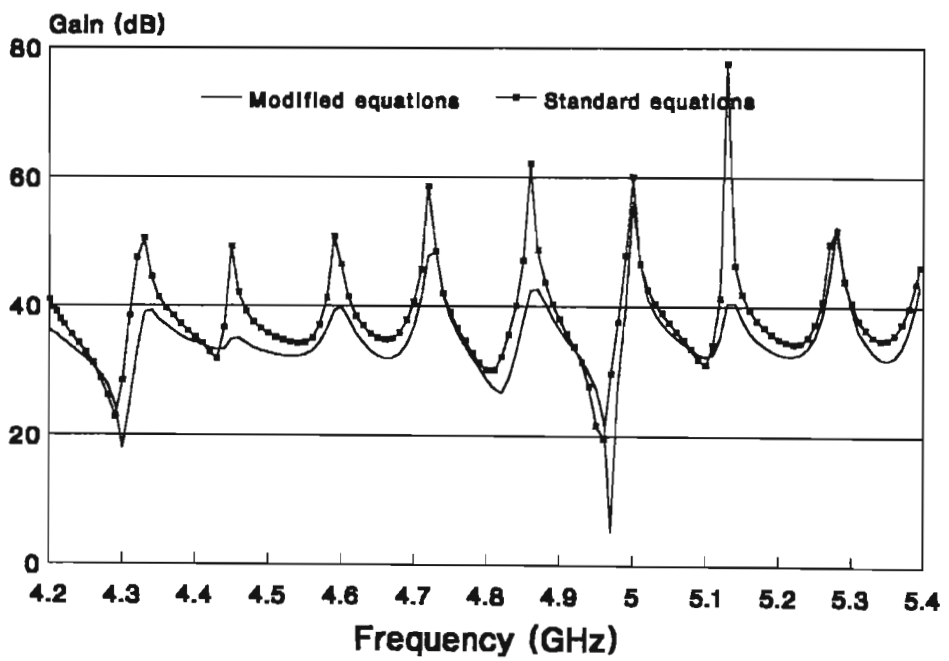

Fig 2.12 : Simulated gain at 4500V 45mA using the standard and modified equations

In Fig 2.12 the simulated gain of the experimental TWT (LP10) is plotted having used both the standard equations and the modified equations. While the difference in the result is not dramatic it is to some extent accentuated by the considerable feedback present in the tube. Generally, the standard equations appear to give slightly more

optimistic values of gain and somewhat more phase shift, leading to larger amounts of feedback and hence larger swings in the gain over frequency.

2.2.7 The Launching Loss

Knowledge of the launching loss is needed in estimating the gain of the TWT, since it forms part of the gain equation. In simple calculations a value of 20log(1/3) = -9.54dB is often assumed and this is reasonably correct under conditions where the velocity parameter b is zero, that is, where the slow space-charge waves are synchronous with the unperturbed circuit wave. Under other conditions, however, the launching loss will depart considerably from the value of 9.54dB, so it was considered necessary in the program to calculate with reasonable accuracy the actual values for the launching loss. To do this the electronic equations need first to be solved, and the values obtained for the x's and y's then inserted into the equation obtained for launching loss. Based on equation (D17) derived in Appendix D we have for the decibel launching loss for the gaining slow-wave :

$$A_{L1}(dB) = 20\log\left(1 + \frac{[\delta_2^2](\delta_1 - \delta_3)(1 + jC\delta_1)}{[\delta_1^2](\delta_3 - \delta_2)(1 + jC\delta_2)} + \ldots + \frac{[\delta_3^2](\delta_2 - \delta_1)(1 + jC\delta_1)}{[\delta_1^2](\delta_3 - \delta_2)(1 + jC\delta_3)}\right) \ldots\ldots (2.43)$$

where the $\delta_n = x_n + jy_n$. The δ_n are always complex quantities and the above equation is first manipulated in the program to obtain the magnitudes before the decibel loss is calculated.

In view of the fact that all three space-charge waves are considered in estimating the gain of the tube in the presence of internal feedback, launching losses are defined for all three waves. Therefore, based on equations (D19) and (D21) we have for the decibel launching loss for the other two space-charge waves:

$$A_{L2}(dB) = 20\log\left(1 + \frac{[\delta_1^2](\delta_2 - \delta_3)(1 + jC\delta_2)}{[\delta_2^2](\delta_3 - \delta_1)(1 + jC\delta_1)} + \ldots + \frac{[\delta_3^2](\delta_1 - \delta_2)(1 + jC\delta_2)}{[\delta_2^2](\delta_3 - \delta_1)(1 + jC\delta_3)}\right) \quad \ldots\ldots (2.44)$$

$$A_{L3}(dB) = 20\log\left(1 + \frac{[\delta_1^2](\delta_2 - \delta_3)(1 + jC\delta_3)}{[\delta_3^2](\delta_1 - \delta_2)(1 + jC\delta_1)} + \ldots + \frac{[\delta_2^2](\delta_3 - \delta_1)(1 + jC\delta_3)}{[\delta_3^2](\delta_1 - \delta_2)(1 + jC\delta_2)}\right) \quad \ldots\ldots (2.45)$$

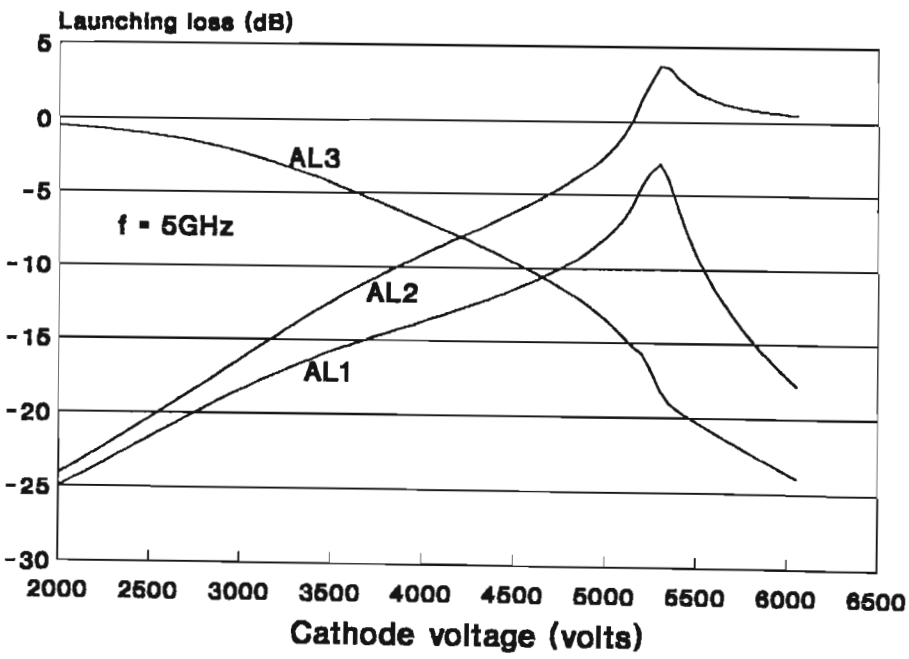

Fig 2.13 : Launching losses for the three space-charge waves at 5GHz

Shown in Fig 2.13 are the launching losses for the three space-charge waves at 5GHz, indicating how they would vary with changes in the beam conditions.

2.2.8 Parameters B and N

The calculation of the gaining-wave parameter B is very straight-forward once the electronic and circuit equations have been solved, since [35]

$$B = 20(2\pi)\log_{10}e.x1 = 54.57x_1 \quad \ldots\ldots\ldots\ldots (2.46)$$

Values of B are always real and positive under conditions where the tube exhibits gain.

The total phase shift in the circuit when not perturbed by the beam is ßL where L is the length of the slow-wave structure, and the number of wavelengths is

$$N_g = \frac{\beta L}{2\pi} \quad \ldots\ldots\ldots\ldots\ldots\ldots (2.47)$$

The number of wavelengths N contained in the beam will depend on the beam velocity, since the slow-waves are compelled always to travel slower than the electrons, and therefore [47]

$$N = \frac{N_g}{(1 + Cb)} \quad \ldots\ldots\ldots\ldots\ldots\ldots (2.48)$$

The polarity and magnitude of velocity parameter b is controlled by the applied beam voltage, and the number of

stream wavelengths N can vary considerably above and below N_g.

2.2.9 Helix Impedance and Port Characteristics

Knowledge of the helix characteristic impedance is important for matching the helix to the 50 ohm input and output ports. The impedance of the helix is the free space characteristic impedance of the helix modified by the presence of the ceramic helix support rods and the metal tube barrel. The helix impedance is not easy to measure, but may be quite accurately estimated from the theory. Following the approach of B.N.Basu [36] the inductance and capacitance per unit length of the helix in free space are first obtained, and these are then modified by the dielectric rods and metal shell. For the helix in free space :

$$L_0 = \frac{\mu_0}{2\pi} I_{1a} K_{1a} \left(\frac{\beta}{\gamma}\right)^2 \cot\psi^2 \quad (Henries/metre) \qquad \ldots\ldots\ldots\ldots\ldots\ldots (2.49a)$$

and

$$C_0 = \frac{2\pi\epsilon_0}{I_{0a} K_{0a}} \quad (Farads/metre) \qquad \ldots\ldots\ldots\ldots\ldots\ldots (2.49b)$$

For the helix in the metal shell, supported by the dielectric rods, the values of L_o and C_o are modified as shown in equation 2.50 below. The quantities X_L , and X_c, are respectively the inductive and capacitive coupling coefficients between helix and metal shell, and ϵ_r is the

effective dielectric constant for the region between the metal shell and helix. Often a mechanism is employed [16] whereby the dielectric property of the support rods is "smeared" out to fill the whole region between helix and metal shell with a continuous dielectric medium of lower dielectric constant.

$$L = L_0(1 - \chi_L)$$

$$C = \frac{C_0}{(1 - \chi_C)}\left[1 + (\epsilon_r - 1)\gamma a I_{0a} K_{1a}\left(1 + \frac{I_{1a}K_{0b}}{K_{1a}I_{0b}}\right)\right]$$

$$\text{where } \chi_L = \frac{I_{1a}K_{1b}}{K_{1a}I_{1b}} \quad , \quad \chi_C = \frac{I_{0a}K_{0b}}{K_{0a}I_{0b}}$$

.....(2.50)

The characteristic impedance of the helix in the metal shell, supported by dielectric rods is therefore

$$Z_0 = \left(\frac{L}{C}\right)^{\frac{1}{2}} \quad .....(2.51)$$

The helix impedance is a function of frequency, falling from a large value at low frequencies to a much lower value at higher frequencies, as may be seen for the LP10 helix shown in Fig 2.14 below.

The helix is terminated near its centre by the attenuator, whose impedance does not have the same dependence on frequency as that of the helix. This imperfect matching of the helix to the attenuator usually situated somewhere near its centre translates to frequency-dependent complex

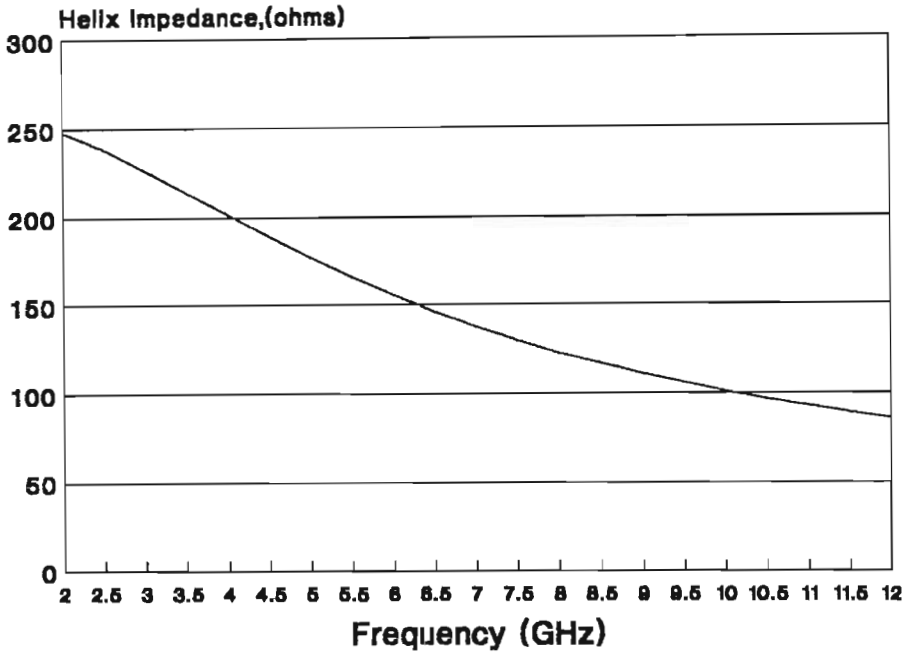

Fig 2.14 : Helix impedance for a = 1.25mm, p = 1mm

impedances at the two ends. These impedances are calculated by assigning to the attenuator a value of impedance (in practice this is difficult to measure or estimate), and then treating the helix as two sections of low-loss transmission line of known length, L_1, impedance, Z_o, and propagation characteristics, $\alpha+j\beta_1$, which transform the attenuator impedance, Z_{att}, to some complex value :

$$Z_H = Z_0\left[\frac{Z_{att}\cos\beta_1 L_1 + jZ_0\sin\beta_1 L_1}{Z_0\cos\beta_1 L_1 + jZ_{att}\sin\beta_1 L_1}\right] \quad \ldots\ldots (2.52)$$

The helix terminates in the TEM connect, which may be modelled as a small series inductance, due to the "tail" of the helix between the last turn and the output/input port, followed by a shunt susceptance due to the

capacitance of the TEM connect to the tube barrel. The inductance of the helix tail has been estimated as follows

$$L_{TL} = \frac{\mu_0}{8} \; Henries/metre \; \ldots\ldots\ldots (2.53)$$

Estimation of this inductance is not easy because of the complicated geometry of the input and output ports, but it is basically a shielded system, the tail wire of the helix being screened by the tube barrel and other components. The expression above was adapted from that for the inductance of a coaxially screened conductor,[37]. In practice, values of about 450 picohenries were used for the overall inductance L_T (see Fig 2.15).

The shunt capacitance of the TEM connect was estimated from theory based on electrostatic principles, this being justified by the fact that the physical dimensions of the connect are generally much less than the shortest wavelength of interest. Measurements of this capacitance were considered too unreliable and inaccurate to be used in any analysis. The capacitance of a round conductor in a dielectric medium to a ground plane on either side was estimated as follows :

$$C = \frac{4\varepsilon_0\varepsilon_r}{\ln\left[\frac{d}{R}+\sqrt{\frac{d^2}{R^2}-1}\right]}\left(\pi-\tan^{-1}\left(\frac{R}{d-\sqrt{d^2-R^2}}\right)\right) \; Farads/metre \; \ldots\ldots\ldots (2.54)$$

The expression above was adapted from that for the capacitance of two round conductors,[38]. Here d is the

spacing from the centre of the TEM connect conductor to the ground plane on either side (tube barrel), and R is the radius of the TEM connect conductor. For d = 2mm and R = .75mm the above expression yields a value of 343pF/metre, and the value of the shunt capacitance C_s was estimated as .34pF. Vassilopoulos (9) performed a finite element analysis on the TEM connect, carefully taking the geometry of the port into account, and found a value of .45pF for the structure. Although the value of .34pF was used for most of the simulations, this was later replaced by .45pF since this latter value was felt to be more reliable.

The loss in the helix, although low, does affect the value of the impedance presented to the termination and therefore the return loss. The attenuation constant for the helix, α_1, is calculated and the loss is therefore $\alpha_1 L_1$ nepers. The effect of this small loss (typically 0.5 to 1dB, but depends on the frequency) on the impedance is approximated by including at the output of the port a 50 ohm attenuator with the same value of loss, where,[39]:

$$R_{sh} = \frac{50}{\sinh(\alpha_1 L_1)}$$

$$R_s = \frac{50}{\tanh(\alpha_1 L_1)} - R_{sh} \qquad \text{.....(2.55)}$$

The equivalent circuit of the input section of the helix and those elements which affect it is shown in Fig 2.15. The impedance of the helix is modified by these elements, especially at higher frequencies by the susceptance, so

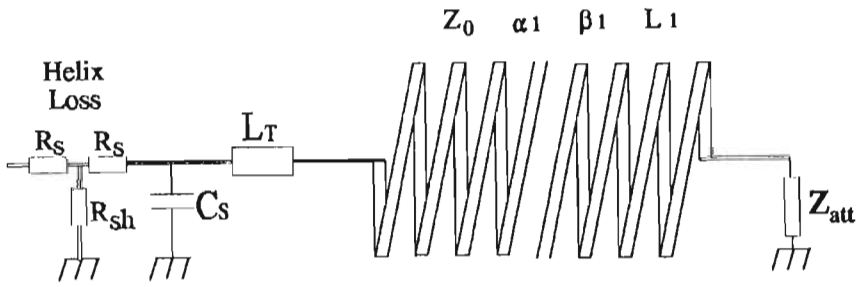

Fig 2.15 : Equivalent circuit of helix input section and input port

that the impedance seen at the port contains a fairly dominant capacitive component. This capacitive component results in a poor return loss if the port is terminated directly in 50 ohms without the use of a suitable RF impedance matching network.

Shown in Fig 2.16 is the measured (cold)input return loss, S11, for the experimental TWT LP10, performed by Vassilopoulos (9) on an HP8510 network analyser, and also some simulated results using the analysis of this section. There is a reasonably good correspondence on average between the measured and simulated results, but there is some difference in the periodicity with frequency of the two patterns. This is most likely due to the imperfect isolation achieved by the attenuator between the two helix sections and their respective ports. The simulation did not take this into account. In general, however, both simulated and measured data point to the poor matching at the ports due to the absence of proper matching transformers and inadequate attenuator performance.

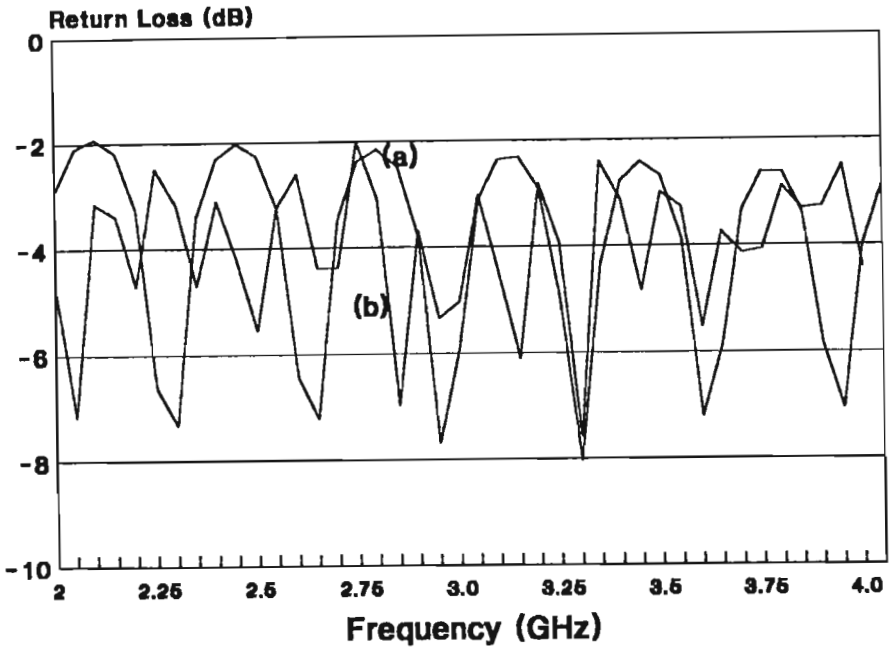

Fig 2.16 : Simulated return loss,(a), and measured S11 data,(b)

2.2.10 Reflections in the TWT

Due to the inevitably imperfect impedance matching encountered in an experimental TWT, reflections of signals will take place within the device. Reflections are undesirable since they may lead to instability or to variations in gain with frequency. Four principal regions of reflection were identified, namely, at the input and output ports and at the attenuator input and output. Irregularities in the helix pitch, with consequent fluctuations in the helix impedance, were considered to be of minor importance and then only from turn to turn, so that over the full length of the helix the pitch is kept quite uniform on average. Minor reflections internal to the helix are therefore considered to cancel out. The effect of the four significant sources of reflection was examined and modelled into the gain simulations. Regions

of possible instability over the frequency band can also be predicted.

Values of reflection coefficient at the input and output ports were estimated from the theory, from theoretical

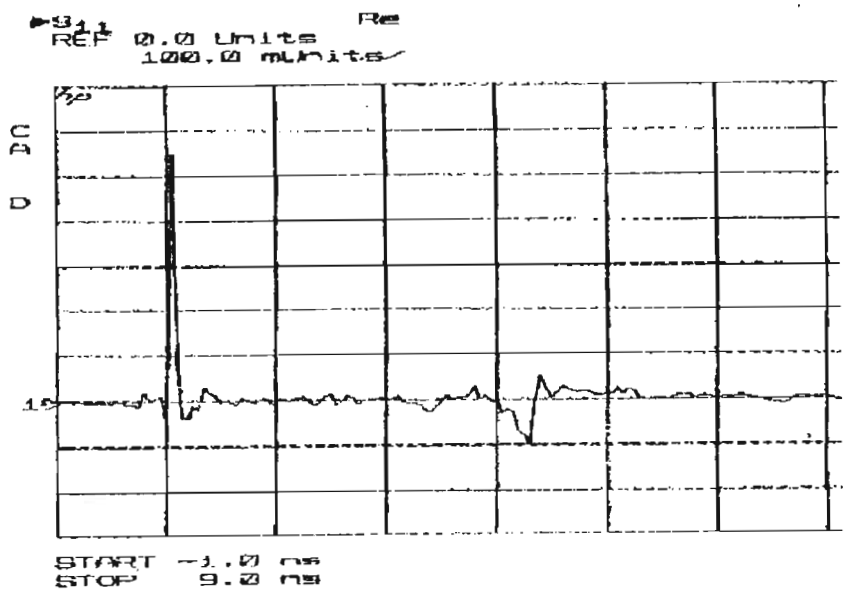

Fig 2.17 : Time domain response of the input port and attenuator input

estimates of the helix characteristic impedance as modified by its environment and by stray external inductance and port susceptance, all functions of frequency.

Values of reflection coefficient at the attenuator input and output were determined by analysis of time domain network analyzer plots of the properties of the "cold" helix subassembly, conducted over a wide frequency band. These time domain measurements were performed on an HP8510B network analyser by Vassilopoulos [9]. The results for the input and output sections of the slow-wave structure (S11 and S22) are shown in Figs 2.17 and 2.18. The measurements are performed in the frequency domain

over a predetermined frequency band and then converted to time domain data. The large reflections to the left in Figs 2.17 and 2.18 represent reflected energy at the ports while the smaller reflections to the right are due to the mismatch between attenuator and helix. The reflections are proportional to the voltage reflection coefficients. Because the data is assembled from measurements made over a wide band in the frequency domain, the reflections represent an overall effect due to signals at many frequencies. These measurements may therefore be of doubtful value in characterising the ports and attenuator, but are useful in determining the sites of reflections due to mismatch.

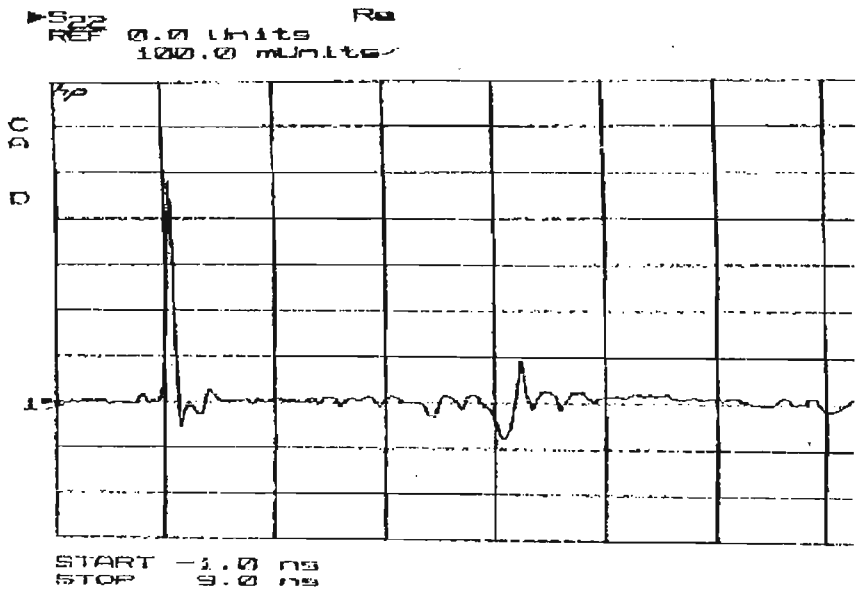

Fig 2.18 : Time domain response of the output port and attenuator output

The attenuator is of finite length (approximately one third of the overall helix length) and is fabricated by depositing a very thin layer of molybdenum on the dielectric rods. The conductivity of the molybdenum layer is tapered to an approximately cosinusoidal profile by

controlling its thickness, being a maximum at the centre of the attenuator.

The effect of these reflections on the small signal gain of the tube is examined in detail in Appendix D.

2.2.11 Attenuator Characteristics

An adequate attenuator loss across a wide frequency band is essential if stability in tube behaviour is to be maintained, since it chiefly affects signals reflected back to the input. A purely theoretical model of cold attenuator loss did not appear feasible, so a model was adopted which was based on measured cold loss data. The cold loss data was derived from S21 plots performed by Vassilopoulos [9] on an HP8510 network analyser on the LP8 slow-wave structure over the band 2 to 14GHz. Using the cold loss data a third order polynomial was generated which approximates average values of the measured S21 data with reasonable accuracy. The polynomial does not track the periodic variations in the S21 data, which in any case would be due to mismatch between the helix and the ports during the measurement and is not therefore characteristic of the attenuator. The polynomial is given below:

$$P(f) = 2.161278E\text{-}02.f^3 - 0.4831512.f^2 + 2.662876.f + 26.7387 \quad \ldots\ldots\ldots\ldots\ldots\ldots (2.56)$$

Here the frequency f is in GHz and $P(f)$ in decibels. In Fig.2.19 the measured S21 data is plotted, giving approximately the attenuator cold loss, and with it the third order polynomial, showing fairly good correspondence between them over a wide frequency band. In the solution

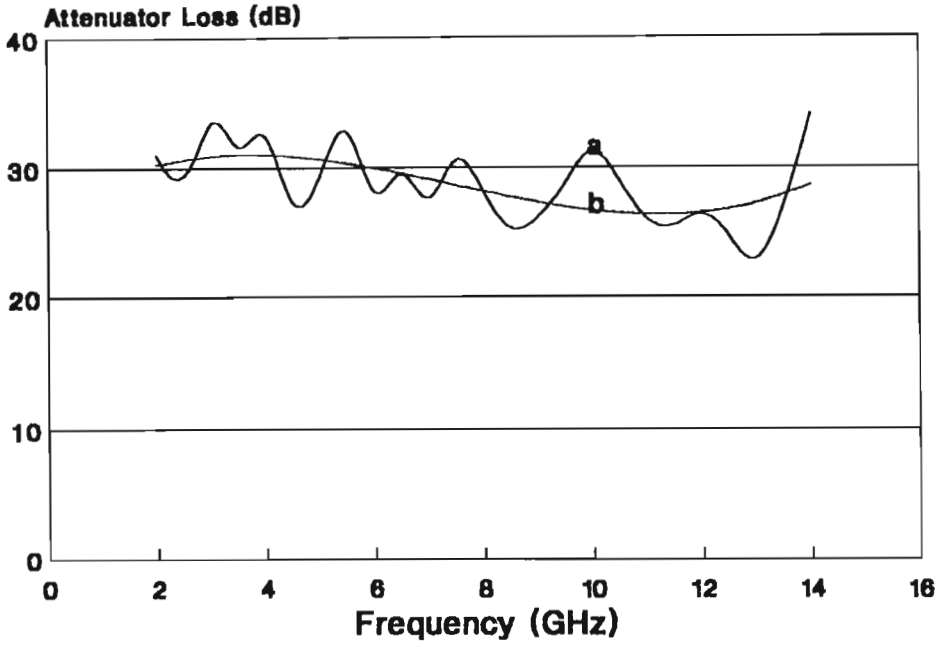

Fig 2.19 : Measured S21 data,(a), and third order polynomial,(b)

of the electronic equations a loss factor, d_2, is used to determine the behaviour of the three space-charge waves as they propagate through the attenuator region in the forward direction. The parameter d_2 can be estimated as follows :

$$d_2 = \frac{P(f)}{8.686\beta_0 CL_{as}} \qquad \text{.....(2.57)}$$

In the reverse direction, from the output back towards the input, the loss in amplitude of the reflected waves is dominated by the attenuator loss where:

$$\alpha_2 = \frac{P(f)}{8.686 L_{as}}$$

.....(2.58)

For waves travelling in the forward direction towards the output the behaviour of the attenuator is very different from that in the reverse direction. In the forward direction total signal energy is shared between that propagating in the slow-wave structure and that carried by the beam, whereas in the reverse direction it is carried almost entirely by the circuit. Although the circuit fields will decay rapidly in the attenuator, the signals in the beam are much less affected because of the relatively weak interaction between the beam and the lossy helix section. The attenuator was modelled as a drift space, i.e, a beam without a surrounding slow-wave structure, using the equations of Gittins [49]. However, since weak fields still exist, coupling the beam to the lossy helix, this drift space is treated as "lossy" and the electronic equations need to be solved again in the presence of a much higher loss factor, d_2. Because the signal energy is carried predominantly by the beam the transport of the signal through the attenuator region is best described by the ratio of a.c. current, i_2, in the beam exiting the attenuator to a.c. current, i_1, entering the attenuator. Therefore [49]:

$$\frac{i_2}{i_1} = \frac{(\delta_2\delta_3 - \delta_1\delta_2 - \delta_1\delta_3 + 4QC)\cos[\beta_0 CL_{as}\sqrt{4QC}]}{(\delta_2 - \delta_1)(\delta_3 - \delta_1)} + \frac{\left((\delta_1 + \delta_2 + \delta_3)\sqrt{4QC} + \frac{\delta_1\delta_2\delta_3}{\sqrt{4QC}}\right)\sin[\beta_0 CL_{as}\sqrt{4QC}]}{(\delta_2 - \delta_1)(\delta_3 - \delta_1)}$$

.....[2.59]

where the δ_n are the propagation constants $x_n + jy_n$ for the lossy region in the forward direction, β_o is the d.c. beam constant, and L_{as} the length of the attenuator section. The attenuator exhibits either a slight gain or loss, depending mostly on the frequency. The decibel gain or loss can quite simply be expressed as :

$$G_{att} = 20\log_{10}\left|\frac{i_2}{i_1}\right| \quad \text{.....[2.60]}$$

Shown in Fig 2.20 is the transport characteristic of the attenuator for the LP10 tube. At lower frequencies the

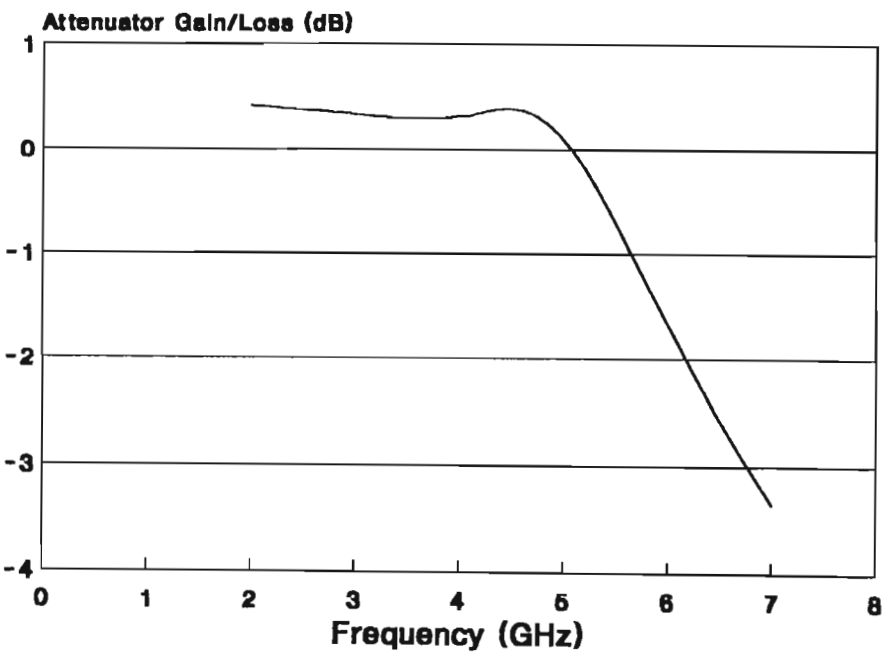

Fig 2.20 : Attenuator gain/loss for LP10 at 4500V 80mA

attenuator shows a modest gain, but above 5GHz becomes increasingly lossy. This plainly would influence the high frequency performance of the tube.

2.2.12 Electron Beam Profile

In the electron beam, the current density is not uniform but falls from some peak value on the beam axis to zero at the beam edge. Measurements were carried out [10] using a beam analyser to determine the beam profile, and a plot of these measurements is shown in Fig 2.21. Superimposed on

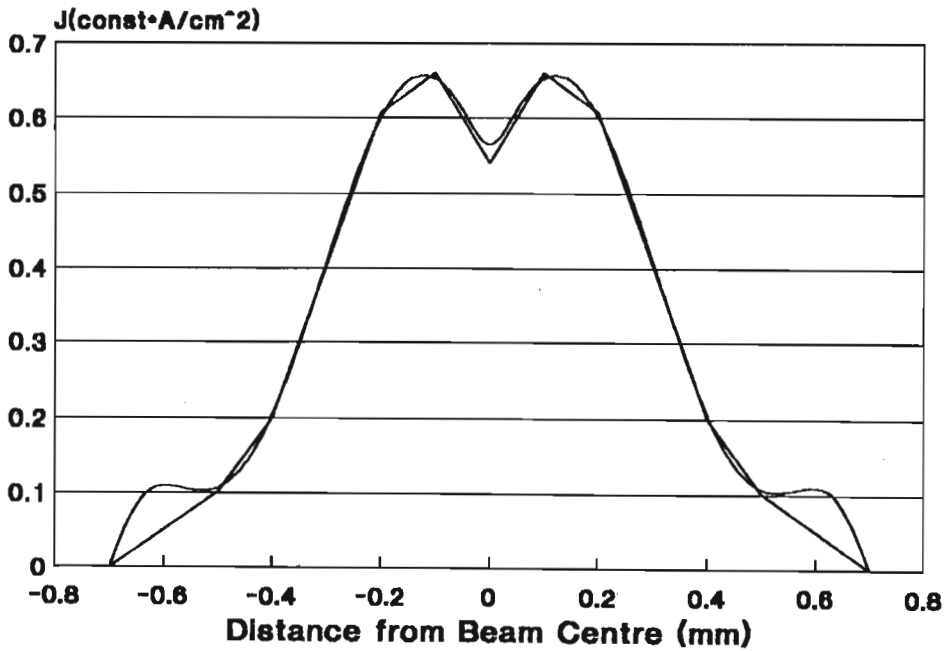

Fig 2.21 : Measured and simulated electron beam profile

the measured data is a fifth-order polynomial which turns out to be quite a good approximation to the current density profile, except at the outer edge of the beam where there is noticeable error. This polynomial is given by :

$$J(r) = -9.508097E{+}16.r^5 + 1.38598E{+}14.r^4 - 5.46572E{+}10.r^3$$

$$-5.284348E{+}5.r^2 + 1.670326E{+}03.r + 0.54$$

.....(2.61)

where r is the radial position in the beam in metres. Normalising the beam radius by adjusting the coefficients of the polynomial so that the peak value is unity provides the following :

$$P(r/r_0) = -24.04036.(r/r_0)^5 + 50.06149.(r/r_0)^4$$

$$- 28.20247.(r/r_0)^3 - .3901048.(r/r_0)^2$$

$$+ 1.759072.(r/r_0) + 0.812392$$

.....(2.62)

Of interest is the relationship between the peak current density J_o and the average current density which can be simply related to the beam current which is known. Therefore (see Appendix A):

$$J(r/r_0) = 0.9717718.\frac{I_b}{r_0^2}.P(r/r_0)$$

.....(2.63)

From this current density function the plasma frequency can be estimated as a function of beam radius r_o and position r. The plasma frequency in turn plays a role in determining the space-charge parameter Q and the behaviour of the space-charge waves.

2.2.13 Electron Beam Perturbations

The space-charge parameter defined for a magnetically confined electron beam has been given as [40]:

$$Q_0 = \frac{\sqrt{2} I_b}{\pi \varepsilon_0 \eta^{3/2} V_1^{1/2} B^2 r_0^2}$$

$$= 1.378111 x 10^{-6} . \frac{I_b}{V_1^{1/2} Bpk^2 r_0^2} \qquad \ldots\ldots\ldots\ldots\ldots\ldots (2.64)$$

Here *Bpk* (Wb/m^2) is the peak value of the periodic magnetic field, r_o the mean beam radius, and I_b the beam current. For $Q_o << 1$ the magnitude of the perturbations in beam radius will also be small and the shape sinusoidal, whereas for large Q_o the correspondingly large perturbations are no longer sinusoidal. For small sinusoidal perturbations the maximum value of the normalised beam radius, *Rpk*, can be accurately estimated as follows :

$$Rpk = 1 + \frac{Q_0}{2} \qquad \ldots\ldots\ldots\ldots\ldots\ldots (2.65)$$

For larger values of Q_o the following relationship applies

$$Rpk^2 + \frac{1}{Rpk^2} - 2(1 + Q_0 \log_e Rpk) = 0 \qquad \text{.....(2.66)}$$

This transcendental equation cannot be solved exactly for *Rpk* in terms of Q_o. However, a fifth-order polynomial was easily generated which quite accurately relates these two parameters :

$$\begin{aligned} Rpk = {} & 9.151766x10^{-4}.Q_0^5 + 1.920485x10^{-3}.Q_0^4 \\ & - 4.487932x10^{-2}.Q_0^3 + 0.1366641.Q_0^2 \\ & + 0.4979578.Q_0 + 1.000053 \end{aligned} \qquad \text{.....(2.67)}$$

This characteristic is plotted in Fig.2.22. Also shown in Fig.2.22 for comparison is a plot of the relationship between *Rpk* and Q_o for purely sinusoidal perturbations. The difference in magnitude between the two characteristics is only about 2% at most, and this would imply that for Q_o not too large the perturbations in the beam radius remain reasonably sinusoidal over distance. For the following typical parameter values for the experimental tube the value of Q_o can be calculated :

I_o = 80mA V = 4500V r_o = 0.7mm Bpk = 0.1 Wb/m²

and we find that Q_o = 0.3356 and Rpk = 1.181. Judging from Fig.2.22 it can be seen that the curves (a) and (b) would

be very close for Q_o = .3356, and this implies that the waveform of the beam perturbations would be almost purely sinusoidal.

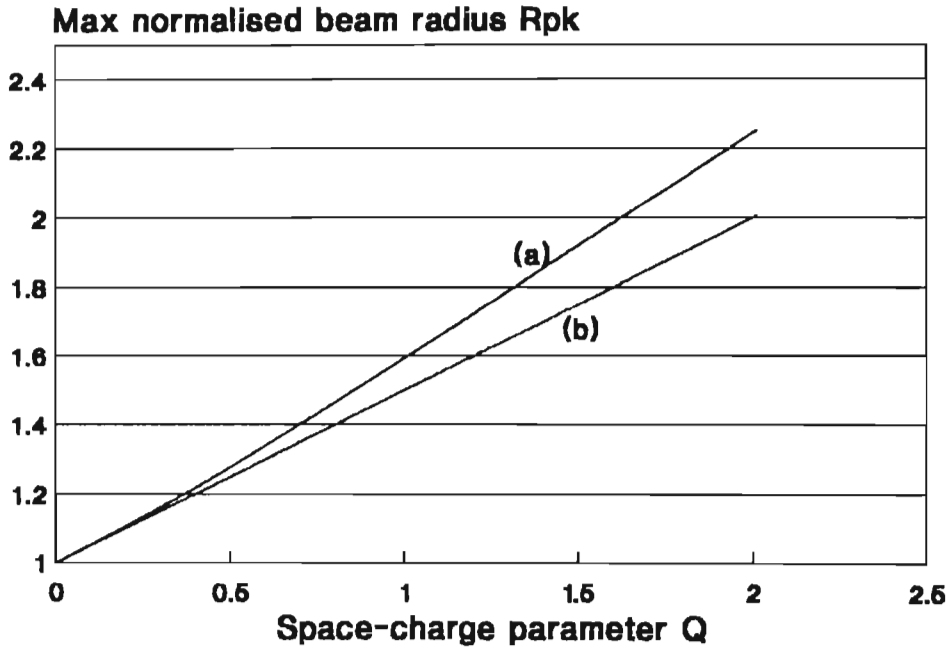

Fig 2.22 : Beam ripple for (a) an exact solution and (b) an approximate sinusoidal solution

CHAPTER III

TWT DESIGN

3.1. Introduction

The design of a helix TWT with PPM focusing had earlier been undertaken, before any simulation facility existed which would have aided the design of the tube. Certain broad objectives had been in view at the time of the design, and these were briefly :

Small-signal gain:		30dB
Centre frequency :		7GHz
Frequency band	:	6GHz - 8GHz
Slow-wave structure :		wire helix
Type of focusing	:	PPM
Beam voltage	:	4500V
Beam current	:	80mA
Construction	:	metal/ceramic

With time many of the design details changed as new and improved components were introduced into the tube, but the basic objectives remained the same.

The assembly drawing of the final design of the TWT is shown in Fig 3.2.

3.2. Electron Gun Design

The electron gun had begun as a standard Pierce gun of metal/ceramic construction with a perveance of .265μPervs. Some experimental versions were made and their performance evaluated, while the necessary skills required for fabricating metal/ceramic electron guns were growing and developing with each successive attempt. As the design progressed certain changes and refinements were implemented, and these are discussed below. In Fig 3.1 the electrode arrangement of the final electron gun design is shown.

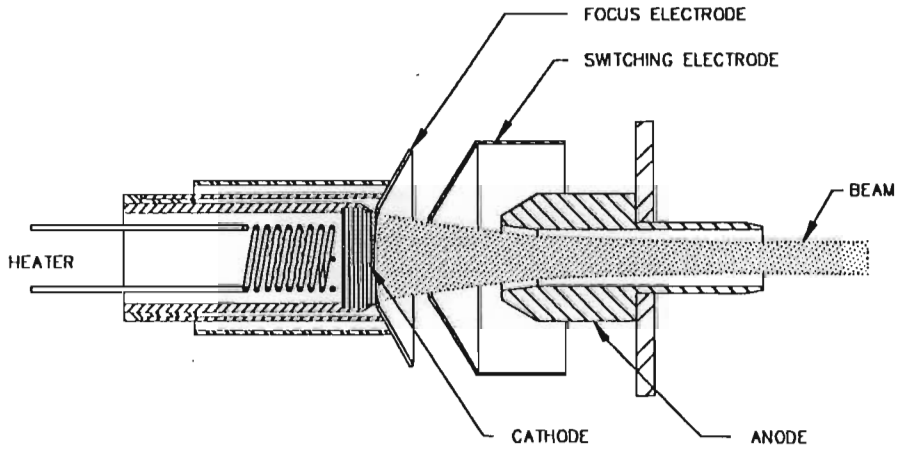

Fig 3.1 : Electron gun design showing electrode arrangement

3.2.1 Dispenser Cathode

The nickel oxide-coated cathodes used in the first models of the electron gun were replaced later by the more robust 'S' type dispenser cathode which is less vulnerable to poisoning and ion bombardment, and offers longer life.

The cathode comprises a porous pill-shaped tungsten matrix 5mm in diameter, machined firstly to the desired spherical radius of curvature, and then impregnated with 4:1:1 mixture (a molar ratio of four parts barium oxide to one part calcium oxide and one part alumina powder) by heating in an induction furnace. The cathode pellet is then mounted in a cathode holder machined from molybdenum, and the thin-walled side of the cathode holder is crimped to grip the cathode pellet. A thin-walled molybdenum cylinder supports the cathode holder and the impregnated tungsten matrix, and the tungsten heater, double-wound in order to minimise the stray magnetic field linking with the cathode surface, is mounted inside the cathode cylinder.

The operating current density is .41A.cm^{-2}, and this is quite low compared with saturation current densities achieved of 17.6A.cm^{-2} at 1140°C$_B$, 9.5A.cm^{-2} at 1060°C$_B$, and 6.7A.cm^{-2} at 1025°C$_B$. These temperatures, expressed as °C$_B$, are brightness temperatures as measured by an optical pyrometer. The measured Richardson work function is within 3 percent of the minimum value of 2.03eV expected from this kind of cathode.

3.2.2 Modulating Electrode

The first electron guns made employed a standard Pierce geometry. The potential on the focus electrode, nominally the same as the cathode, could be adjusted slightly positive or negative to optimise the focusing of the electron beam to achieve a minimum beam radius of .75mm just beyond the anode aperture.

Current distributions, measured at the beam minimum using a beam analyser, appeared to be far from uniform across the beam cross-section. The current density peaks sharply at the beam axis, falling away quite rapidly towards the edge of the beam. Initially, it was thought that this

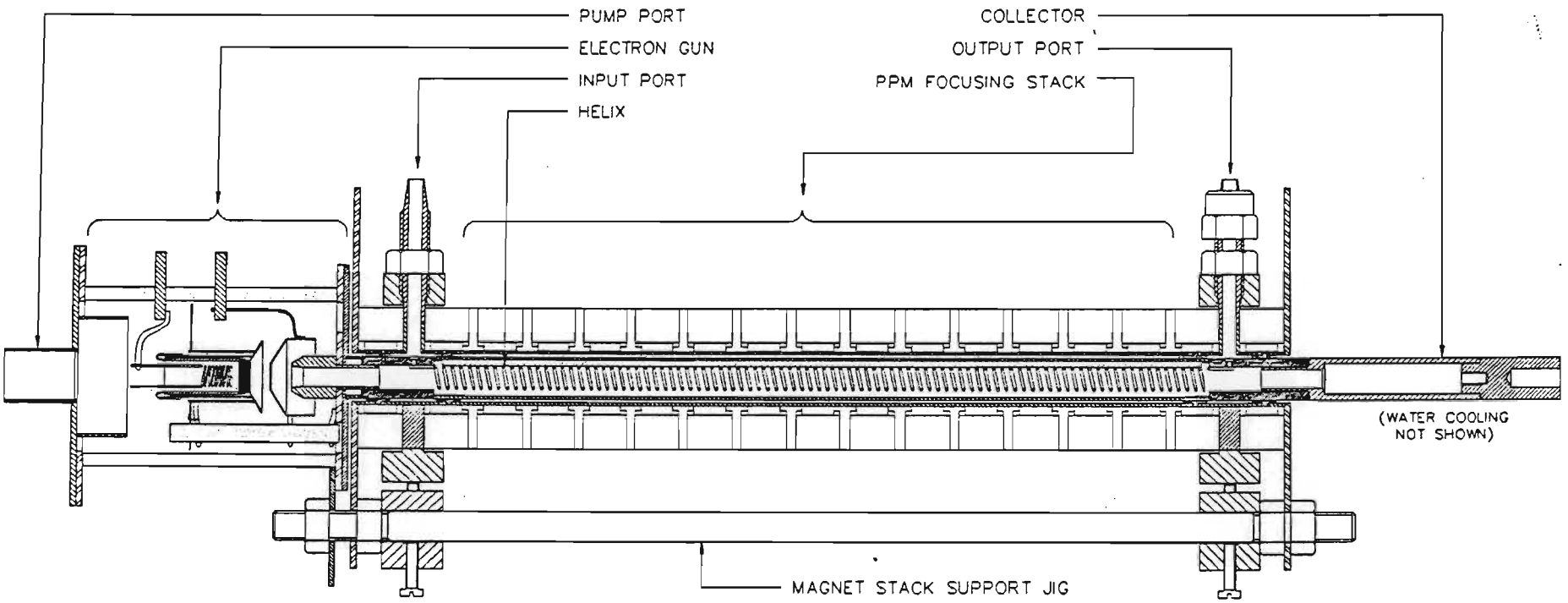

Fig 3.2

UNIVERSITY OF NATAL	
DEPT. OF ELECTRONIC ENGINEERING	
TITLE: TWT ASSEMBLY (LP8)	
DRAWING NO.: FCTA 720	PROJ. LEADER: H.L.NATTRASS
SCALE:	DRAWN: B.D. FOULIS
MATERIAL:	DATE: FEBRUARY 1993

current density profile would mean poorer interaction with the helix and thus lower tube gain, and some improvements in the current density profile were therefore sought. It was further thought that by modifying the electron gun geometry this objective might be achieved.

Control over the beam current is difficult in a standard Pierce gun, especially without defocusing the beam and aggravating interception by the helix and anode. The perveance of a Pierce gun is fixed by its geometry. Cutting off the beam current was achieved only by biasing the focus electrode very negative with respect to the cathode, by about 900 volts, and this was achieved only by employing an extra power supply.

Adding an electrode mounted at some intermediate position between cathode and anode, shaped in such a manner as to minimally disturb the equipotential profiles between anode and cathode, suggested the possibility of more effectively controlling the current,[10]. The electrode would be biased at a potential positive with respect to the cathode and, since the electrode is not expected to draw any current, the bias required could be derived from a simple voltage divider dividing the voltage between cathode and anode. The ideal bias would not disturb the potential distribution between cathode and anode. Reducing the bias on the modulating electrode to zero, i.e. to cathode potential, the electric field at the cathode surface due to the anode would be reduced practically to zero and very little current would be drawn.

In practice, the modulating electrode not only provided a means of cutting off the beam (reducing the current to about 3% of the full beam current) but also a means of adjusting the gun perveance somewhat above and below the nominal value of .265μPervs with little defocusing of the beam.

3.3 The Slow-wave Structure

The decision was made initially to use a tungsten wire helix as the slow-wave structure. The mean helix radius was fixed at 1.75mm, considerably larger than the nominal beam radius of .75mm, but this was largely to ensure that very good beam transmission would be achieved, although this might be at the expense of optimum interaction between beam and helix.

The pitch of the helix was decided upon by matching the d.c. beam constant at 7GHz to the phase velocity of the helix, neglecting the opposing effects of the dielectric loading of the helix support rods and the inductive coupling effect of the molybdenum tube barrel. The dielectric loading would tend to increase the value of the propagation constant of the helix by the square root of the effective dielectric constant of the region between helix and tube barrel, while the inductive coupling between tube barrel and helix would tend to reduce the value of the propagation constant. The pitch ultimately selected was 1.41mm.

A factor that does to some extent influence the behaviour of the helix is the diameter of the helix wire. The value chosen eventually was .5mm.

Three ceramic support rods were used to support the helix firmly within the tube barrel. These rods are 1mm in diameter and are of high purity alumina. The tube barrel is a molybdenum tube with an inner diameter of 6mm.

In the final version of the TWT (LP10) the helix dimensions were altered [9] in an attempt to improve the interaction between the beam and slow wave structure. The mean helix radius was reduced to 1.25mm, the diameter of the support rods increased to 1.5mm, while the pitch was

adjusted to a new value of 1.00mm, found by simulating the propagation constant for the old slow wave structure and then adjusting the pitch in the new structure until similar values were obtained.

3.4 Attenuator Design

Various ideas were considered for the design of the attenuators but difficulties were frequently encountered when it came to fabricating them. Eventually, a design [9] was adopted which involved forming a very thin layer of molybdenum on the centre section of each of the three dielectric support rods. Molybdenum was chosen for stability and for its refractory properties, and also because its expansion coefficient is not very different from that of alumina. The coated section is approximately 40mm in length, and the conductivity of the layer is not uniform over the length but is made to vary in an approximately sinusoidal fashion, rising from zero at one end to a peak value at the centre, and then falling again to zero at the other end. This distribution in the conductivity of the molybdenum layer was implemented in order to achieve the best possible matching of the attenuator to the helix impedance and thus to minimise internal reflections.

Forming the molybdenum layer was performed using an electron beam welder. A molybdenum target is bombarded by the electron beam, vapourising the metal. The dielectric rods are rotated slowly near the molybdenum target, and a layer of molybdenum is slowly deposited. The amount of molybdenum deposited is quite critical in determining the degree of attenuation achieved, and the correct thickness is found by trial and error. Too much metal deposited was also found to lead to flaking off of the layer, and it was thought that this was due to slight differences in the expansion coefficients of molybdenum and alumina.

The attenuators were evaluated on a network analyzer [9] after assembling the helix and rods into the tube barrel. S-parameter measurements were performed to obtain the through-loss, which is almost entirely the loss of the attenuator. The goodness of the attenuator impedance match to the helix was assessed using time domain techniques on the network analyzer, which permits discontinuities in the slow-wave structure to be separately and individually measured. Measurements showed that attenuations over a wide frequency band of up to 50dB could be quite routinely achieved, while the reflection coefficient (estimated from time domain plots) at the interface between attenuator and helix was about .04, corresponding to a return loss of 28dB.

3.5 Design of the Low-Profile TEM Connect

One of the requirements defined earlier on for the TWT had been that the tube should be easily discarded at its end-of-life without discarding or cracking the magnet stack. The magnet stack was expected to remain a fairly costly component, and any further work on it such as reassembly of the stack after remagnetising would simply add to the cost. Frequently, in many tubes, the magnet stack becomes captive to the TWT because of the high profile of the port connections. A means was therefore sought which would allow easy separation of tube and magnet stack without either suffering any damage. The low-profile TEM connect seemed to be the answer [9]. The TEM nature of the connect would also make it fairly wide band.

The molybdenum tube barrel terminates at each end in a short section of alumina ceramic tube of the same outer diameter. The ceramic sections are joined by active brazing to the tube barrel. In each piece of ceramic a single hole of 1.5mm diameter is drilled through its wall, and the end of the helix , coming out of the last turn of

the helix, terminates in the hole without protruding through. The hole is sealed and the end of the tungsten wire firmly gripped in place by active brazing material (an alloy of silver, titanium, and copper) such that a low-profile button remains in the sealed hole at the end of the helix. A coaxial connection can then be made externally to the connect, while the tube barrel forms the ground return. Both input and output connections to the helix are practically identical.

Practical difficulties encountered with this design mainly involved achieving good sealing of the metal-ceramic joints against atmosphere, and also the fact that the TEM connect in the ceramic represents a considerable capacitive susceptance at each end of the helix, and this makes good impedance matching over a wide band rather difficult. A possible solution to this, which could perhaps be the subject of further investigation, would be to replace the ceramic with a ceramic of lower relative permittivity loaded with ferrite material to raise the relative permeability to a value similar to that of the relative permittivity. This would have the effect of imparting to the short ceramic section a higher value of characteristic impedance, much closer to 50 ohms, and therefore easier to match over a wide frequency band.

3.6 Collector Design

The collector is machined from molybdenum [9] and is intended to be water-cooled. It is hollow in order to receive the beam, and is active brazed to the ceramic tubular section containing the output TEM connect. Water-cooling is effected by a threaded hole in the other end of the collector through which the water flows at a regulated rate. The power dissipated in the collector is 360 watts, since the collector is not operated in depressed mode. Operation in depressed mode would have considerably

reduced the power dissipated and improved the efficiency of the TWT but would have required an extra power supply which was not available at the time.

Some redesign of the collector would have been undertaken if opportunity had presented itself early enough. The collector was observed under d.c. conditions of operation to glow a dull red, especially the front end, and it appeared that the beam expanded very rapidly as it approached the entrance to the collector, striking the inside wall very near the opening. This part of the collector is furthest from the water-cooling and nearest to the metal-ceramic joint, so this was some cause for concern. Under pulse conditions, where the duty cycle would be between 1 and 10%, the power dissipated would be much lower and there would be no danger to the tube.

3.7 Design of the PPM Magnet Stack

The PPM stack comprises a periodic design of 17 sections [9], using uncracked Alnico 8 rings, and is based on an earlier experimental design [44]. It is designed to focus a 4500V 80mA beam. The optimum field strength for this case is approximately 450 Gauss(rms), or a peak value of 636 Gauss, which would be equivalent to the Brillouin field. Earlier designs of the magnet stack used peak values of 700 Gauss, only slightly above the Brillouin value. In the final version of this design the stack was magnetised up to 1000 Gauss, representing the maximum level of magnetisation possible with Alnico 8 before saturation sets in. This probably caused the beam to be somewhat over-focused, especially in those situations where the beam current was reduced well below 80mA. However, simulations which were run using a MATLAB differential equation-solving routine [9] showed that the beam would be reasonably well focused in the centre of the beam where the current density is highest, but poorer

at the edge of the beam due to the lower current density, possibly leading to excessive ripple for the outer electrons. Earlier measurements conducted on a tube with a helix of 1.75mm radius containing a beam of 4500V 79.5mA showed a 99% beam transmission from anode to collector. Later, using a helix of 1.25mm radius and the same magnet stack the beam transmission dropped to 90%.

CHAPTER IV

AN AUTOMATED TEST FACILITY

4.1 Introduction

The design and fabrication of an experimental TWT immediately gives rise to the need for some facility by which such a device could be extensively tested and evaluated. The test system would be designed keeping the following considerations in mind :

a) it should be inexpensively and cost-effectively designed and constructed, considering the limited funds available

b) it should enable accurate measurement of the most important TWT parameters using simple methods and techniques, reducing human error as far as possible.

c) measurements which may require much time-consuming repetition or many steps should be preferably executed under control of a computer in order to reduce the tedium and minimise the likelihood of human error. Logging and treatment of the data should also be automated as far as possible. Measurement and logging of data would therefore be much more rapid, reducing the effects of nuisance variables such as, for example, thermal drift.

d) the measurement capability of the test system should address both d.c. and RF TWT parameters, under conditions of continuous or pulsed operation, keeping in mind that initial measurements on the experimental tube would most likely take place when the tube is still on the pump being outgassed and the PPM magnet stack still to be optimally adjusted for minimum helix interception.

4.2 Requirements for TWT Testing

4.2.1 D.C. Parameters

By d.c. parameters is meant those tube parameters of voltage and current which are not functions of time, although they may be evaluated under pulse conditions. The following d.c. parameters would need to be monitored continuously while the tube is on the pump, especially during activation of the cathode and subsequent alignment of the PPM magnet stack :

a) cathode current and voltage
b) heater current and voltage
c) anode current, helix current, and collector current

These parameters would be monitored under pulse conditions, especially during the early phases of activating the tube, in order to minimise the possibility of arcing while the tube is out-gassing, and also to eliminate the risk of excessive dissipation in any sensitive parts of the tube such as the helix. For activation of the cathode a low, adjustable, value of cathode voltage may need to be applied continuously for a period of time, with heater power also being varied. Short pulses at a low duty cycle will need to be employed at the full cathode voltage during alignment and adjustment of the PPM stack. Thereafter, the beam transmission can be measured,(the percentage of the cathode current that reaches the collector), varying the cathode voltage as parameter. This could be done under d.c. or pulse conditions.

Under conditions of RF drive certain d.c. parameters may vary, and these should be monitored. For example, as saturation of the output signal is approached the helix current will increase.

4.2.2. RF Parameters

The following RF parameters would be measured :

a) small-signal power gain, as a function of certain parameters such as frequency and beam current and voltage

b) saturated power gain and output power, as functions of frequency and beam current and voltage

c) small-signal instantaneous bandwidth, saturated bandwidth,

d) noise figure,

e) spectral purity over a wide band, evaluation of harmonically and non-harmonically related spectra, with frequency as a parameter. Harmonic levels as a function of output power levels. Close-in sideband levels.

4.3 Design of the Test Facility

Driving the experimental TWT into saturation would require a wideband microwave source of adequate power over the band 2 - 12GHz. Considering that the experimental tubes would be designed to have small-signal gains of nominally 30dB (the saturated gain is some 5 or 6dB lower,[42]) and the saturated power was anticipated to be between 10 and 50 watts, the minimum power required from the source can be estimated :

$$Ps(min) = +47dBm - 30dB + 6dB = +23dBm$$

A synthesized microwave source was available in the form of an HP8340B synthesized signal generator, but the levelled output power cannot be expected to much exceed +13dBm across the full frequency band of interest. A

wideband power amplifier was required to raise the generator output power to at least +23dBm, preferably +30dBm (1Watt). An approximate specification for the amplifier was as follows :

Frequency band : 2 - 12GHz

Saturated Gain : 17dB

Power output : 1 Watt (max) at 1dB compression

Certain difficulties presented themselves at this stage, firstly, that the HP8340B was dedicated to the network analyzer and therefore not really available to be moved to the laboratory where the TWT's would be on the pump awaiting testing. Secondly, the power amplifier proved difficult to source and also very expensive. A new strategy was required by which an acceptable input signal level could always be achieved at the TWT input, and this was to configure the TWT as an oscillator. The loss in the feedback loop could be adjusted in order to control the level of oscillation and hence the degree of saturation, while the frequency of oscillation would be set by a tunable transmission cavity included in the feedback path.

4.3.1 Description of the Measurement Set-up

The measurement set-up is shown in Fig.4.1 and will now be described without too much detail. A full description of the system can be found elsewhere [9]. Connected directly to the input and output ports of the TWT are two bias tees which permit the helix current to flow from the helix into the measurement circuit without disturbing the flow of RF power. At the output of each bias tee is connected a wideband coaxial circulator. The two circulators

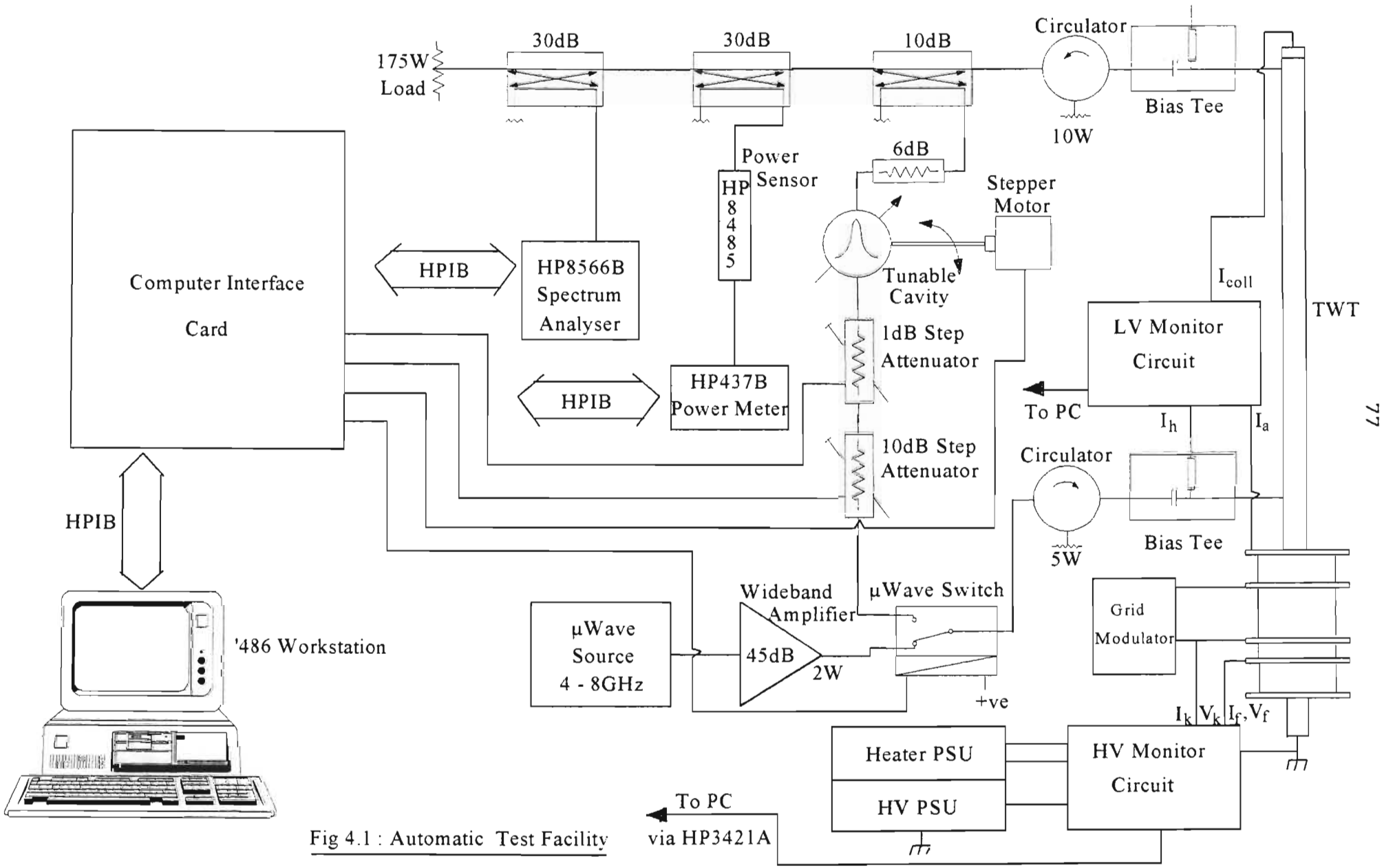

Fig 4.1 : Automatic Test Facility

efficiently match the bias tees to 50 ohms, shielding the TWT ports from mismatches in other parts of the measurement circuit. The circulators are specified to handle at least 50 watts, and the circulator in the TWT output circuit is terminated with a 10 watt termination capable of absorbing the reflected power from other elements in the circuit. The output signal passes through three broadband directional couplers connected in series before being terminated in a large 175 watt load. The first directional coupler is a 10dB unit, and energy is taken from its coupled port through a high Q transmission cavity, through a 1dB and a 10dB step attenuator, and through a coaxial microwave switch back towards the TWT input. This forms the feedback path.

The coaxial resonator is tunable mechanically by means of a shaft driven by a stepper motor and its high Q controls the frequency of oscillation, normally near to the natural resonance of the cavity but also influenced by the large phase shift in the TWT. The frequency setting for the resonator is determined from a look-up table in the computer relating the number of stepper motor increments from the mechanical stop (lowest frequency) to frequency.

The two attenuators are wideband step attenuators with magnetic latching, not requiring d.c. power to hold them in any particular selected state, and can provide attenuations from zero to 81dB in steps of 1dB. Attenuator settings are controllable directly from the computer. The default setting is maximum attenuation (81dB).

Connected in the TWT input path is a microwave SPDT switch which controls the mode in which the system will work. In the default state, which is the amplifier mode, the switch connects the TWT input to the output of a broadband solid-state 2W amplifier which is driven from a 4-8GHz microwave

source. The other state closes the feedback loop for the oscillator mode.

The output signal at the TWT output is sampled from two 30dB directional couplers whose coupled ports are respectively connected to a digital power meter (HP437) and a spectrum analyser (HP8566B). Both instruments are under HPIB control by the '486 computer. Accurate power measurements are performed by the power meter and these are relayed to the computer for calculation of output power and gain. The spectrum analyser provides information on the spectrum which the power meter cannot do.

Monitoring of the helix, anode, and collector currents is performed by the LV Monitor circuit which relays the information to the computer. Installed in the computer is a PC30 card which accepts up to 16 analogue channels. Monitoring of the cathode voltage and current, modulating electrode voltage and current, and heater voltage and current is performed on the HV Monitor circuit and this information is relayed via two HP3421A data acquisition units and an optical link to the computer. This link is necessary because the HV circuit operates at cathode potential(-4500V).

The computer monitor is configured as a control and display panel, being divided into a number of smaller displays, each representing a particular parameter. The status of the system can be determined at a glance. The status is updated every four seconds.

Losses in the system as a function of frequency are measured during calibration and this information stored in the computer so that TWT gains and power levels can be accurately determined.

4.3.2 Helix Current

The helix current will be measured at the bias connection to the bias tee in the output circuit. The output terminal of the tee is taken provisionally via a 10 ohm resistor to ground, so that the natural voltage of the helix will be near zero volts. Nevertheless, if required the helix could be held at some other potential, either positive or negative up to a value of 500 volts. This could be done by inserting a floating variable bias of the desired polarity between the terminal of the bias tee and the 10 ohm resistor. The current will be measured across the 10 ohm resistor to ground as a voltage. Monitoring the helix current is important as an indicator of the degree of perturbation of the beam when the tube is being driven as an amplifier into saturation, and also as a measure of how well the beam is focused by the PPM magnetic stack. Automatic monitoring of the helix current is also important for the safety of the tube, allowing almost immediate shut-down of the tube power supply when the tube is at risk.

4.3.3 Small-signal Gain

The small-signal gain at a particular frequency can be determined by adjusting the level of attenuation in the circuit in 1dB steps until the onset of oscillation is reached. The small-signal gain, to within approximately +\-0.5dB, is then the selected value of attenuation plus the fixed loss in circuit comprised mainly of the resonator insertion loss near resonance and the coupling ratio of the 10dB directional coupler. The fixed loss will be somewhat frequency-dependent but can be measured at intervals in the frequency spectrum and the values then stored in the computer as a calibration. The minimum gain in the tube for which oscillation will take place will be that value for which the step attenuators are both set to

zero, and the gain is then equal to the fixed loss in the circuit. The fixed loss has a minimum value equal to the sum of the coupling ratio of the 10dB directional coupler and the insertion loss of the tunable cavity resonator, plus other small losses. This fixed loss has a minimum value of approximately 18dB ; tube gain will not be measured for values below this.

4.3.4 Large-signal Gain

The large-signal gain at a particular frequency and level of output power can be determined by adjusting the attenuation level in circuit until that value of peak output power is measured at the power meter, keeping in mind though that the power measured by the power meter is the total signal power including all harmonics. The total harmonic power may, under conditions of severe saturation, exceed the power of the fundamental. The HP8566B spectrum analyzer should therefore be used to obtain the ratio's of the harmonics to the fundamental so that the necessary corrections can be made to the power meter reading. These corrections could be made automatically under software control. Summing the fixed loss and the selected attenuation gives the large-signal gain at that corrected output power level and frequency of the fundamental. The levels of the fundamental and the harmonics will be monitored on the HP8566B spectrum analyzer, but a drawback at present is the limited bandwidth of the 30dB directional couplers (4GHz - 10GHz). One way of improving the measurement of harmonic levels is to do this under pulse conditions with the duty cycle set to nominally 1%. The 175W load and the two 30dB directional couplers are then removed and replaced by a 5W 30dB dc -18GHz attenuator connected to the output of the 10dB directional coupler. The output of the attenuator is connected to the HP8566B spectrum analyzer, or to the power meter. The harmonic levels can then easily be assessed over a much

wider bandwidth by direct comparison with the fundamental component.

4.3.5 Oscillator/Amplifier Mode Selection

A microwave SPDT switch in the feedback path to the TWT input enables either the feedback signal to be selected, setting up oscillation, or an external input, placing the TWT in an amplifying mode. Selection of the mode will be under software control, furthermore in the event of an emergency and the tube being put at risk, the amplifying mode will be automatically selected. With no signal being present at the external input , the tube will be in a no-signal condition, and any high-level oscillation will cease within a few milliseconds. Through the circulators the input and output ports will be correctly terminated in 50 ohms.

4.3.6 Noise Measurement and Spurious Signals

If the external port selected by the microwave SPDT switch is correctly terminated in 50 ohms and no signal applied, the output signal from the TWT will in theory be an amplified noise spectrum. Knowledge of the small-signal gain of the TWT over a particular frequency band will permit the spectral noise density to be determined and hence the noise figure. The spectral noise density will be evaluated on the HP8566B spectrum analyzer connected to the output port via the 5W 30dB attenuator :

$N_o = kTBGF$

where $k = 1.3805 \times 10^{-23}$ (Boltzmann's constant)

T = absolute temperature in degrees Kelvin

B = RF (resolution) bandwidth of the spectrum analyzer

G = small-signal gain of the TWT

F = noise factor of the TWT

Two 30dB wideband directional couplers are connected in the output circuit. One coupled output is connected to the HP437B digital power meter via its HP8485A power sensor, and this enables accurate output power measurements to be performed once the path losses between the TWT output and the power sensor are determined. These losses will be frequency-dependent and will need to be measured at a number of points across the frequency spectrum of interest. Once determined they will be unlikely to vary significantly with time and the values could be stored in computer memory. The output power displayed by the power meter will be the average TWT output power. When operated under pulse conditions, if the duty cycle is known and is entered into the power meter, the power meter will display the peak output power.

A second coupled output, 30dB down from the main signal path, is connected to an HP8566B spectrum analyzer. Setting the instrument up under HPIB control with the correct frequency span and centre frequency, the appropriate RF and video bandwidths, and suitable reference level, will permit examination and interpretation of the power spectrum. In the absence of a suitable pulse frequency counter, which could not be acquired because of insufficient funds, examination of the spectrum analyzer display will provide reasonably accurate information about the frequency of oscillation. The spectrum analyzer functions will be controlled from the computer and frequency data extracted from the c.w. or pulse spectrum. Examination of the close-in sidebands, however, probably will not be performed automatically, and results will be taken manually and interpreted. Phase modulation spectra can be interpreted and the sensitivity

of the TWT output phase determined in terms of electrode voltage fluctuations. Also, non-harmonically related spectra could be examined and analyzed. Lastly, in the absence of signals the spectral noise density could be measured as a function of frequency, and the noise figure determined.

4.3.7 Bias Tees

Some means of separating the d.c. and RF signals at the TWT input and output ports is required, since measurements are to be carried out on both the d.c. helix current and on the RF signals. The RF circuits should not have a d.c. path to ground which would complicate helix current measurement, while the helix current circuit should not disturb any measurement of the RF signals, and meeting this requirement is the task of the bias tees. The following specification was drawn up for the bias tees :

Operating freq. band : 2 - 12GHz

Lower cut-off frequency : <1000MHz

Max VSWR (2-12GHz) : 1.4 : 1

Input\output Impedance : 50 ohms

Max. transmitted power : 50 watts

Max. bias voltage : 500 volts

The search for a commercial off-the-shelf item was not successful, mainly on the grounds of inadequate power handling ability (a few watts) and the bias voltage on such units being too low (usually only 50V for solid-state applications), although in other respects performance

would have been excellent. The design of a suitable bias tee was therefore undertaken, and the result was acceptable for the most part, although the VSWR was in places a little higher than desired. The requirement for reasonably low VSWR at the TWT ports arises from the tendency for the tube to oscillate if the reflections at its ports are excessive. Generally, as a guideline, the combined return loss seen by the TWT at the designated port and that of the sever or attenuator should be less than the available small-signal gain in that section of the tube. Anticipating that the return loss at the attenuator might be poor at certain frequencies in the operating band, the minimum return loss to be seen at each port was set at 15dB, equal to the expected small-signal gain. Measured results showed that the return loss exceeded the 15dB goal over most of the band , between 650MHz and 9GHz, but above this the return loss degraded in places to about 10dB. Power handling was not tested.

4.4 Calibration of the Test Facility

Calibration of the test facility for the purpose of measuring the performance characteristics of an experimental TWT is obviously of great importance. Errors introduced during calibration will obviously be reflected directly in the measurement data. This calibration was performed by Vassilopoulos [9]. The TWT was bypassed and the cables to the input and output brought together so that the insertion loss is 0dB. The linearity of the system was tested by inserting a fixed attenuator (5dB) and verifying a 5dB fall in signal level over a wide band as read by the power meter. Shown in Fig 4.2 below is a plot of the calibration using the 5dB attenuator as a reference. On average, across the band 4 - 8GHz, the fall in the power meter reading is 5dB. The rather severe fluctuations in the calibration (which will cause uncertainties in the gain measurements) are mostly likely

due to VSWR problems in the cables and the bias tees. The semi-rigid cables are quite long, and it is uncertain how well the coax connectors were fitted. The uncertainty in the calibration amounts to +/-3dB.

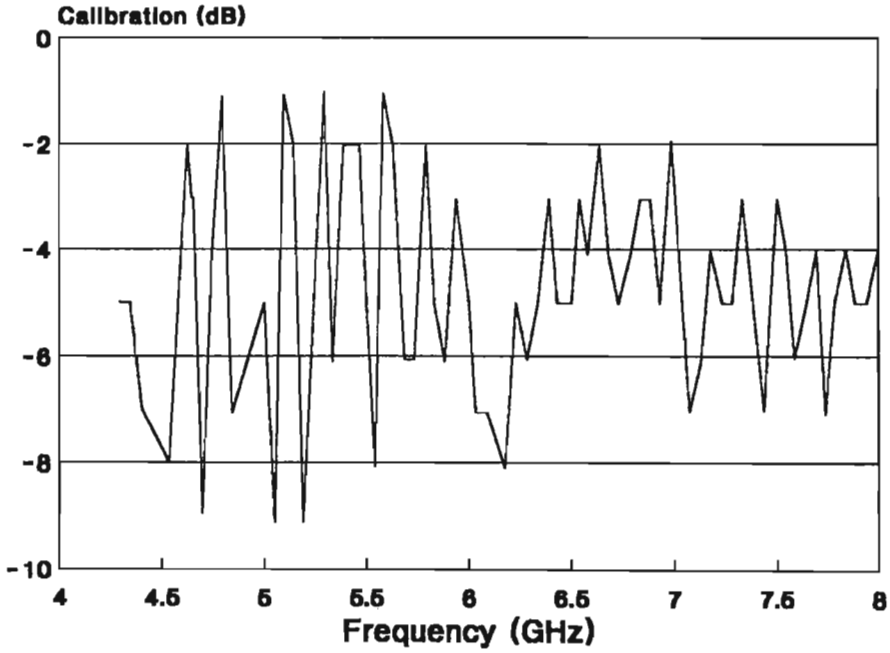

Fig 4.2 : System calibration using a precision 5dB attenuator

CHAPTER V

SIMULATIONS AND MEASURED RESULTS

5.1 Introduction

In this chapter certain facets of the measured small-signal performance of the experimental TWT LP10 are examined and compared with simulated results. Due to the unstable behaviour of the tube some emphasis has been placed on analysing and simulating this aspect and comparing it with what was actually observed.

In order to validate the computer model, a commercial TWT of specified performance was taken and analysed, and these results are also presented and discussed.

5.2 The E3510 MiniTWT

A commercial TWT was obtained by the CSIR, opened up, and certain internal dimensions relating to the slow-wave structure carefully measured. The measurement data was then made available for the purpose of this simulation.

The E3510 MiniTWT is manufactured by Elettronica S.p.a of Italy and is mainly intended for military applications in the X/Ku band, delivering a minimum of 40W CW in the band 6.7 to 17GHz. Constructional features include a metal-ceramic structure, PPM focusing (samarium cobalt magnets), dispenser type cathode, a high μ grid, and depressed collector operation.

5.2.1 Specification

The electrical performance characteristics are as follows:

	Symbol	Min	Max	Unit
Frequency range	F	6.7	17	GHz
Saturated output power	P_o	40	--	W
Saturated gain	G	50	--	dB

This performance is obtained within the following range of operating conditions :

Cathode voltage	E_k	-4.8	-5.2	kV
Cathode current	I_k	130	160	mA
Grid voltage				
- tube "on"	E_g	40	55	V
- tube "off"			-40	V
Grid current	I_g			
- tube "on"			40	mA
- tube "off"			0.1	mA
Collector current	I_{coll}		110	mA
Collector voltage	E_{coll}	50%E_k		V
Helix current	I_h		40	mA

No typical or maximum performance is given in the data sheet in terms of saturated gain and output power. Examination of data and specifications for other TWT's showed the same situation, no typical or maximum output power and gain. Similarly, gain-bandwidth curves do not generally seem to be published.

The computer model only treats the small-signal characteristics of the TWT. The minimum small-signal gain for the E3510 is estimated by adding 5dB [42] to the minimum saturated gain, i.e 55dB(min) at the band edges. TWT bandwidth appears to be characterised by a 2dB fall in

saturated power at the edges, and the minimum small-signal mid-band gain is therefore estimated as 57dB.

The operating conditions defined for the computer model were initially 4800V and 75mA for the beam. This was decided upon after concluding that the tube would still have to meet its specified performance at these minimum values. The minimum cathode voltage is 4800V, and the minimum beam current obtained by subtracting the maximum grid and helix currents from the minimum cathode current, a situation which could occur near the end of the tube's life.

5.2.2 Measured Data

Because the TWT had failed previously due to loss of cathode emission its performance could not be measured. However, the following data were obtained from physical measurements carried out on the tube :

Average helix radius :	0.59mm
Inner helix radius :	0.53mm
Average pitch :	0.678mm
Overall helix length :	200mm
Length of attenuators :	22mm,22mm,34.5mm
Inner radius of barrel:	1.5mm

The helix is a tungsten tape helix, wound with tape having a width of .357mm and an average thickness of .116mm. There are three attenuators spaced at intervals over the length of the helix, fabricated by depositing a very thin layer of molybdenum on the three alumina support rods. The molybdenum layers are tapered linearly in thickness to a maximum at the attenuator centre.

Tests were carried out on a network analyser to determine the combined attenuation of the attenuators, and the

matching characteristics of the ports. From the S11, S22, and S12 data polynomials were generated to simulate the attenuator loss and the reflection coefficients at the ports.

No information was available on the beam size, but this was estimated to be 75% of the available space inside the helix, i.e. 0.4mm. The focusing field was measured to be 2000 Gauss, or .2Weber/m^2.

The information thus obtained was sufficient to put together a model for this particular TWT.

5.3 Normalised Phase Velocity Measurement

Verification of the normalised phase velocity predicted by the model against measured data for a particular structure is important in confirming values for γ and β_1.

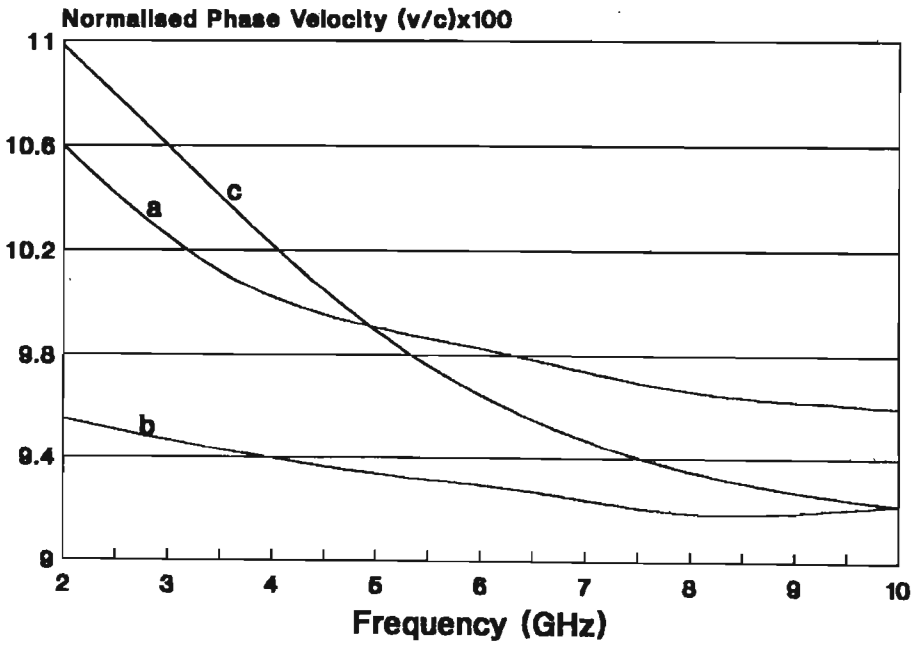

Fig 5.1 : Normalised phase velocity (v/c) with (a) Belohoubek,(b) Jain & Basu,and (c) this simulation

Belohoubek [43] has conducted phase velocity measurements on a helical slow-wave structure comprising a wire helix supported by three circular ceramic rods in a metal shell. The dimensions for the Belohoubek slow-wave structure are as follows:

a = 0.825mm, s = 0.0635mm, b = 1.499mm, p = 0.552mm, d = 0.61mm.

Jain and Basu [17] ran a comparative simulation of the normalised phase velocity on this particular slow-wave structure using their Approach II, and these results are shown in the plots of Fig 5.1. Their results are consistently somewhat lower than Belohoubek's measured data. The same simulation of the normalised phase velocity was then conducted on this slow-wave structure using Jain and Basu's Approach II [17], expecting that the same results would be obtained. However, this was not the case as may be seen in Fig 5.1. When the discrepancy was noted, the implementation in the program of Jain and Basu's Approach II was carefully checked, expecting that errors may have crept in, but none was found. Although the difference remains a bit of a mystery, the results achieved by this simulation do agree quite favourably with those of Belohoubek, the error being no greater than a few percent over a wide frequency band. A variant of the method of [17] was devised and has been described in Chapter II, and its results compared with those of Belohoubek in Fig 2.4, also being within a few percent of the measured values. This does generally tend to lend support to the Approach II method.

The axial propagation constant β_1 is inversely related to the normalised phase velocity :

$$\frac{k_0}{\beta_1} = \frac{v}{c} \quad \ldots\ldots\ldots\ldots\ldots\ldots [5.1]$$

where k_o is the phase constant for free space. This would suggest that the simulated axial and radial propagation constants for the structure would also be close to the actual values obtained by measurement.

5.4 Interaction Impedance

Initial estimates of the simulated small-signal gains of LP10 and the E3510 MiniTWT appeared to be too high compared with measurement or specification. Investigations finally highlighted the reason; use of a slightly modified free space sheath model gave values for the

interaction impedance which were unrealistically high, consequently inflating the gain. Jain and Basu [49] had produced a more complex model of the interaction impedance of a helical slow-wave structure, including the loading effects of the metal envelope and dielectric support rods. The structure they had analysed was practically identical to that of LP10, being a wire helix supported by three circular alumina rods in a metal envelope, having the same ratio of metal envelope radius to helix radius (c/a = 2.4). See Fig.2 of [49]. This permitted direct comparisons to be made, and this is shown in Fig 5.2. Also shown in Fig 5.2 is the interaction impedance for the E3510, based on a sheath model. Here the similarity in the structure is not quite so good, the main difference being that the E3510 uses a tape helix, not a wire helix as in [49]. However, it was felt that the comparison would still have some validity. What is evident in Fig 5.2 is that the interaction impedance is much lower than that of the

adapted sheath model, so it was decided to adopt the approach of [49] and adapt the calculation of the

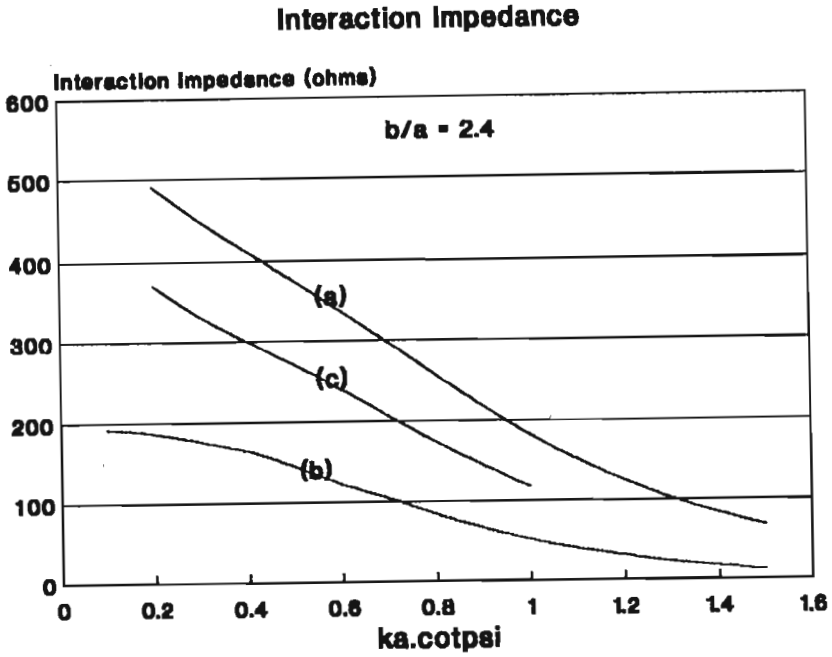

Fig 5.2 : Interaction impedance for (a), LP10, (b), Jain & Basu, (c), E3510

interaction impedance accordingly. The lower values of interaction impedance would mean lower values of C, and lower calculated gains.

5.5 Gain Measurements and Simulations

5.5.1 LP10

The operating point for the experimental tube LP10 was intended to be 4500V and 80mA. It was soon discovered that the tube was extremely unstable at this working point. Maintaining the cathode voltage at 4500V and reducing the cathode current progressively appeared to be the only way of getting the tube stable. Normally, with an electron gun of fixed perveance this would not have been possible, but in this case this was achieved by reducing the heater

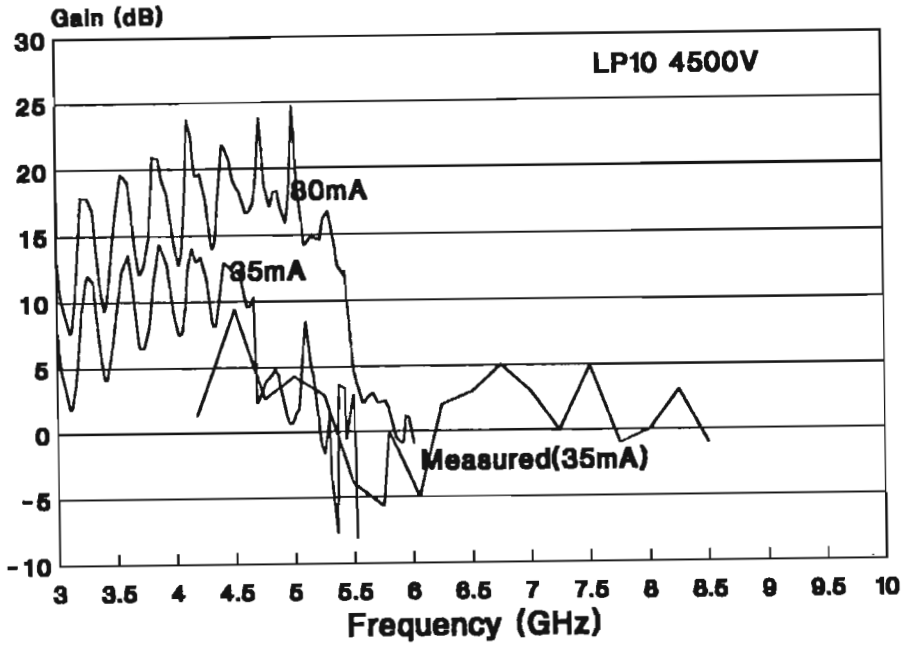

Fig 5.3 : Simulated gain for LP10 at 4500V, 35mA, and 4500V, 80mA, with measured values for 4500V, 35mA

power carefully until the cathode was running temperature limited and the beam current began to fall below 80mA. The electron gun was refocused as the current fell by adjusting the bias to the modulating electrode until very good beam transmission was again obtained.

The TWT was stable at 4500V 35mA so a gain measurement could be performed. Shown plotted in Fig 5.3 are the measurements taken at 4500V, 35mA, and also the simulated gain of the tube operating at 4500V 35mA and 4500V, 80mA. The severe ripple in the simulated gain characteristic suggests that quite considerable feedback still is present even when the gains are low. The measured gain also shows considerable ripple although the periodicity is not the same as in the simulation. This is most probably because the gains were sampled at different frequency intervals, the simulations every 50MHz or so but the measurements

every 250MHz approximately. At 35mA and between 4.5 and 5.5GHz the measured and simulated results agree reasonably well showing similar trends. Unfortunately, the signal source did not operate below 4GHz so measurements could not be performed there. Between 3 and 4GHz the model predicts that the TWT would still have gain. The peaks in the gain characteristic correspond to those frequencies where considerable in-phase feedback is present.

In an attempt to keep the tube stable while operating at higher beam currents, the beam voltage was increased in steps while maintaining the current near 80mA. At 5290V 89mA the tube was stable and no spectra were observed on the spectrum analyser. Plots of the measured and simulated gains are shown in Fig 5.4. At first, the model had been set up for 89mA 5290V, and its response seemed initially quite "dead" (as may be seen from curve (a) in Fig 5.4)

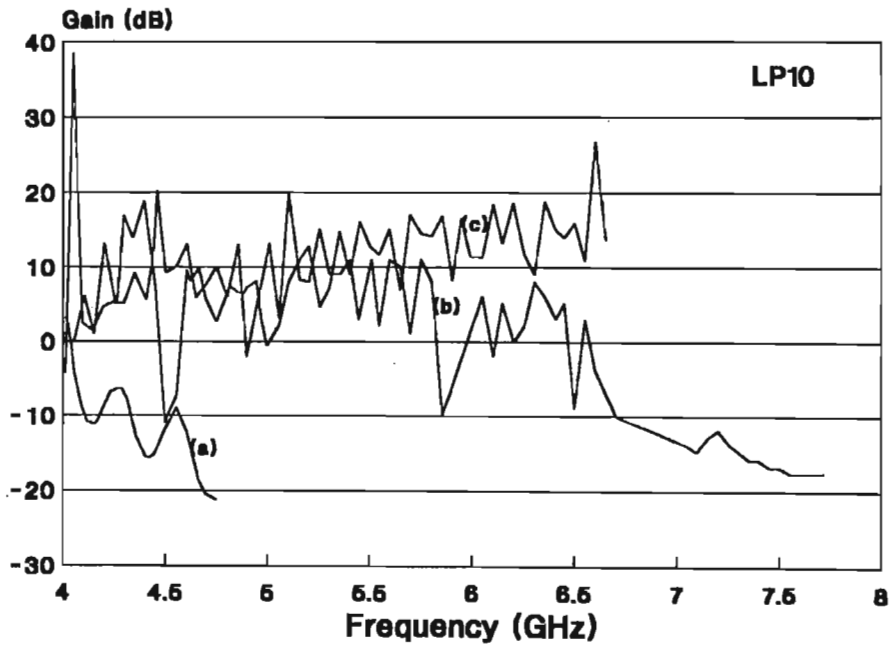

Fig 5.4 : Simulated gain at 5290V using 30dB attenuator,(a), measured gain at 5290V 89mA,(b), and simulated gain at 5100V 89mA, using 10dB attenuation,(c).

when, judging from the measurements done on LP10, there was obviously some activity and the tube had even been unstable at about 4.15GHz. After adjusting the voltage downwards to 5100V, while maintaining the current at 89mA, and having made a change to the attenuator in the model the tube sprang to life (see curve (c) in Fig 5.4). Vassilopoulos had earlier reported that during tests done on the "cold" LP10 on the test facility, it was found that the isolation between input and output ports was only about 10dB over a wide frequency range, very much at variance with the S21 measurements done on the cold LP10 on the network analyser where an isolation of between 25 and 30dB had been measured. By this time LP10 was on the pump station and could not be taken back to the network analyser for checking. So it was felt that there was some justification in replacing the 30dB attenuator in the model with one of about 10dB. Inspecting (c) in Fig 5.4 it may be seen that there is a strong tendency for instability at 4.05GHz, where at 5100V there is sufficient feedback to initiate oscillation. In practice, LP10 had been unstable at 4.15GHz until the voltage was raised to 5290V. In the model, raising the voltage to 5290V also has the effect of reducing the feedback at 4.05GHz below a level where oscillation could occur.

The gain characteristics of LP10, both measured and simulated, show a high degree of ripple, obviously due to high levels of internal feedback. The attenuation, which had been reduced to 10dB, was increased slightly to 14dB to see whether it would significantly improve the stability. The result is shown in Fig 5.5, and it looks similar except that the ripple has been somewhat reduced and the gain has fallen slightly. However, it is not on the threshold of oscillation as in the 10dB case.

The model predicts a gradual rise in gain beyond 5GHz, beginning to fall after 7GHz, whereas the measured results

show that the gain falls away rapidly after 6GHz.

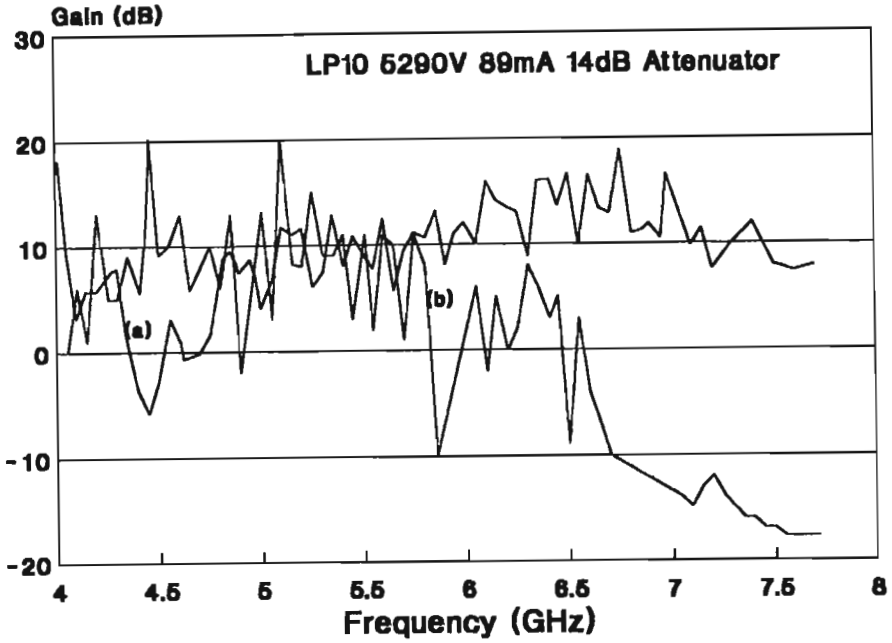

Fig 5.5 : Simulated gain at 5290V 89mA using 14dB attenuation,(a), and measured values at 5290V 89mA,(b)

5.5.2 E3510 MiniTWT

The E3510 TWT has been designed to operate as a saturated CW amplifier between 6.7GHz and 17GHz having a minimum saturated gain of 50dB. The gain of the device was simulated for different beam currents and voltages, and these are shown in Figs 5.6 and 5.7. below. The beam currents quoted are currents flowing throughout the interaction region of the tube, and do not include currents lost to electrodes such as grid and anode. Inspecting Fig 5.6 it may be seen that operating the tube at 4800V 75mA obviously would not meet even the minimum gain specification, while at 5000V, 95mA there is improvement, and at 5000V, 120mA it performs even better.

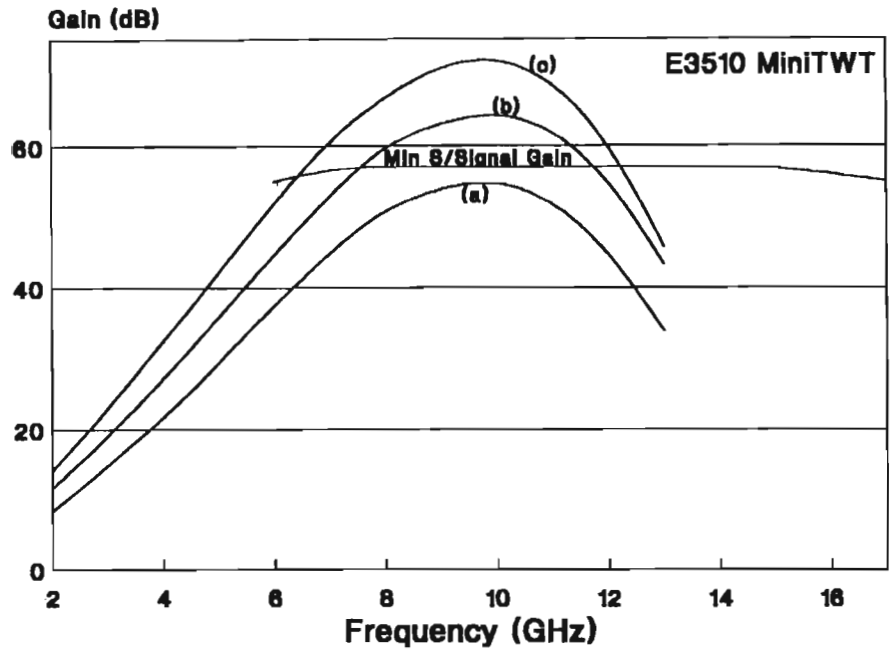

Fig 5.6 : Simulated gain plots for,(a),4800V 75mA (b), 5000V 95mA, and,(c) 5000V 120mA compared with the minimum gain specification

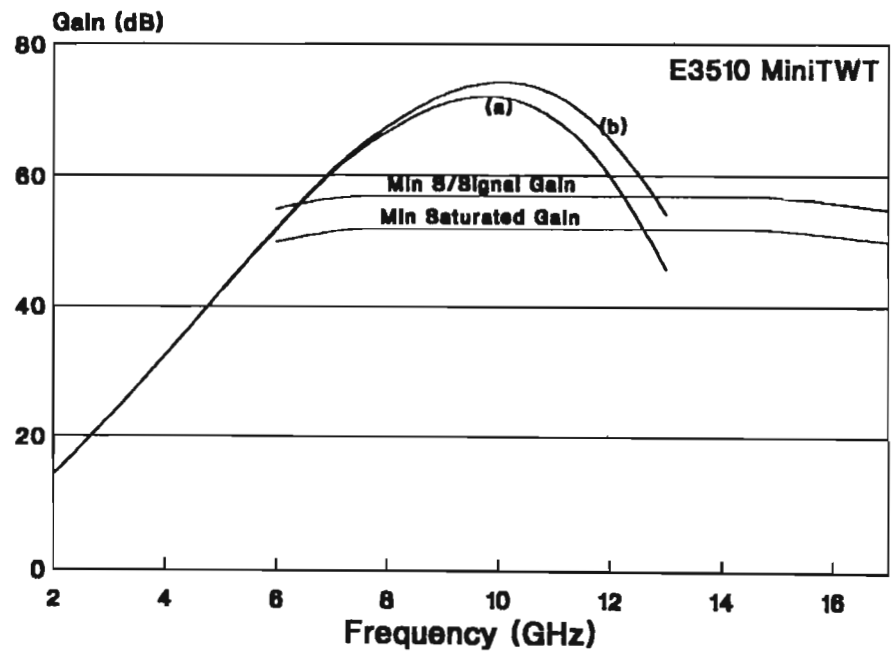

Fig 5.7 : Gain plots for (a), 5000V 120mA and, (b), 5200V 120mA, compared with minimum small-signal and saturated gain specifications

However, the high frequency performance is quite inadequate compared with its specification. In Fig 5.7 the saturated bandwidth (obviously wider than the small-signal bandwidth) can be estimated. At 5000V 120mA the saturated bandwidth is approximately 7.3GHz, lying between 6GHz and 13.25GHz. Increasing the beam voltage to 5200V while maintaining the beam current at 120mA improved the performance, adding about 500MHz on to the top end of the band.

5.6 Internal Feedback and Instability

a) Operation at 4500V

The output spectrum of LP10 was observed on the HP8566 spectrum analyser between 2 and 10GHz without any input signal being applied. Initially, operating at 4500V and 80mA, a large number of spectra were observed of varying magnitudes, showing the tube to be extremely unstable. As the beam current was reduced the number of spectra diminished until finally only one spectral line remained at 5.624GHz. This last spectral line disappeared as the beam current was reduced to 38mA, and below this the tube was always stable.

Using the internal feedback model developed for the TWT, the magnitude of the feedback in phase with the input can be predicted for various values of beam current as a function of frequency. Obviously, that part of the feedback signal which is in phase with the applied input signal is what can lead to instability. At 35mA the feedback nowhere reaches a value of unity (the minimum value at which the tube will become unstable) so the tube is stable. At 80mA considerable feedback is present and instability is likely at any one of a number of frequencies. The feedback reaches a maximum between 5 and 6GHz and instability in this band will be the most

persistent as the beam current is reduced. At higher beam currents the potential for instability increases to include frequencies above and below 5.71GHz.

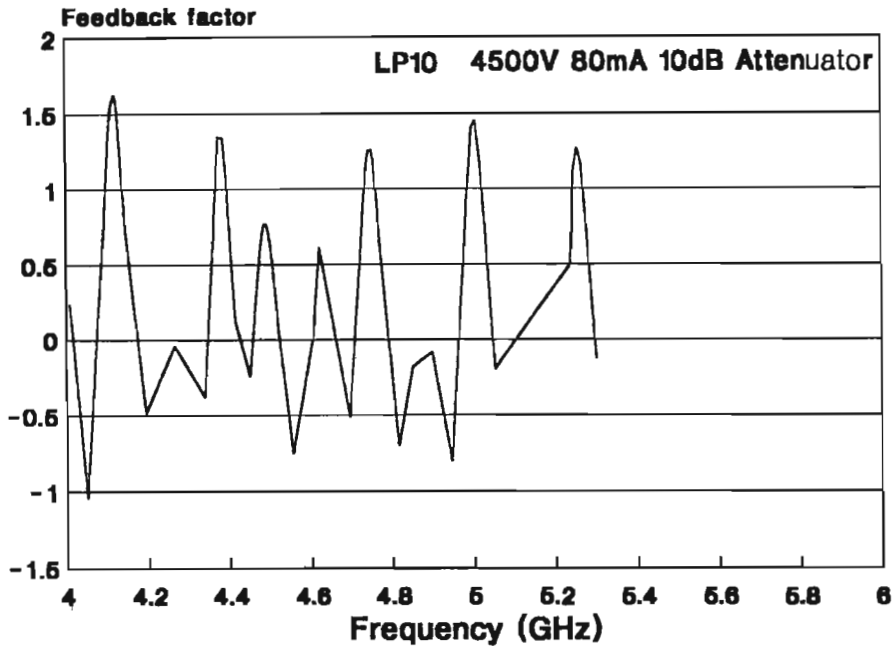

Fig 5.8 : Feedback in LP10 at 4500V 80mA

In Fig 5.8 the feedback is shown plotted against frequency for a 4500V 80mA beam, where it is evident that the feedback exceeds unity at more than one frequency and the tube will be unstable. In Fig 5.9 the beam current has been reduced to 35mA and the feedback magnitude does not reach a value of unity anywhere in the band.

These simulated results agree with experimental observations in two particular respects, namely, i) the tube shows a tendency for instability at 5.71GHz at higher beam currents, and this was experimentally observed at 5.624GHz, and, ii) stable operation is predicted below 40mA, while experimental observations found this to be 38mA.

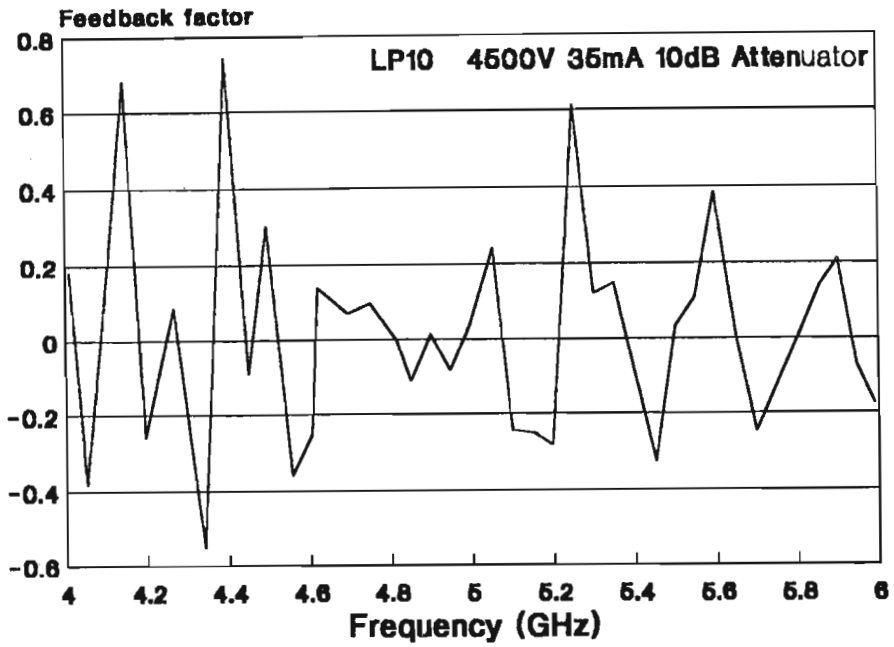

Fig 5.9 : Feedback in LP10 at 4500V 35mA

b) Operation above 4500V

In an attempt to reduce the coupling between beam and circuit (and thus to get the tube stable) the beam voltage was increased progressively above 4500V. A series of measurements was eventually carried out at 5290V 89mA. The performance of the tube was then simulated at the same working point and compared with the measurements. These simulated and experimental results have been shown in Figs 5.4 and 5.5. The simulated and measured gain both show large excursions in the region 4 - 6GHz, and this is due to the considerable amount of feedback reaching the tube input, and it is on the verge of instability. In Fig 5.4 the gain has been simulated at 5100V 89mA, just below the voltage where it was found to be stable, and a large gain excursion can be seen on the left just above 4GHz, predicting potential instability. In Fig 5.10 the feedback is plotted against frequency with the tube operating at 5100V 89mA and the feedback at 4.05GHz slightly exceeds a

value of unity, indicating that the tube would be unstable. Experimental investigations at this value of beam voltage and current indeed showed this to be the case with only a single spectral line being observed on the spectrum analyser at about 4.15GHz, while a very narrow peak in the gain characteristic was also found around 4.44GHz, suggesting a point of possible instability although no oscillation was actually observed near this frequency.

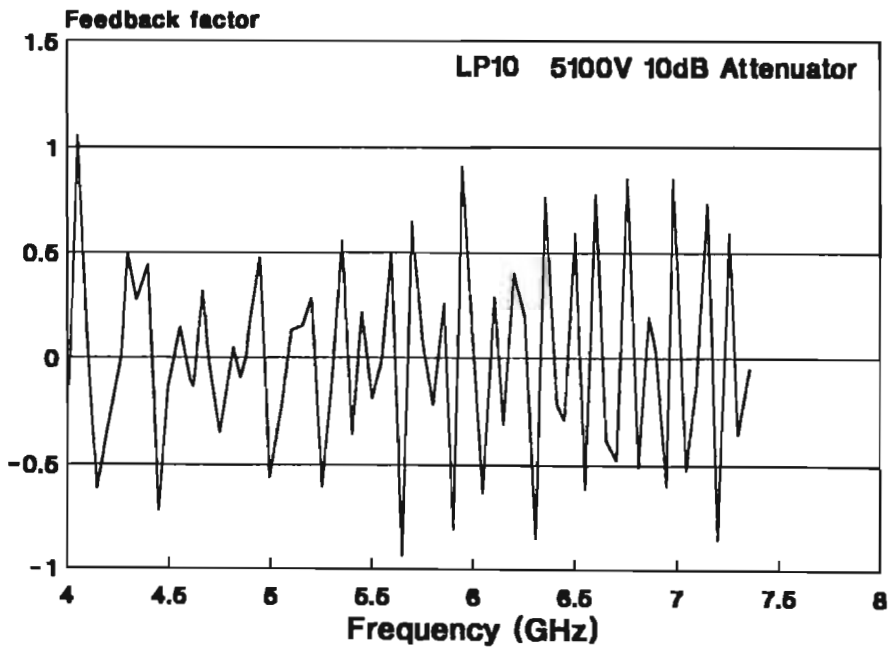

Fig 5.10 : Feedback in LP10 at 5100V 89mA

Shown in Fig 5.11 is the feedback for LP10, biased this time at 5290V 89mA, where it was found to be stable. The feedback just above 4GHz still dominates, although there are quite a few other frequencies in the band where considerable feedback is present. However, their feedback magnitudes have all fallen below unity to about .8 or less, so that the tube is now marginally stable.

The TWT was also operated experimentally at 5478V 89mA and under these conditions was found to be completely stable.

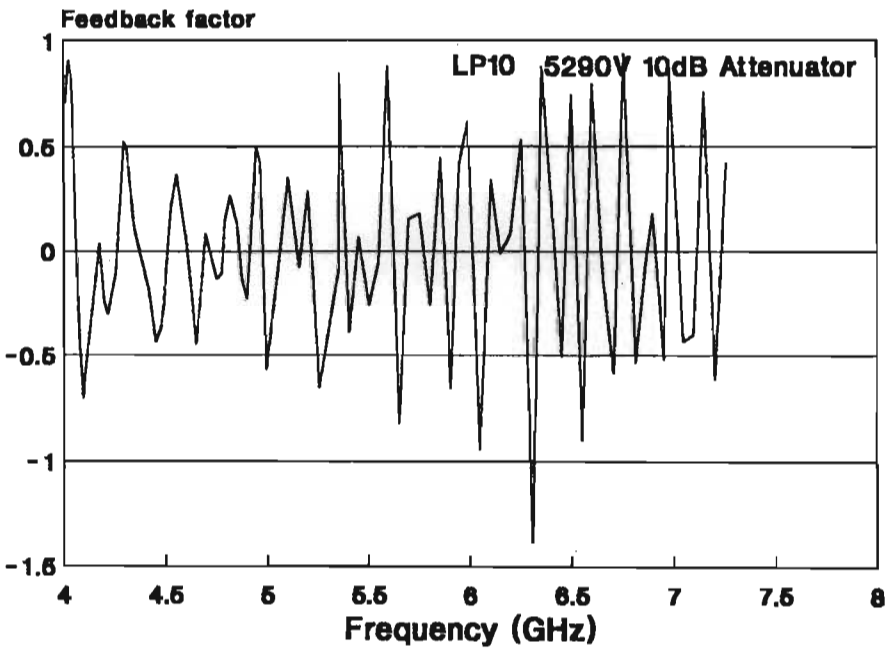

Fig 5.11 : Feedback in LP10 at 5290V 89mA

CHAPTER VI

DISCUSSION AND CONCLUSION

6.1 Introduction

An experimental TWT has been designed, built, and tested. In parallel with this development a simulation facility has been produced which attempts to model the performance of an unstable, imperfect TWT so that certain predictions can be made regarding its performance. An automated test facility was also set up to enable reliable logging of test data.

On most points reasonable correlation exists between theoretical prediction and experimental findings, and these are discussed in this chapter. In order to better verify the model, a commercial TWT of known specification was also brought in and analysed, and these findings are also discussed.

6.2 Phase Velocity

Computation of the phase velocity theoretically has been designed around the approach of Jain and Basu for a dielectrically-loaded helical structure in a metal shell, using circular support rods with a free-space gap between sheath helix and rods. The approach was tested against the the measured data obtained by Belohoubek and good correlation was found, within 4% over a wide frequency range. A variation of this method was also designed in the hope that computer time could be reduced without sacrificing accuracy. For good convergence it was advised [17] that at least n = 100 dielectric tubes would be

required; in practice it was found that n = 200 worked better but obviously it took much longer to reach a value for γ. For the odd calculation it may not have mattered too much, but when it is required to recalculate γ every 5MHz over a very wide band when analysing reflections in the tube, then it becomes a factor. The new method for γ used a sinusoidal variation in dielectric tube thickness, very thin tubes near the helix where the fields are concentrated and where it matters, and much thicker tubes further away from the helix, in the centre of the dielectric region between helix and metal shell. The hope was that, overall, the number of tubes could be reduced, but in the end n = 200 still seemed necessary, so there was no saving in time. The results of the two methods differed somewhat as can be seen in Fig 2.4, and this was independent of how large n was.

While it may be possible to calculate γ and ß with good accuracy, how useful this is will still depend very much on the degree of precision achieved and maintained when assembling a slow-wave structure. How accurately LP10 was put together is hard to quantify, and no measurements were carried out on the cold helix assembly to determine its propagation characteristics.

6.3 Helix and Attenuator Losses

Computation of helix losses in the low-loss input and output sections of the helix has been based on the work of A.S.Gilmour, Jnr, *et al*. Their theory was tested against measured data and reasonable agreement found. In this computation slight adjustments are made by means of a simple polynomial to bring theoretical values more into line with measured data. Helix losses, in any case, are low, amounting only to 1 or 2dB, so the effect of errors here is unlikely to be significant when computing the gain.

Attenuator loss over a frequency band has been modelled by means of a representative third-order polynomial based on the measured S21 characteristics of a molybdenum attenuator. Admittedly, only one attenuator had been used for the model and it was later found that, from attenuator to attenuator, there was quite a wide spread in characteristics. The loss characteristics were found to depend critically on the thickness of the molybdenum layer deposited on the rods, and this process was apparently not very repeatable. Also, the molybdenum layer was fragile in that it did not adhere well to the alumina. Nevertheless, fortuitously perhaps, the attenuator chosen for LP10 turned out to be a rather mediocre one, and this added a bit of realism to the feedback model developed later.

The model used for the electrical characteristics of the attenuator was based on the equations of Gittins described in Chapter 2. It was characterised as a drift space with loss, and as such was frequency-dependent, and exhibited quite a wide range of behaviour. Its behaviour appeared to depend chiefly on frequency, its cold loss, electrical length, and beam velocity. For a while its behaviour was watched narrowly with suspicion, but it seemed to be doing the right things, sometimes providing a little bit of insertion gain, other times a small loss. However, its high frequency performance does not appear to be very good,(see Fig 2.20), and it may have contributed to the rather rapid fall-off in performance of the model at the upper end of the frequency band. In the case of the E3510 tube, with its large gain, the attenuators (there are three) did not appear to play a significant role. However, with LP10 performing like a lead balloon, its attenuator seemed to have an undue influence on its performance.

6.4 Interaction Impedance and Parameter C

The parameter C is obviously significant in determining the decibel gain of the tube, and depends on the interaction impedance. Here the standard Pierce theory had been used, so the interaction impedance was derived from a slightly-modified sheath model. Insufficient attention had been paid to the effects of dielectric-loading and coupling between helix and metal shell. This led to unrealistically high values being computed for interaction impedance, and hence also for C. The tube gain was therefore also too high.

Two issues led to the revision of the way the interaction impedance was to be calculated. Firstly, validating the model for the first time against a tube of known performance confirmed there was a problem, and this problem was soon narrowed down to the interaction impedance. Secondly, in a published paper [49] the interaction impedance was analysed of a structure which was literally identical to that used in LP10. This allowed a direct comparison of the results to be made, when it was found that the values calculated for LP10 were about double the values found in [49]. The procedure in [49] was then adopted and the necessary changes implemented.

6.5 Space-Charge Parameter Q

Computation of Q depends very much on correctly calculating C and ω_q. From a model for the beam profile an "effective" plasma frequency was calculated, and then the space-charge reduction factor F is calculated using a simple procedure. The value for F calculated in this manner is within 10% of that found by Branch and Mihran. Due to the fact that there is ripple in the beam because of magnetic focusing, the plasma frequency may also be modulated by the ripple. The plasma frequency, like C, is

also calculated at several points along the beam and an average value found and hence an average value for Q. Some time after these measures had been implemented investigations into C and the plasma frequency showed that their value varied very little with fluctuations in beam radius.

The value for Q is not large for a 4500V 80mA beam and so space-charge effects are not very serious. Errors in Q are unlikely to cause serious errors in the computation of gain.

6.6 The Electronic Equations

In these days of fast common-place computers there is little justification for certain of the assumptions made in earlier times. One of these assumptions is that higher order terms in C in the electronic equations can be ignored on the grounds that C is always small. C may not always be negligible. It has been shown earlier that taking these higher order terms into account does make a noticeable difference in gain computations, so for the sake of completeness and improved accuracy these higher order effects have been taken into account.

6.7 Launching Losses

Launching loss, in particular that of the gaining slow wave, is an integral part of the gain calculation for a TWT. Equations have been developed for the calculation of the launching losses of the three space-charge waves and results presented. While it is true that the other two space-charge waves make a negligible contribution to the growth of the signal in a TWT, nevertheless these waves are included in the gain calculations and in the feedback model, more for reasons of completeness and correctness than for anything else. To exclude them would probably

make no more than 0.3dB difference to the calculated gain. Inspection of the plots for launching loss reveals that the values are in the vicinity of the expected -9.5dB for b = 0. The launching loss also plays an important role in the feedback model which seems to work quite well.

6.8 Reflections in the TWT

Reflection coefficients for the input and output ports have been based on calculation, using a model for the helix characteristic impedance in a dielectrically-loaded metal shell, modified by stray inductance and port susceptance. The calculated values of return loss are reasonably close to measured S11 and S22 values. Reflection coefficients for the attenuator were initially taken directly from time domain measurements done on a cold helix sub-assembly, but these results do vary from attenuator to attenuator, the best being about 0.04 and the worst 0.1. Furthermore, this value of the voltage reflection coefficient is a generalised value, not specific to a particular frequency but drawn from data derived over a wide frequency band. It was felt that it would be better, if possible, to characterise the interface between helix and attenuator as a function of frequency.

It is perhaps to be regretted that the design of matching transformers for the input and output ports was never undertaken. Simulations have shown that the mismatch at the input and output ports is the dominant cause of internal feedback and the resulting instability.

6.9 An Internal Feedback Model

It became evident early on that the TWT's were prone to instability. For this reason it was decided to design a simple model for this unstable behaviour which was

subsequently tested in a real situation. The model estimates the magnitudes of an in-phase and quadrature-phase feedback component as they recombine with the input signal. Using the model the beam current at which the tube would become unstable can be quite accurately predicted. Inspection of the feedback plots also gives information on likely frequencies of instabilities, and which frequencies are more likely to occur than others. Again, in certain situations, where instabilities were experimentally observed these agreed quite closely with what was predicted.

Operating the tube at beam voltages significantly higher than the optimum value of 4500V could also be modelled quite successfully in terms unstable behaviour due to mismatch.

6.10 Measured and Simulated Gain

Calculation of the tube gain is now based on improved values interaction impedance. Inspecting Figs 5.3 and 5.4 a reasonable correspondence can be seen between measured and calculated gains for LP10, at least over moderate bandwidths. The effect of internal reflections is evident in both measured and calculated values. Certain differences become evident also when inspecting these results. In Fig 5.3, the model suggests a steady decline in performance beyond as low as 5GHz, whereas the measured data indicates that there was some activity to beyond 8GHz. In Fig 5.4 the trends are reversed : the model suggests modest improvement in the performance up to beyond 6.5GHz before declining, whereas the measured data shows a steady decline from about 5.5GHz. These differences are perhaps not very pronounced and could be due to a number of factors. For example, in Fig 5.4 the tube is being operated at an unusually high voltage in order to force it to be stable. Its gain has already been

reduced. It is being operated at a point where the velocity parameter b has taken on a rather high value of +1.9. If one consults Pierce's Fig 8.4 one gets a better idea of what happens when b approaches +1.9, especially when there is very little space-charge (QC=.03) and the loss is low(d=.025) as in the model for LP10. The performance becomes a little unpredictable, especially over a band of frequencies, since to some extent the value of b will be affected because of its dependence on a frequency-dependent C.

The model was also tested on the E3510 wide band TWT, and the results are to be seen in Figs 5.6 and 5.7. The model gives values for gain (typical small-signal gain) about 15dB above the minimum small-signal specification. The small-signal gain is not quoted in the specification, so it is assumed to be about 5dB above the minimum saturated value. The model predicts the gain quite realistically, and only falls down in estimating the usable bandwidth, somewhat less than the 6.7 - 17GHz stated in the specification.

Generally the model appears to give reasonable estimates of gain under various conditions of bias and frequency.

CHAPTER VII

DESIGN OF A PULSE MODULATOR FOR TWT TESTING

7.1 Introduction

Certain considerations make pulsed operation of an unevaluated experimental TWT an attractive if not essential option, and some of these considerations are given below :

7.1.1 Low Stress

An experimental TWT, because of its perhaps unpredictable and unknown behaviour, needs an environment within which it can be safely evaluated without any risk of damage. Because of the risk of damage to delicate parts of the tube, such as the helix, the tube is best operated in pulse mode at a low duty cycle of a few percent so that the average power dissipated in the tube is kept within safe limits and the temperature rise restricted. Reduced temperature gradients across, for example, metal-ceramic joints would keep stresses low.

7.1.2 Stable Operation

Restricting the temperature rise in the tube limits drift in tube parameters during measurement, making for more accurate logging of data.

7.1.3 Adjustments and Activation

Certain aspects of the process of activating the tube require careful control over the conditions of bias, such as in forming of the cathode, outgassing of the tube, and

during optimisation of the magnetic beam focusing for the best beam transmission through to the collector. Combinations of continuous and pulsed bias may best serve this purpose.

Once reliable and predictable operation is achieved and the final adjustments to the PPM focusing system have been satisfactorily performed the tube may then be safely operated continuously.

7.2 Methods of Pulsing the TWT

Two means of pulsing the experimental TWT were defined. The first involves pulsing the cathode negative with respect to the anode which is at ground potential. The second relates to applying the required conditions of bias to the modulating electrode to either draw the full beam current, or to cut it off. These two methods will now be discussed with their respective advantages and disadvantages.

7.2.1 Pulsing the Cathode Negative

Considering that RF measurements would form the most significant part of the evaluation of the experimental TWT, and that for convenience the helix and anode should be operated at or near ground potential, the most satisfactory configuration for biasing the tube would require the cathode to be pulsed negative. The voltage applied to the cathode would be that voltage required to fully form the beam, and the voltage source would also have to supply the full cathode current. Between pulses the cathode-anode potential would be reduced to some arbitrarily low value, preferably zero, in order to force the beam current to zero.

The heater is normally operated at a potential very close to the negative cathode potential, as would be the modulating and focus electrodes. Mains-operated equipment such as the heater power supply, bias supply for the modulator electrode and parts of the monitoring system would need to be operated near to cathode potential, and primary power would have to be supplied via mains isolation transformers. Pulsing the cathode negative in such a case would also require that all such equipment and circuitry at cathode potential be driven by the pulse. In particular this would mean that the capacitance between the primary and secondary windings of the mains isolation transformer would have to be charged rapidly to cathode potential at every pulse, and this would require that the pulse modulator be able to handle such capacitive surges repeatedly without undue stress. Discharging of this capacitance would most likely be through the experimental tube.

7.2.2 Pulsing the Modulating Electrode

This configuration requires the cathode to be held continuously at the correct negative potential with respect to the anode, which is at ground potential, while the modulator electrode is pulsed. The positive modulator pulse which turns on the TWT is referenced to the cathode, and is nominally 25% in magnitude of the cathode-anode voltage.

The modulator bias supply is configured to provide zero bias on the modulating electrode when the tube is cut off, and the positive pulse is superimposed to turn on the TWT. Since the modulating electrode effectively screens the cathode from the anode, at zero bias on the electrode the accelerating electric field at the cathode surface is reduced to a low value and little current flows. What current does flow is only a few percent of the full beam

current and because the gun is badly focussed under these conditions most of this current is intercepted by the anode.

When the electron gun is pulsed on by the modulating electrode the electric field at the cathode surface rises to its operating value and the beam is formed. Since the modulating electrode behaves as a lens the positive bias applied affects the focusing of the beam. The magnitude of the pulse is therefore adjusted to optimally focus the beam through the anode aperture into the drift space beyond.

Under conditions of near-optimum focusing no measurable current is intercepted by the modulating electrode and it is seen by the pulse modulator circuit as a small capacitance of only a few picofarad. Considering that the normal bias applied does not exceed about 1200V the modulating electrode would be quite easy to drive directly from a solid-state circuit.

During the time the pulse rises from zero to its maximum value the modulating electrode is at some intermediate voltage and the electron gun is defocused. Quite large currents flow to the anode because of this, and the slope impedance of the anode-cathode characteristic can become negative. Due to the presence of stray inductance and capacitance in the cathode circuit instabilities can occur. It is therefore important that the region of instability should be traversed as quickly as possible, and pulse rise and fall times need therefore to be kept to a minimum. The sum of the rise and fall times should together be limited to a small fraction of the pulse width so that errors are minimised.

The modulating electrode has a large aperture permitting all of the beem current to pass through it under normal conditions. A condition to be avoided, however, is that where the anode-cathode voltage is reduced to a low value while the modulating voltage remains large. This especially applies when the TWT is operated under d.c. conditions. Here electrons would be accelerated towards the modulating electrode rather than the anode. The average power applied by the modulating circuit should be sufficiently low to avoid damage through overheating to the modulating electrode. This is achieved by maintaining the circuit impedance high enough to limit the current.

7.2.3 Design of the Grid Pulse Modulator

The circuit diagram of the grid pulse modulator is shown in Fig 7.1. The negative terminal of the pulse modulator is connected to the cathode of the TWT which is held at approximately at -4500V and pulses of up to +1400V are applied to the modulating electrode. The regulated d.c. power for operating the modulator is obtained externally from a high voltage Kepco power supply, and the output voltage of the Kepco is adjusted to give the desired pulse magnitude. The Kepco is naturally also referenced to the cathode of the TWT, and a.c. mains power is obtained for it via an isolation transformer.

Pulses for driving the modulator are obtained from the reference pulse generator and these are delivered over an optical link as light pulses to an HFBR2524 optical receiver. The optical receiver puts out 5V logic level pulses, buffered by a high-current CMOS buffer (IC2), and these pulses are translated into current pulses of 16mA nominal magnitude in the collector of Q2. A power supply including a 5V monolithic regulator and associated components provides a regulated 5V for the optical receiver and logic circuits which drive Q1 and Q2.

Transistors Q1 and Q2 are connected in cascode, Q2 being a low-power switching transistor and Q1 being a high-voltage television deflection power transistor capable of withstanding up to 2200V. The current pulses generated by the non-saturated switching action of Q1,R1,R2, and R3 pass through the emitter of Q2 into its collector circuit. In the collector circuit of Q1 is a 40W 88kΩ pull-up resistor, and the current pulses flowing through it generate the output voltage pulses of the required magnitude. The diodes D2 and D3 prevent Q2 from fully saturating and this reduces delays in the transistor.

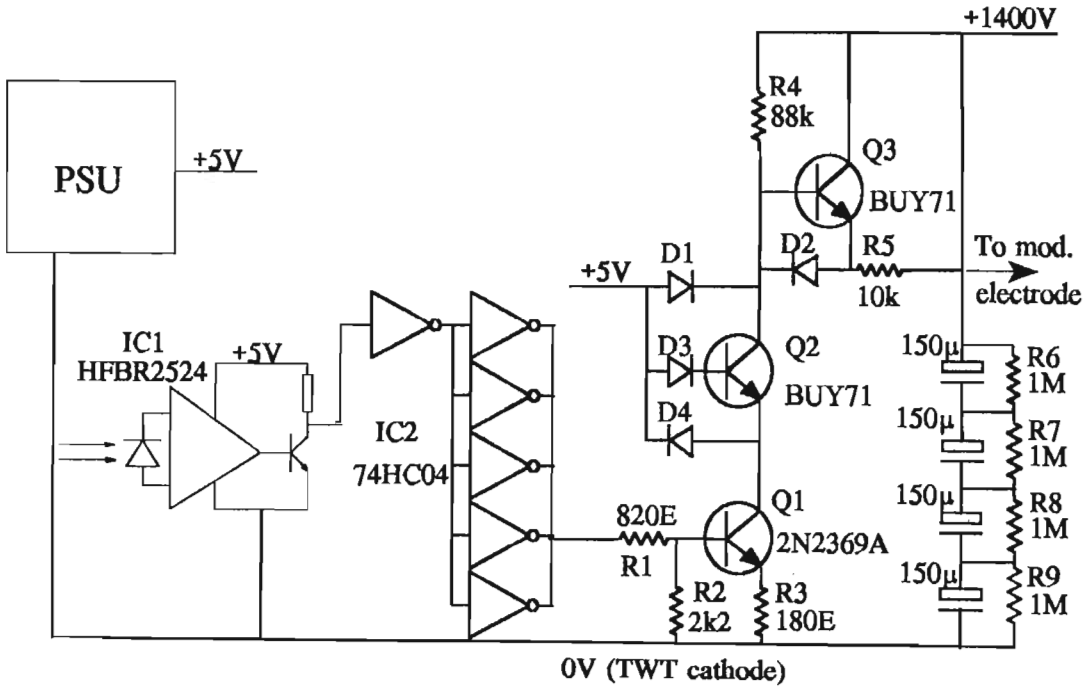

Fig 7.1 : TWT grid modulator circuit

At the output of Q2 is an emitter-follower comprising another high-voltage transistor Q3 in association with R5 and D2. The main reason for this output circuit is to reduce the output resistance of the modulator to a value

not much greater than 10kΩ so that the output pulse shape and magnitude are less affected by extraneous influences. Furthermore, earlier designs of the electron gun had had the weakness that deposits of barium oxide could build up on the ceramic support rods between the modulating electrode and cathode, creating a conducting path which made it more difficult to drive the electrode with large positive pulses. In later electron gun designs the ceramic rods were screened to prevent these deposits and the problem was solved.

The normal mode of operation requires that Q1 and Q2 be in conduction between pulses and the output voltage at the collector of Q3 is therefore low (approximately +4V with respect to the cathode). During a pulse Q1 and Q2 are cut off and the voltage rises at the emitter of Q3. The rate of rise is determined by the rate at which the 88kΩ load resistor R4 charges the capacitance seen in this part of the circuit. This capacitance is chiefly comprised of the collector capacitance of Q2 and Q3 and the junction capacitance of D1, totalling about 300pF. Other circuit capacitances due to the wiring and the modulator electrode add up to only a few picofarad. The response at the output is nominally about 15μs, and because the circuit operates in a non-saturated mode, this time constant is the same during both the rise and fall of the pulse. Because the periods of rise and fall of the pulse represent periods of possible instability in the TWT, these times should not be made any longer. Preferably, the pulse width and period should also be long compared with these transition times if accurate logging of pulsed currents in the TWT is desired.

7.3 Pulse Modulator Requirements

In view of the different forms of d.c. and pulse bias that could be required during the development of a TWT , it was

decided that the pulse modulator should, in principle, be as flexible and versatile as possible. For example, the development of the dispenser cathode in a test diode would require low positive voltages at higher currents, while testing the electron gun would require much higher voltages of negative polarity at lower current negative polarity. The test diode would also not have a control electrode, whereas the electron gun would. It was decided therefore, in principle, to implement both methods of pulsing the TWT. Characteristics considered to be desirable in a pulse modulator are described below.

7.3.1 Positive and Negative Polarity

For maximum versatility, output pulses of either positive or negative polarity should be available from the pulse modulator without any essential differences in performance. Changing the polarity should be as straightforward as possible. Both polarities were considered necessary because it was felt that the pulse modulator configuration should be versatile enough to test a number of different vacuum tube devices as the need arose, and also to allow flexibility in the choosing the configuration for modulating the device under test.

7.3.2 Adjustable Output Amplitude

The output amplitude of the pulses should be continuously adjustable between zero and some maximum value by means of a simple linear control. The maximum value of the output pulse should be preferably only somewhat lower than the d.c. input to the modulator, perhaps 90% or greater, in order to minimise the stress on the modulator. The stress would be proportional to the product of load current through the modulator and voltage drop across it. This would require the rectifier input to the modulator to be adjusted by means of, for example, a variac or electronic

control to a value about 10% greater than the desired output pulse amplitude. In view of the 4.5kV 80mA required for the experimental TWT, it was decided that the range in output from the modulator should be from zero to 5000V, either positive or negative, with currents not exceeding 200mA.

7.3.3 Regulation of Pulse Amplitude

The output pulses should be regulated in amplitude so that the pulse modulator would have a reasonably low output impedance, much lower than the slope impedance of the anticipated load which would be typically that of an electron gun cathode.

A typical value for the slope impedance of an electron gun with a perveance of 265μPervs could be obtained by differentiating its IV characteristic :

$$\frac{dV_k}{dI_k} = \frac{2}{3PV^{1/2}} = Z_k$$

At V_k = 4500V where I_k = 80mA this would be about 37.5kΩ. A suitable output impedance for the modulator would be no greater than a few hundred ohms.

7.3.4 Line Regulation

The modulator should have the ability to filter the input from the rectifier such that very little rectifier ripple or variation in rectifier voltage should be impressed on the output pulse. This is desirable because of the ease with which the output of a TWT can be phase-modulated by variations in cathode voltage. For the same reason the output level of the pulse should be kept stable over its

$$\frac{d\varphi}{dV_k} = -\frac{\varphi}{3V_k}$$

where ϕ is the total phase shift undergone by a wave in the interaction region of the TWT. The phase shift is proportional to the length of the TWT, and therefore also to its decibel gain. After manipulating the gain formula for a TWT :

$$Phase\ \varphi = \frac{2\pi(G + A)}{BC}\ .\ (rads)$$

where G is the decibel gain of the tube, B is the gaining wave parameter, A is the overall attenuation in the tube due to launching loss and sever loss, and C is the Pierce gain parameter. Inserting typical values of G = 40dB, A = 13dB, B = 47.3, and C = .05 :

$$\phi = 140.8 \text{ radians}$$

and the pushing factor would be :

$$\frac{d\varphi}{dV_k} = -.0104\ rads/volt$$

This is an approximate value which serves to indicate the order of magnitude of the phase pushing factor. The phase modulation sidebands would be approximately at a level of 20log(.0104) = - 39.6dB for 1 V(rms) interference impressed on the cathode. It appears reasonable to limit the interference at the cathode to 1 V(rms), although this choice is arbitrary. There are no clear logical guidelines at this stage to setting the limits to incidental phase modulation because the experimental tube does not have a clearly defined application and therefore its

specification is incomplete. AM sidebands would appear also to be very low for a permissible level of 1 V(rms) on the cathode.

7.3.5 Pulse Width and Period

The output of the modulator should be independently adjustable in pulse width and duty cycle as an added facility for TWT testing, since the behaviour of TWT's may vary with applied pulse width. Ion oscillations could take place in the tube if the pulse is too long, whereas short pulses might avoid this. Thermal effects in longer pulses, or higher duty cycles, may cause drift in parameter values.

7.3.6 Solid-state Design

If possible, the unit should be entirely solid-state. While a suitable vacuum tube, such as a transmitting tetrode, could have been considered for the pass element of the pulse modulator, problems would arise in obtaining output pulses of either polarity , further complicated by provision having to be made for floating screen grid and heater power supplies. Nevertheless, the vacuum tube is very forgiving, being able at high voltages to withstand surges and overloads in a manner that semiconductor devices could not.

7.4 Concept for a Pulse Modulator

The configuration adopted for the modulator is shown in the block diagram in Fig.7.2. It is based on the standard configuration for a voltage regulator comprising a series pass element, an attenuator, a feedback amplifier and a voltage reference, with the exception that the normally fixed voltage reference is replaced by a reference pulse

of adjustable magnitude, pulse width, and duty cycle. The output of the regulator is then a magnified replica of the reference input pulse.

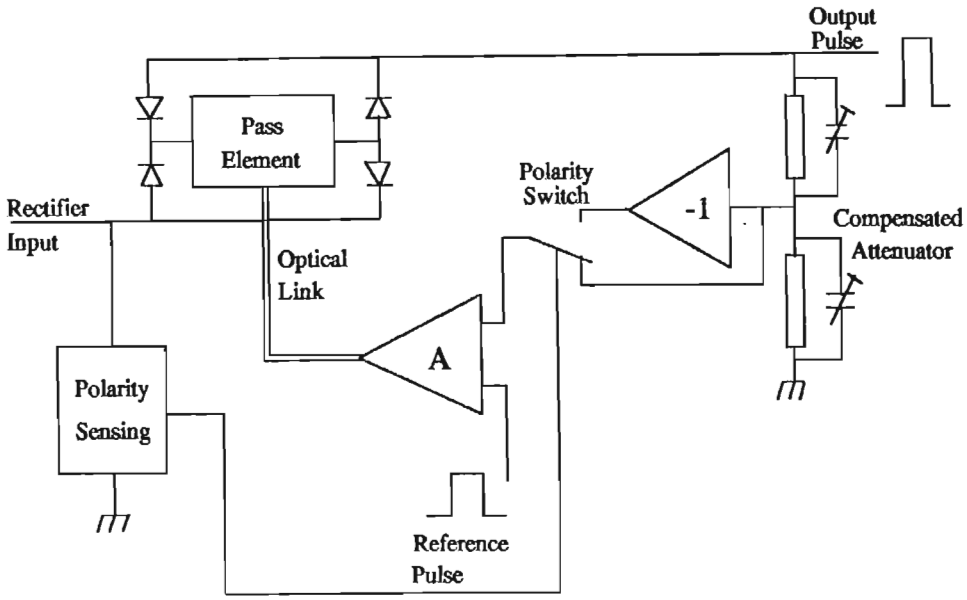

Fig 7.2 : Pulse modulator concept

A novel feature of this configuration is that the pass element is placed within a rectifier bridge, enabling it to handle positive and negative rectifier inputs, while additional circuitry senses the polarity of the applied rectifier input voltage and automatically corrects the polarity of the pulse sample obtained from the attenuator, or voltage divider. In this manner adjustable, regulated output pulses are obtained having the same polarity as the rectifier input. In the absence of an output pulse the full rectifier voltage will appear across the pass element. Because a single solid-state pass element could not handle the full rectifier voltage on its own, which can exceed 6000V, six elements are connected in series with arrangements being made to equally share the very large voltages. As a consequence, six independent regulating loops are required, each with its own unique voltage reference. The configuration is shown in Fig.7.3.

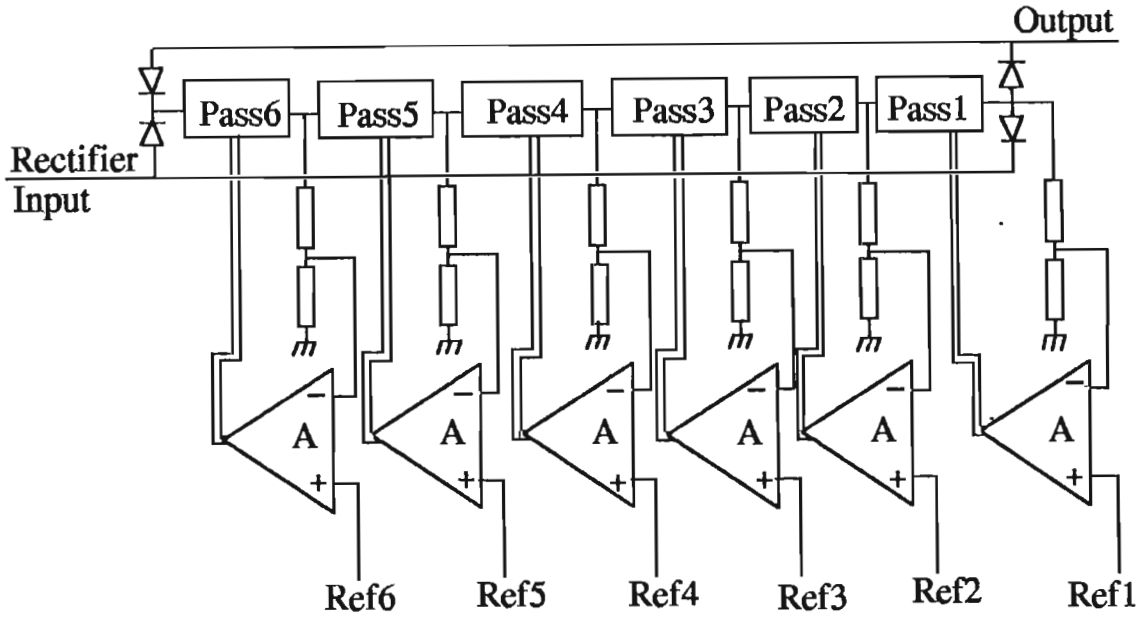

Fig 7.3 : Multiple regulating loops for voltage-sharing

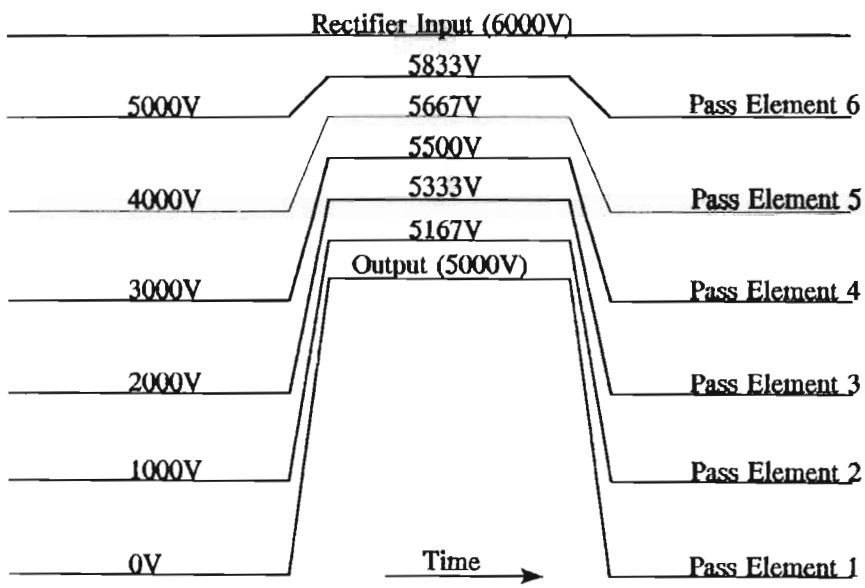

Fig 7.4 : Waveforms for a 5000V output pulse

In Fig.7.4 some waveforms are shown for an output pulse of 5000V and how the voltage is shared among the pass elements. In the absence of a pulse at the output, the rectifier voltage is shared so that 1000V appears across each pass element. During a pulse the volt drop across each element falls to 167V.

7.5 Specification for the Pulse Modulator

The following specification for the pulse modulator was drawn up, although somewhat arbitrarily since at the stage the pulse modulator was designed and developed only one application was in view :

Maximum regulated output pulse	:	5000V
Maximum peak output current	:	200mA
Maximum rectifier input volts	:	6000V
Range of Pulse Widths (continuously variable)	:	50μs - 1.2ms
Range of repetition rate	:	10Hz - 500Hz
Output impedance	:	< 1000 ohms
Output pulse polarity	:	same as rectifier input
Maximum safe duty cycle	:	10% for pulse widths of 50μs to 300μs

	:	1% for pulse widths of 300μs to 1.2ms
Operating modes	:	d.c. or pulse output of either polarity

7.6 Design and Description of the Pulse Modulator

7.6.1 The Series Pass Elements

The overall pass element comprises six identical elements connected in series with arrangements to at all times equally share the voltage across them. The full load current passes through each element, and the power dissipated in each one can therefore be expected to be approximately the same. Six elements were chosen after a survey of the capabilities of various semiconductor devices. This survey led to the decision to use high voltage bipolar NPN power transistors designed for use in horizontal deflection systems for television.

Power FETs were initially rejected as possible candidates mainly on the grounds of cost and availability, and also because of their poorer high voltage performance (maximum voltage across these devices appears to be limited to 1000V). At a later stage they were again to be considered because of certain very real advantages over bipolar transistors, in particular because they are not subject to that very destructive phenomenon, particularly prevalent in high-voltage bipolars, known as second breakdown.

Second breakdown occurs in all bipolar transistors where they are subjected simultaneously to higher voltages and excessive collector currents. At lower voltages and higher

collector currents operation is limited rather by thermal considerations. In view of the limitations of second breakdown and thermal effects the safe operation of bipolar power transistors is specified in terms of Safe Operating Area (SOA) curves, provided by the manufacturer of the device. An example of such SOA curves is shown in Fig.7.5, being in this case for the BU208A/BU209A television deflection power transistor.

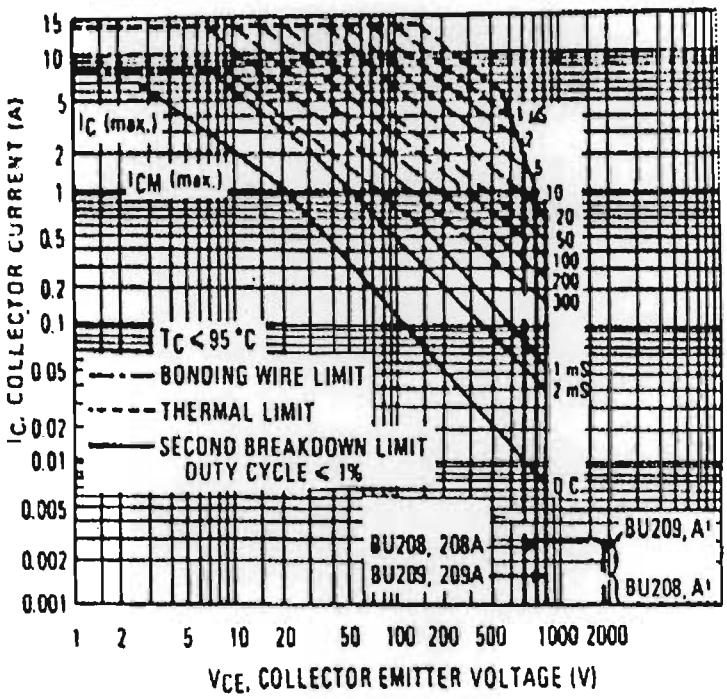

Fig 7.5 : Safe Operating Area curves for the BU209A deflection transistor

As may be seen from these curves distinction is made between d.c and pulse operation, the device being able to withstand much higher stresses under pulsed conditions. The shorter the duration of the pulse the higher the permissible stress. The region to the left (lower voltages) of the pulse curves relates to thermal dissipation limits in the device, whereas that region to the right (higher voltages) is limited by second

breakdown. Operation must be kept at all times in the safe area below these curves, and the duty cycle stated with the SOA curves should be observed.

The transistor eventually chosen for the role of the series pass element was the BUY71, a television deflection transistor. Regrettably, very little data was found upon which to base the design, but what was found was sufficient to decide to use it. Its main specifications are listed below :

Sustaining voltage, V_{CES}	:	2200V
Max collector current, I_{CM}	:	5A
Reverse emitter-base voltage, V_{EB}	:	5V
D.C. Current gain, H_{FE}	:	13 (typ) at I_C = 100mA V_{CE} = 10V
Collector dissipation, P_D	:	20W
Risetime, t_r	:	800ns
Falltime, t_f	:	1300ns

7.6.2 High Voltage Module

The schematic of the High Voltage Module is shown in Fig.7.6. The BUY71 transistor is driven in grounded-base mode to maximise its resistance to second breakdown, and it is connected in cascode with Q3, a BD139 medium power transistor. Driving the BUY71 in grounded-base means that its current gain is less than unity, and its emitter current will reach a maximum value of greater than 200mA, and this current must be provided by the BD139.

Since the high voltage module will be biased at a large voltage with respect to ground (up to 6kV) some interface has to be found to drive or control the module across this very large potential difference. This potential difference is furthermore not constant but slews rapidly between two values during the pulse transition. The interface between the drive circuit and the module should preferably have the following characteristics :

i) a large current transfer ratio in the forward direction

ii) nearly zero reverse current transfer ratio, especially under transient conditions, requiring the capacitance across the interface and reverse conductance to be practically zero

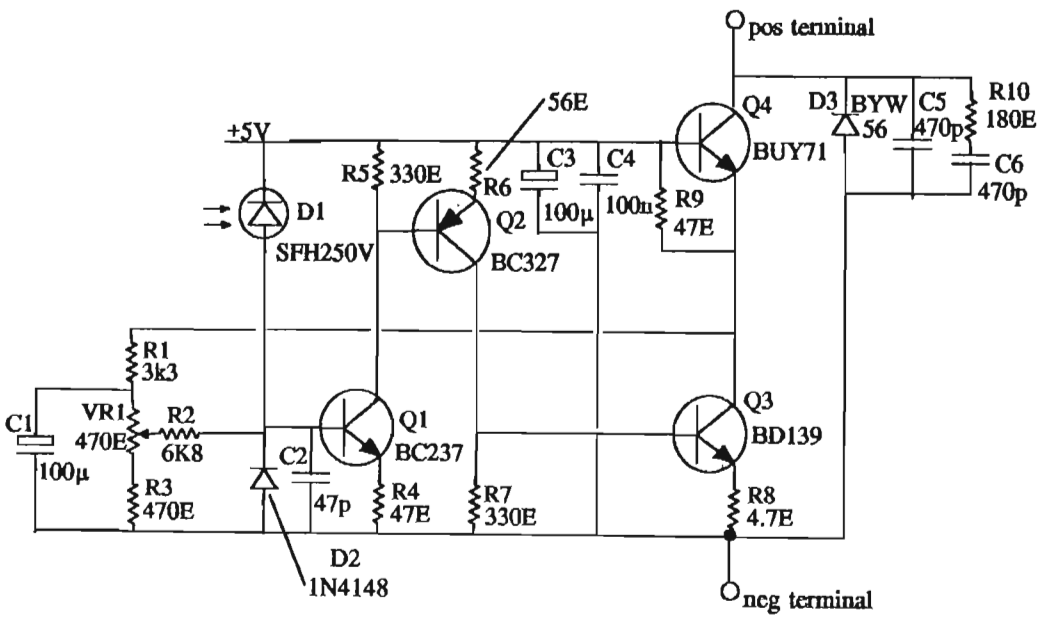

Fig 7.6 : Basic schematic of the High Voltage Module

iii) a very fast response with practically zero delay through the interface

iv) the ability to sustain d.c. control of the loop, permitting the power supply to be used not only in pulse mode but also as a d.c. regulator if required

v) and the ability to stand off very large voltages indefinitely without measurable leakage or risk of breakdown.

These requirements were met by using an optical link comprising a SF451 red transmitter, a 40mm length of plastic fibre optic cable, and an SF250V PIN diode detector. Being a diode-diode link the current transfer ratio is unfortunately poor at .13%, but the response is fast with current rise times of nominally 120ns and fall times of 50ns. Capacitive coupling is very low at approximately .01pF, and voltages of up to 40kV can be withstood.

In view of the poor current transfer ratio the optical detector diode is followed by a fast direct-coupled amplifier, comprising Q1, Q2, and Q3, which amplifies the opto detector output current (a few tens of microamperes) to output currents of greater than 200mA. In order to achieve this the current gain of the amplifier has to be at least 4800, and the overall gain is determined by the values of the emitter-degeneration resistors R4, R6, and R8. D.c. biasing of the amplifier is accomplished by applying an input bias to Q1 via R1-R3 and VR1, and the correct point is obtained by adjusting VR1 so that Q1,Q2, and Q3 are in conduction, but Q4 remains cut off. Under these conditions the voltage drop across R9 should be approximately 400mV, insufficient to turn on the BUY71. The bias network is supplied from the junction of the emitter of Q4 and R9, and the d.c. negative feedback in

the loop makes the setting up of the bias fairly simple, while C1 removes any a.c. negative feedback which would otherwise make the gain of the amplifier too low. Capacitor C2 reduces the response of the circuit to where there is no instability and its value is chosen small enough for an adequately fast response. Capacitors C3 and C4 provide the necessary decoupling for the +5V supply required by the amplifier, and also supply the current surges (up to 20mA) required by the base of the BUY71 during pulses.

The gain of the HV module is large due to its high transconductance and the very high collector impedance of Q4. Across the module is a network comprising C5, C6, and R10 which cause the collector impedance to fall as the frequency increases, reducing the gain and the risk of instability.

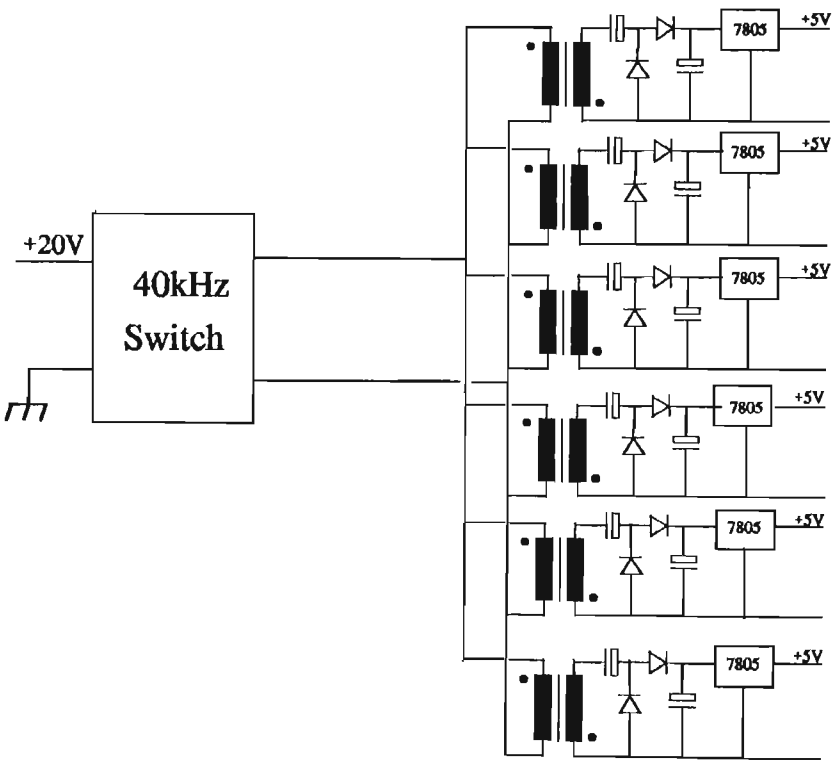

Fig 7.7 : Basic switchmode converter

Across the module is also connected a fast avalanche diode D3 which breaks down in the vicinity of 1350V. This diode protects the module (more specifically Q4) against large voltage transients which may occur if there are arcs at the output of the modulator.

The diode can absorb non-repetitive transients of up to 1kW for 20μs, or 100W for 1ms, without damage and its recovery time is typically less than 2.5μs which is short compared with the duration of any expected transients.

The direct-coupled amplifier requires d.c. power (+5V), and this is provided by a d.c.-d.c. switchmode converter. The basic diagram is shown in Fig 7.7. It has six separate ferrite switching transformers, each dedicated to supplying power to a particular high-voltage module. Switching is at nominally 40kHz. The primary windings are all connected in parallel, each secondary separately driving a voltage-doubling rectifier delivering approximately 8V followed by a 5V monolithic regulator. The primary windings of the switch-mode transformers are at ground potential, while the secondaries are at various high potentials, and these windings are wound on split polycarbonate bobbins with careful attention having been paid to obtaining the best isolation and minimum capacitive coupling between primary and secondary windings.

7.6.3 High Voltage Rectifier

The six pass elements are connected in series and are placed within a high voltage rectifier bridge. The task of the rectifier bridge is solely to ensure that the pass elements are always correctly polarised whatever the polarity of the rectifier voltage that is applied to the input of the pulser. Speed of switching is not of any concern for the rectifier bridge since it does not switch

a.c. signals but performs a simple connecting function. The diode bridge is comprised of a total of 20 1A rectifier diodes with a rated PIV of 1500V each.

7.6.4 Voltage Dividers and Loop Amplifiers

Seven identical frequency-compensated voltage dividers are used in the feedback paths. Shown in Fig 7.8 is a block diagram of one such voltage divider and loop amplifier. All the dividers have the same voltage division ratio of nominally 480. The attenuators are frequency compensated by fitting adjustable capacitors in parallel with the upper and lower sections of the attenuators, and these capacitors are of sufficient size so as to swamp the natural stray capacitances of the resistor string. Adjustments to these trimmer capacitors are also intended to compensate for unavoidable signal delays around the loops, without which the loop might be unstable or display unacceptable levels of overshoot.

Outputs from each resistive divider, ranging from zero to 10V, are buffered by fast non-inverting voltage followers IC4(LM310) and by unity-gain inverting amplifier IC3(LF357). These devices were chosen for their speed, so that delay around the loop would be minimised. Both inverted and non-inverted outputs are brought out and delivered to a CMOS switch (IC2) which selects one of the signal outputs to be passed to the loop amplifier. The switch selection operates in such a manner that signal outputs from the CMOS switch are always positive.

The output from the switch (IC2)) is applied to the input of a differential amplifier in which the signal sample obtained from the feedback loop is compared with a reference signal. The differential amplifier drives an outboard transistor (Q1) in such a manner that the collector current is linearly proportional to the error

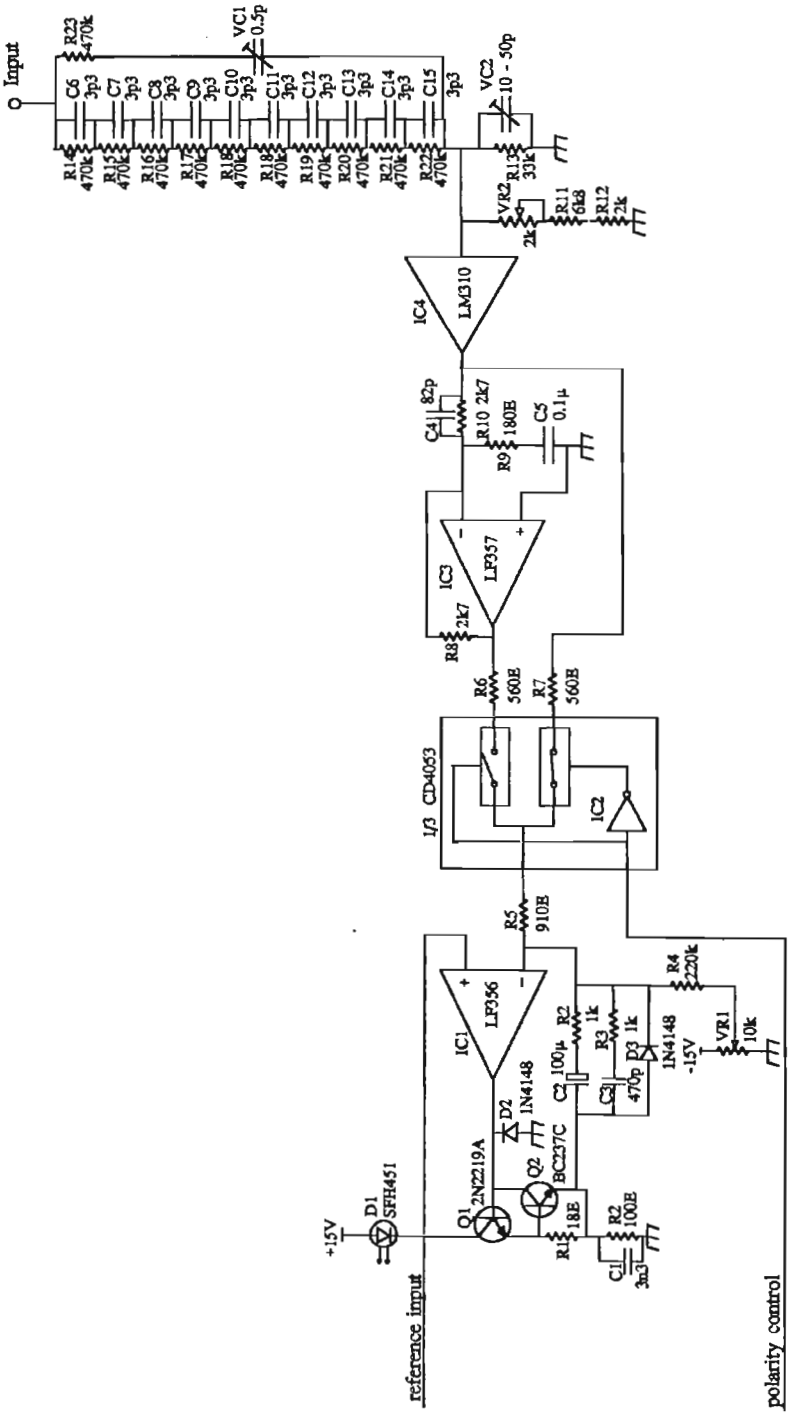

Fig 7.8 : Basic schematic of voltage divider and loop amplifier

between the reference and feedback signals, and the collector current drives the SF451 optical transmitter LED. The resistor/capacitor network R2-R3, C2-C3 sets up the negative feedback path for the amplifier and determines the gain of the circuit.

Propagation delays through the amplifier are undesirable but unavoidable, causing overshoot or instability in the overall loop, and effort has been made therefore to minimise such delays. A fast op amp (LF356) was chosen for the differential amplifier IC1, and a fast transistor for Q1 in the output circuit. A small capacitor C1 across the emitter resistor R2 of the output stage provides some speed-up to compensate for the propagation delays through the loop amplifier.

A current limiting circuit (Q2 and R1) has been included in the output to ensure that peak currents are kept to a safe maximum of 40mA in the optical transmitter LED, D1. Surges in current normally occur at the leading edge of a pulse as the loop is stabilising.

7.6.5 Pulse Generator and Reference Circuits

The pulse generator produces the reference pulse train with specified pulse width and pulse rate. The output pulse train of the Pulse Modulator is intended to be a magnified replica of the reference pulse train. Control of the pulse width and pulse rate is from the front panel, and the pulse width is continuously variable between 50μs and 1.2ms, while the frequency may be varied from 10Hz to 500Hz. A mode switch on the front panel permits the pulse generator to used in different ways, in free-running mode, in manual mode producing a single pulse each time the MANUAL push-button switch is depressed, and in 50Hz mode in which the pulse train is slaved to the 50Hz mains. In each of these modes the pulse width may be independently

selected.The schematic of these circuits may be seen in Fig 7.9.The reference pulse generator comprises two CMOS retriggerable monostable multivibrators (CD4047). The first, IC1, is configured either in free-running (or astable) mode, where the frequency is set by VR1, R1, and C1, or in single-shot (monostable) mode producing a single pulse each time the MANUAL switch is operated. The second, IC2, operates as a monostable multivibrator producing pulses of width determined by VR2, R5, R6, C3, and C4, and it is triggered by outputs from IC1. In the 50Hz LINE mode IC1 is inhibited and a 50Hz square wave is applied to the +TRIGGER input of IC2 instead. The 50Hz square wave is derived via Schmitt trigger NAND gates, IC3a and IC3b, the sinusoidal input being taken from a sample from the secondary winding of the mains power supply transformer.

The output from IC2 is reduced in magnitude and buffered by fast voltage follower, IC4, and a variable reference signal between 0 and 8V is obtained from VR4. The function of VR4 (which is on the front panel) is to set the output level of the Pulse Modulator by varying the reference level. In this way continuous control over the output pulse height is obtained between zero and 5000V. Another mode switch is included at this point of the circuit, providing selection at the front panel of reference waveforms from either the internal pulse generator, or from an external source.

The reference pulse at the output of IC4 has very short rise and fall times, of the order of 10ns, and such fast transitions would cause the modulator output pulse to overshoot. For this reason the rise and fall times are increased by means of R22 and C10 to approximately 5μs.

Six different reference signals are required by the six regulating loops, and these are generated in the circuit comprising the voltage-followers IC6 and IC7 and the

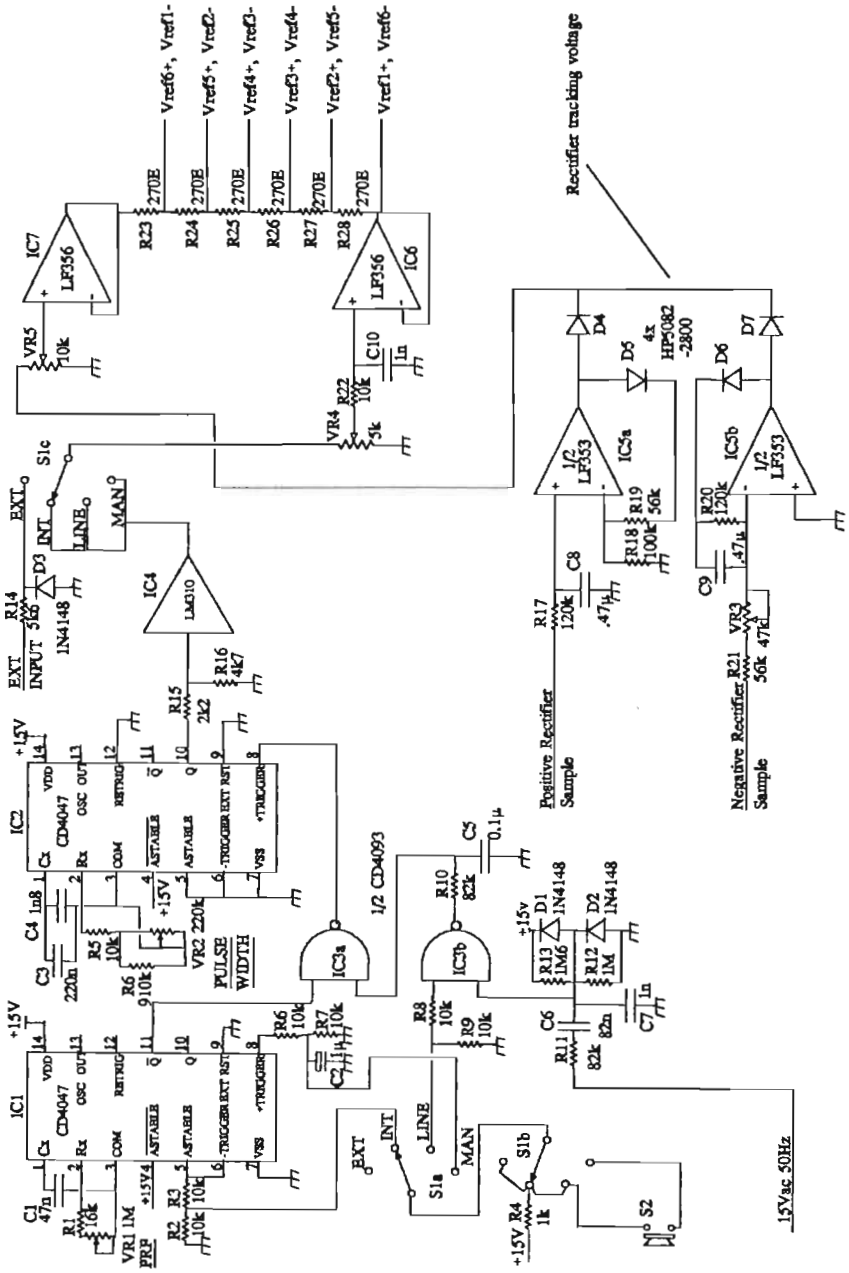

Fig 7.9 : Basic schematic of pulse generator and reference circuits

dividing network R23 - R28. The reference pulse is applied to the network from IC6, and the d.c. bias applied via IC7 and VR5. The reference pulse is combined with the d.c. bias in differing proportions, and the references are picked off at various points along the resistor network. The six combinations of reference pulse, Vref, and the d.c. bias, Vrect, are depicted in Fig 7.10.

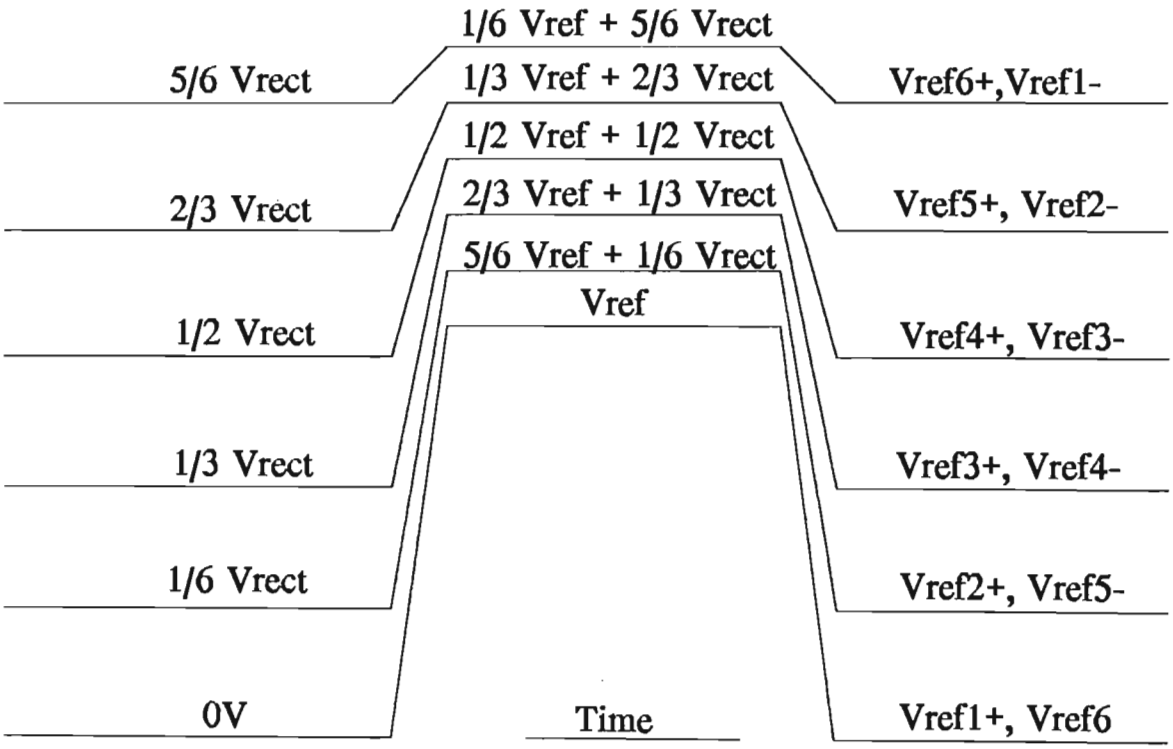

Fig 7.10 : Pictorial representation of the six reference waveforms

A sample of either the positive rectifier input or negative rectifier input (whichever is present) is taken from the EHT rectifier bridge, and IC5 and its associated components produce a sample of the rectifier voltage which is always positive. Pulses which are simultaneously present are smoothed out by C8 and C9. The output is applied VR5 and IC7 to provide the required d.c. bias for

the six reference signals. Using this approach of taking a sample of the rectifier voltage ensures that, no matter what the magnitude of the rectifier input voltage, it is always equally shared by the six pass elements.

The preset potentiometer VR5 is used to set the d.c. bias such that, when there is no pulse at the modulator output, the input EHT rectifier voltage is shared equally over the six pass elements. Normally, for pulse outputs of up to 5000V, the rectifier voltage would be set to about 6000V, and between output pulses the 6000V input would be evenly divided over the six pass elements, i.e. 1000V each. Incorrect setting of VR5 would mean an excessive volt drop over the uppermost pass element (and therefore excessive stress) where the voltage output of VR5 is set too low. Alternatively, where VR5 may be set too high the uppermost pass element will have too little bias across it and may even bottom (saturate). Once the correct setting for VR5 has been found it will be independent of the rectifier voltage.

7.6.6 Polarity Sensing and Correction

In view of the basic requirement that the Pulse Modulator should be designed to accept negative and positive rectifier inputs and deliver pulses of the same polarity, some kind of automatic polarity sensing and correction was considered necessary. Of the seven attenuator networks, one will always be connected to the rectifier output via the rectifier bridge, i.e. input to the pulse modulator, and a second attenuator network will be connected to the output of the pulse modulator. These two networks swap roles automatically when the polarity of the rectifier input is reversed. Both networks provide buffered samples respectively of the rectifier input and the pulse output, and the rectifier sample will naturally always carry with it the polarity of the rectifier input.

The polarity sensing and control network is a discrete design which is very tolerant of input signal levels, more so than would be the case if monolithic logic IC's had been used. It is comprised of transistors Q1-Q5 and associated components D1,D2,C1,C2, and R1-R14. Two inputs are applied to the network, one being a sample of the rectifier input, and the second a sample of the pulse output, and these inputs are identified in the schematic as P1-1 and P1-26, being in effect the pin numbers of the connector by which they are applied to the circuit. Transistors Q1 and Q2 are connected in cascode configuration and provide a logical AND function.

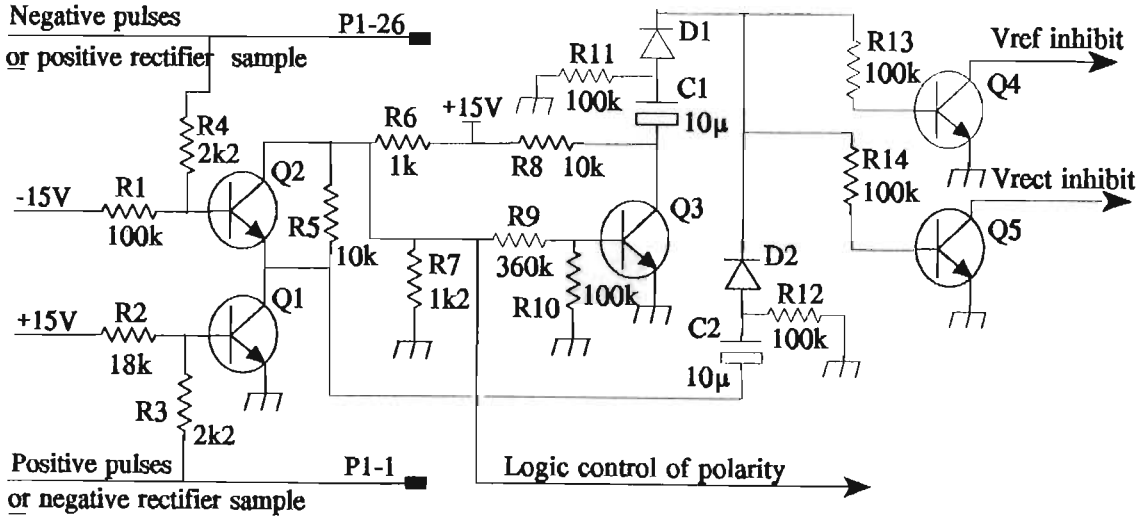

Fig 7.11 : Schematic of the polarity sensing and control circuits

For the case when the applied rectifier voltage is positive, the voltage at P1-1 is close to zero in the absence of any output pulses, and a voltage of nominally +8.5V (for a rectifier input of 6000V) is present at P1-26. Under these conditions both transistors Q1 and Q2 are

in conduction and the collector voltage of Q2 is low. This low voltage condition is applied to the control inputs A, B, and C of CD4053 CMOS switches used in the six control loops. The switches are triple SPDT configurations, type CD4053, and are used here exclusively for configuring the various circuits to operate optimally with both polarities.

In the second case, a voltage of approximately zero appears at P1-26 in the absence of output pulses, and P1-1 is at nominally -8.5V for a rectifier input of -6000V. Under these conditions both Q1 and Q2 are cut off, and the voltage at the collector of Q2 rises to +8V. This represents a "high" logic condition for the CMOS switch controls A, B, and C.

Transistors Q3, Q4, and Q5 apply a brief inhibit pulse of approximately 350ms duration to the reference circuit whenever there is a change of state in Q1 and Q2. A sudden change in state could represent an abrupt application of the rectifier voltage to the modulator, or a reversal in polarity, and the reference circuit is shut down to inhibit any output pulses during any transient conditions. This is largely intended as a protection mechanism for the pulse modulator, especially for the pass elements.

The CMOS switches connect the six reference signals to the six loop amplifiers in a certain order, depending on the output pulse polarity. The connection sequence to the amplifiers is reversed (mirror imaged) by the switches where the polarity is negative. This is necessary for the loops to operate correctly. The switches also select the requisite polarity feedback signal so that at the inputs to the loop amplifiers the signals are always positive.

7.6.7 Current Limiting

As part of the necessary protection for series pass elements the current has to be limited to a certain maximum value. In pulse mode this is set to 200mA, limited by safe operating area considerations, pulse width, and duty cycle. In the d.c. mode it has to be set considerably lower at 20mA because the duty cycle is 100%. The current limit is variable between 0 and 100% and is set at the front panel by means of VR1 (see schematic). The polarity of the current is determined by the polarity of the output pulse, and provision is made to regulate currents of either polarity.

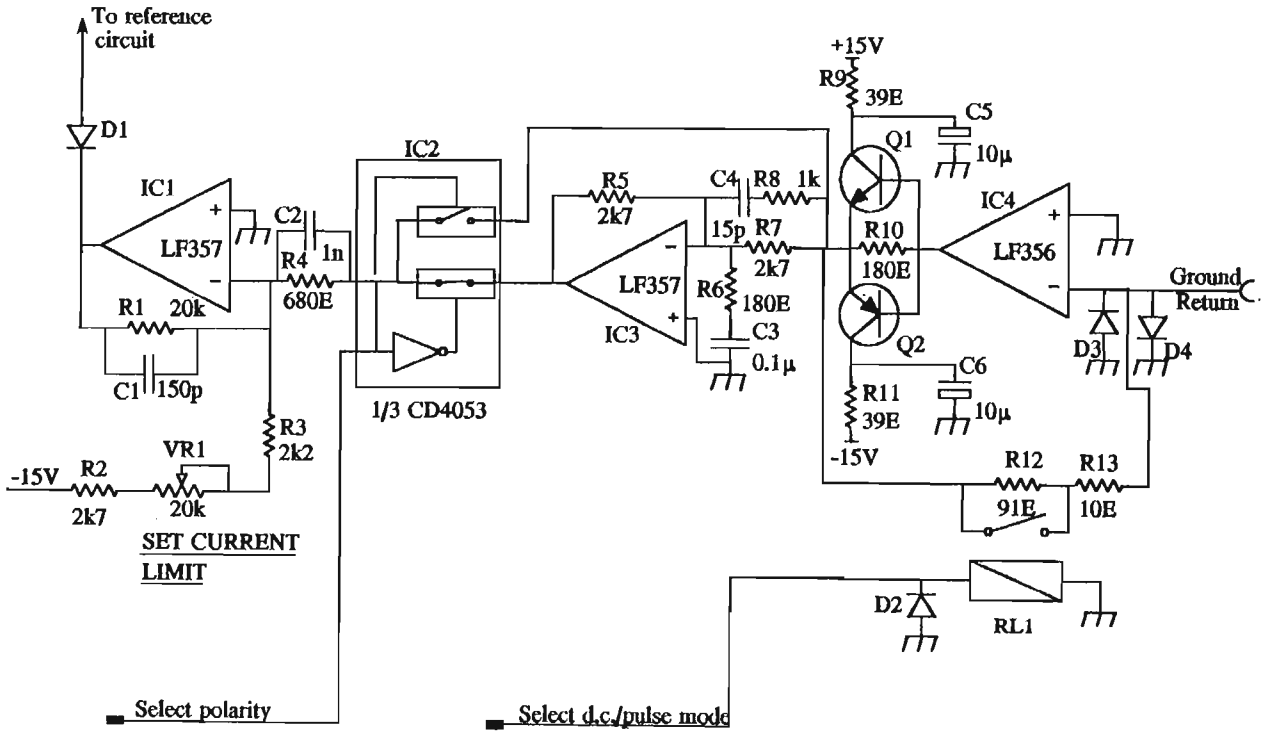

Fig 7.12 : Basic schematic of current limiting circuit

The schematic of the current-limiting circuit is shown in Fig 7.12. The GROUND RETURN terminal of the pulse

modulator is a virtual ground, not chassis ground. Load currents flow into this terminal which is the inverting input of a fast operational amplifier, IC4. The amplifier has at its output transistors Q1 and Q2 which sink or source the current through R12 and R13, and the output voltage at the emitters of Q1 and Q3 is therefore proportional to the load current, while the polarity of this voltage will be the inverse of the output pulse polarity. If the d.c. mode is selected the relay RL1 is not energised and the feedback resistance becomes 101 ohms instead of 10 ohms. This has the effect of reducing the value of the current limit by a factor ten. Diodes D3 and D4 are present to catch fast transients which would appear at the ground terminal while the feedback amplifier is still settling. The collectors of Q1 and Q2 are decoupled from the +15V and -15V supplies by C5,C6,R9, and R11 so that current surges do not interfere.

A fast unity-gain inverting amplifier (IC3) produces an inverted replica of the signal appearing at the emitters of Q1 and Q2. The inverted and non-inverted signals, proportional to the current flowing into the ground terminal, are applied to the CMOS switch IC2. Control over the switch selection is exercised by the polarity-sensing circuit such that only positive signals appear at the switch output, and these are applied as positive currents into the input of the inverting loop amplifier IC1 via R4 and C2. Also flowing into the same input is a negative current whose magnitude is determined by the setting of the current limit potentiometer VR1. The positive and negative currents are summed at this point. As long as the result remains negative the output of the current loop amplifier will be positive and will not influence the reference signals since diode D1 will be reverse biased. When the current is positive, i.e. the feedback current exceeds the current determined by the current limit potentiometer, the output of IC1 begins to swing negative

and , via D1, pulls down the reference signal, thus reducing the pulse output magnitude and consequently the load current.

The gain of the current limiting loop is largely determined by the value of the feedback resistor/input resistor ratio of the current loop amplifier, i.e. R1/R4. The transient response of the current limiting loop is governed by a number of delays, namely, the delays in the current limiting circuits and the delays in the main voltage regulating loops. The overall delay is considerable, and this leads to overshoot and instability in the output waveform when the current limit is exceeded and the current regulating loop is activated. This problem is brought under control by slowing down sufficiently the response of the current loop, and this is done by making C1 just large enough to minimise the overshoot.

The current limiting circuit may be isolated by using the CHASSIS GROUND terminal, which is true ground, instead of the GROUND RETURN.

7.6.8 Monitoring Circuits

An accurate estimate of the pulse magnitude was deemed to be important, as also the magnitude of the rectifier input. While the rectifier voltage would be easy to measure accurately, the pulse magnitude would not, complicated by the fact that the pulse could be of either polarity. The schematic of the monitoring circuits is shown in Fig 7.13. Positive and negative peak detectors have been separately implemented, and these operate on the samples obtained from the voltage dividers. On P1-1 the pulses are positive and these are delivered to the positive peak detector centred around IC2. In the input circuit of the positive peak detector R9 and C3 slow down the rise of the sample pulse, in particular to ensure that

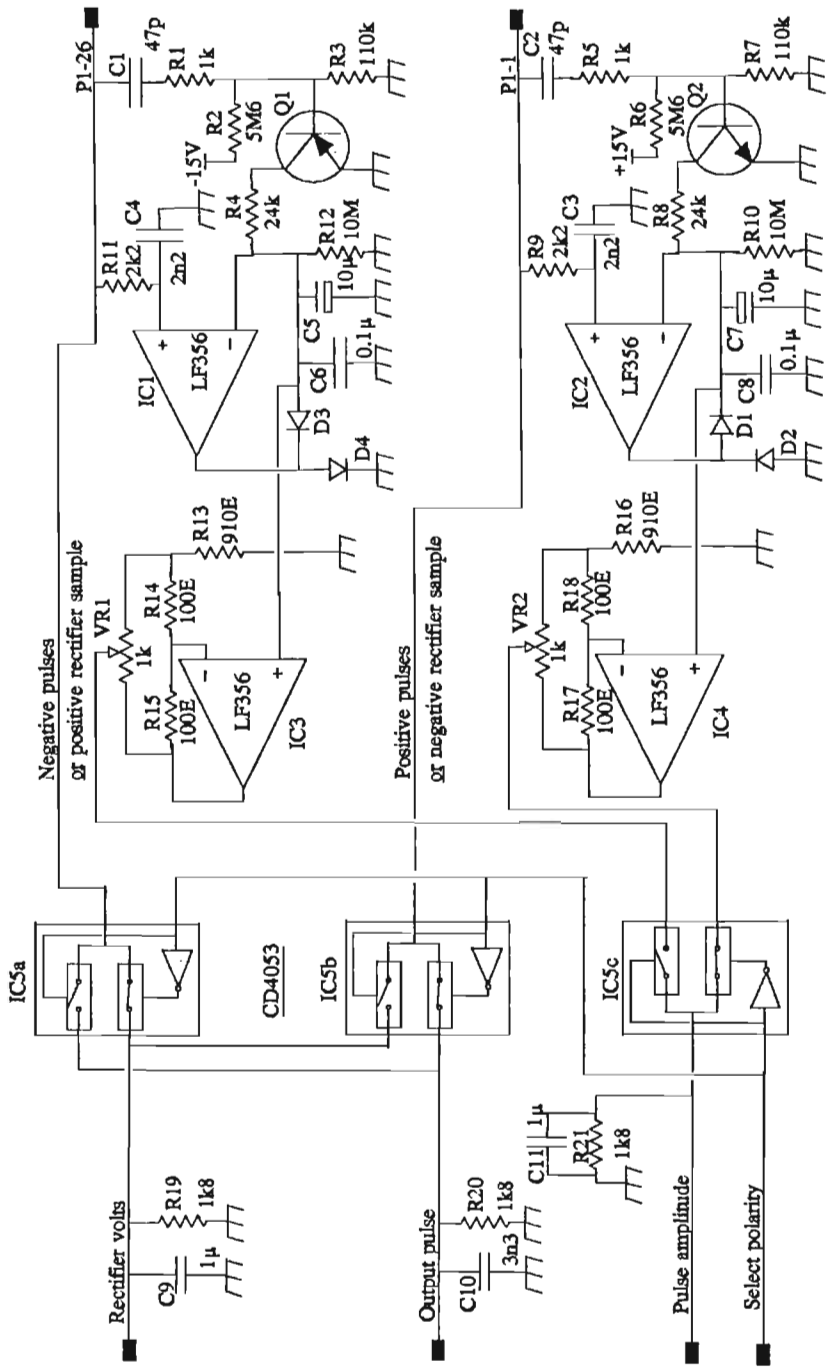

Fig 7.13 : Basic schematic of the monitoring circuits

the circuit does not respond to peak values of overshoot just beyond the leading edge which would then give false indications of the pulse amplitude. The time constant of R9 and C3 is approximately 4.8μs, sufficient to allow the pulse to settle. During the pulse the inputs to IC2 are unbalanced and charge is pumped via D1 into C7 and C8, and equilibrium is reached when the voltage on C7 is very slightly less than the peak value of the pulse. At equilibrium, the charge pumped into C7 is only just sufficient to replace charge lost between pulses. The decay time constant of the circuit is long, being about 100 seconds and largely determined by the value of R10, so that there is practically no droop on C7 between pulses. At the rise of each successive pulse transistor Q2 is very briefly pulsed into conduction, removing a little of the charge on C7 and C8 via R8 so that in the case where the pulse amplitude is reduced, the circuit does not take a long time to decay to the new but lower amplitude. Diode D2 clamps the output of IC2 near to -.7V between pulses, so that the output of IC2 does not have to slew from the negative supply rail to the value of the voltage on C7 before charge is pumped into the capacitor. This speeds up the response of the charge pump.

Voltage-follower IC4 provides a low impedance output for the voltage due to charge stored on C7. Although it is nominally a unity-gain amplifier, the gain of IC4 can be adjusted between .9 and 1.1 by means of VR2, and this provides a means of calibrating the gain of the monitoring circuit such that the d.c. output of the monitoring circuit is precisely 1 volt for every 1000V of peak pulse amplitude.

The operation of the negative peak detector IC1 is precisely the same as that of the positive peak detector except for the polarity, and IC3 provides the same voltage-follower function as IC4. The CMOS switch IC5,

under the control of the polarity selection mechanism, switches through to the front panel the appropriate signals and voltages, permitting monitoring by means of a digital multimeter and oscilloscope. In the presence of a rectifier input and output pulses, at the terminal RECTIFIER VOLTS on the front panel a voltage will appear (source resistance approximately 1k) which has the same polarity as the input rectifier voltage but is reduced in amplitude precisely 1000 times. This is also true for the OUTPUT PULSE terminal where a replica of the output pulse will appear, also reduced in magnitude by 1000 times, but otherwise having very much the same waveshape. For a precise measurement of the pulse amplitude a d.c. voltage can be measured with a digital multimeter at the PULSE AMPLITUDE terminal which is also set to give precisely 1V for every 1000V of output amplitude.

7.7 Experimental Results

During the development of the pulse modulator certain problems arose which had to be overcome.

7.7.1 Instabilities

Instabilities occurred during pulses, typically in the form of oscillations in the region of 50-100kHz. Between pulses the loop gain is much lower and problems were not experienced, but during pulses the loop gain reaches its maximum value and the loops became unstable. Development initially concentrated on getting a single loop to operate satisfactorily at a reduced voltage of about 1000V, and this was quite easily achieved with good waveforms. The difficulties increased, however, as a second and a third loop were added, and this led initially to spontaneous oscillations. This was partly due to the fact that when the pass elements were connected in series the effective series impedance seen by each element is much greater than

the actual load, which was typically about 40kohms, and the resulting voltage gain increased significantly. Another contributing factor was the distributed phase shift around each loop, increasing with frequency until phase inversion was reached and oscillation took place. The frequency of oscillation was typically in the region of 70kHz and only occurred during pulses. The problem of too much gain at the higher frequencies was eventually cured by placing in shunt across each element a small capacitor and a resistor in series to provide extra loading at these higher frequencies, thus reducing the loop gains and slowing down the response of the loops.

Eventually, all loops were operating together quite stably, but at the sacrifice of some speed, a compromise being reached between a tolerable level of overshoot and the speed of response. Currently, the rise and fall times are about 50μs between the 10% and 90% points for a 5000V output pulse. Performance is more or less the same for positive and negative output pulses, although there are slight differences in response and overshoot because the circuit configurations differ a little resulting in different delays around the loops.

7.7.2 Thermal Aspects

During the development of the system it was realised that efficient cooling of the pass elements would be necessary if the stress was to be minimised. It also was realised that power dissipation among the elements would not be uniformly the same, mainly due to the fact that each voltage divider would be drawing a not insignificant current. Considering that the voltage across each element is adjusted to approximately 1000V, the relative power dissipation would be proportional to the current in each one. The highest dissipation occurs in the element at the highest potential, i.e. the one connected to the rectifier

via the diode bridge. The static dissipation amounts to approximately 3.2W in the absence of pulses, and this rises to approximately 5.3W when the pulse modulator is driving a 40k load with 5000V pulses at a duty cycle of 10%.

Heatsinks having a coefficient of 13°K/W were bolted firmly to each BUY71 transistor, and the maximum temperature rise is restricted to about 60°C.

7.7.3 Output Impedance

Although a very low output impedance was originally targeted, this was not achievable in practice, mainly due to the fact that the high loop gains necessary for such a low impedance led to instability and distortion of the pulse. Practical impedances achieved lay between 500 and 1000 ohms.

7.7.4 Rise and Fall Times

While very rapid rise and fall times of a couple of microseconds for 5000V pulses would have been a good

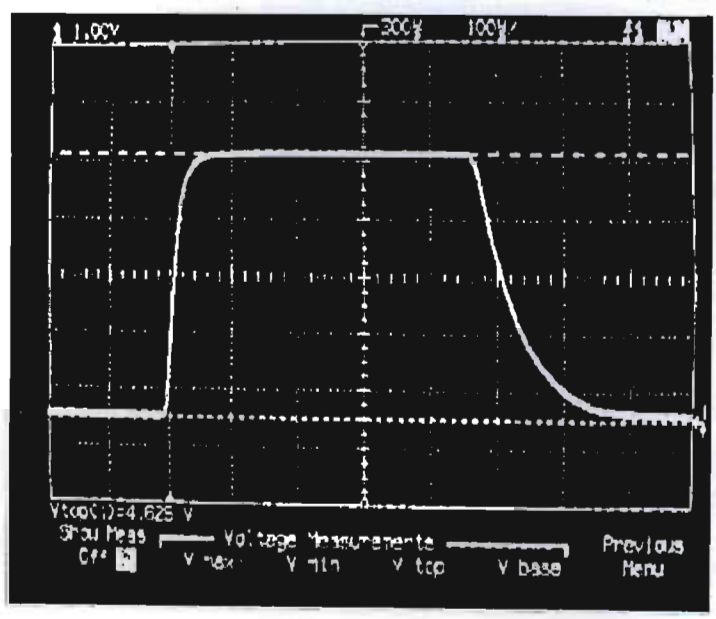

Fig 7.14 : Oscillogram of a positive 4625V pulse

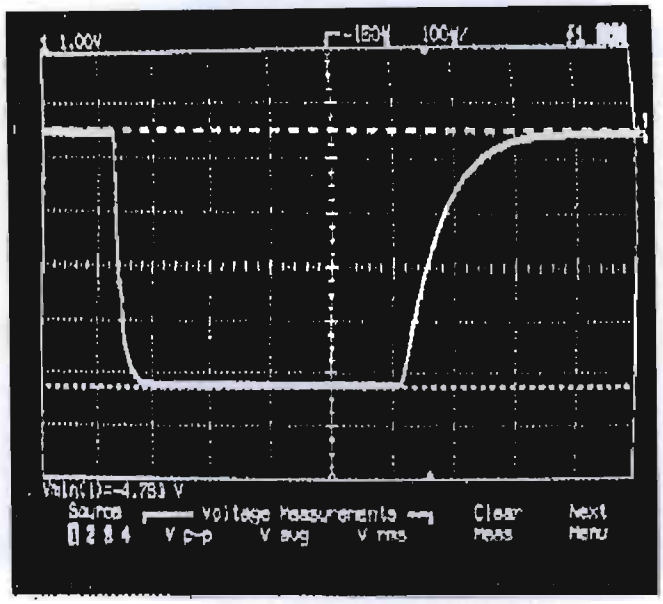

Fig 7.15 : Oscillogram of a negative 4781V pulse

achievement, it was not to be the case in practice. The response of the loops had to be slowed down and the loop gains reduced to a point where overshoot was restricted to a tolerable level, and this meant slower rise and fall times. The results may be seen in Figs 7.14 and 7.15. where samples of positive and negative pulses are displayed on an HP54601A oscilloscope. The oscilloscope timebase was set to 100μs/div. The sample pulses were obtained from a calibrated and compensated 1000:1 resistive divider connected across the 56kΩ resistive load being driven by the pulse modulator. Inspection of the oscilloscope traces shows that the pulses rise rapidly, settling within 40μs to within a few percent of the final value, while the falltime is much longer (about 200μs). The reason for the long falltime is not completely clear. It may have something to do with the fact that at the end of the pulse the control loops are inactive, having shut off the pass elements and reduced the loop gains to zero.

Furthermore, the pulse modulator is only capable of sourcing current into the load, but cannot sink current, so any capacitance shunting the load would have to discharge through the load.

Using the current limit showed that there was an overshoot of about 150V at the leading edge of the pulse, settling to the regulated output voltage and current after 25μs. Naturally, if the load current was less than the value to which the current limit was set then there was no overshoot.

7.8 Safe Operation

As already would have been realised, the modulator is to be operated within safe limits in order not to overstress the pass elements. Three regions of safe operation are identified and these are:

a) a thermally limited region characterised by short pulse widths and low duty cycle where the dissipation in the pass elements due to the product of input/output potential difference and load current could cause excessive temperature rise. For practical reasons this temperature rise is restricted to 35°C

b) a region limited by second breakdown in the power transistors characterised by output pulses of medium length and low duty cycle, restricting the input/output differential across the pass elements for particular values of load current

c) a region of d.c. operation restricting the input/output differential and load current because of second breakdown limitations

These three regions are shown graphically in Figures 7.16, 7.17, and 7.18. In each case the safe area is the area below the curve.

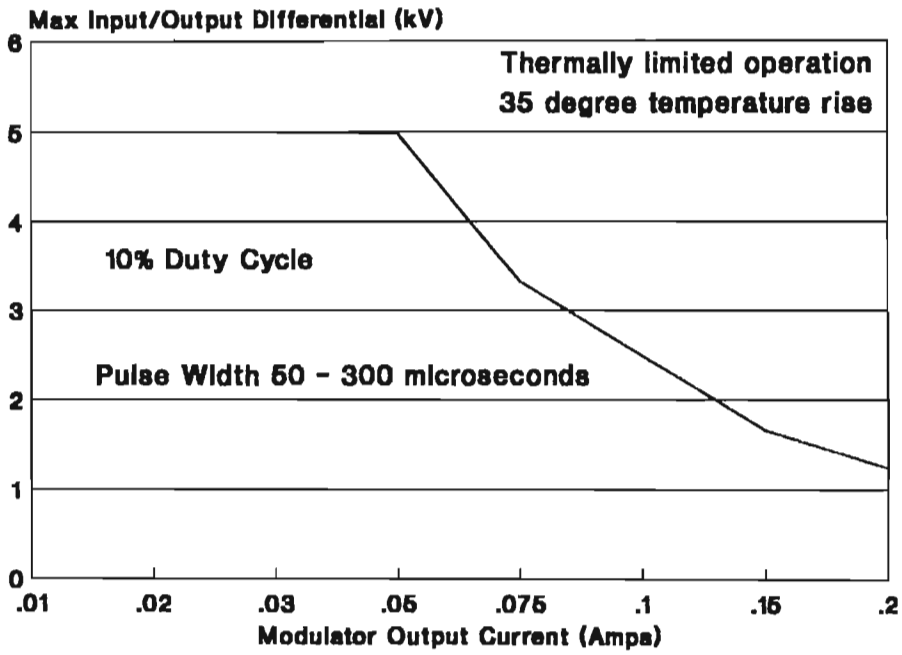

Fig.7.16: Safe operating area (thermally limited)

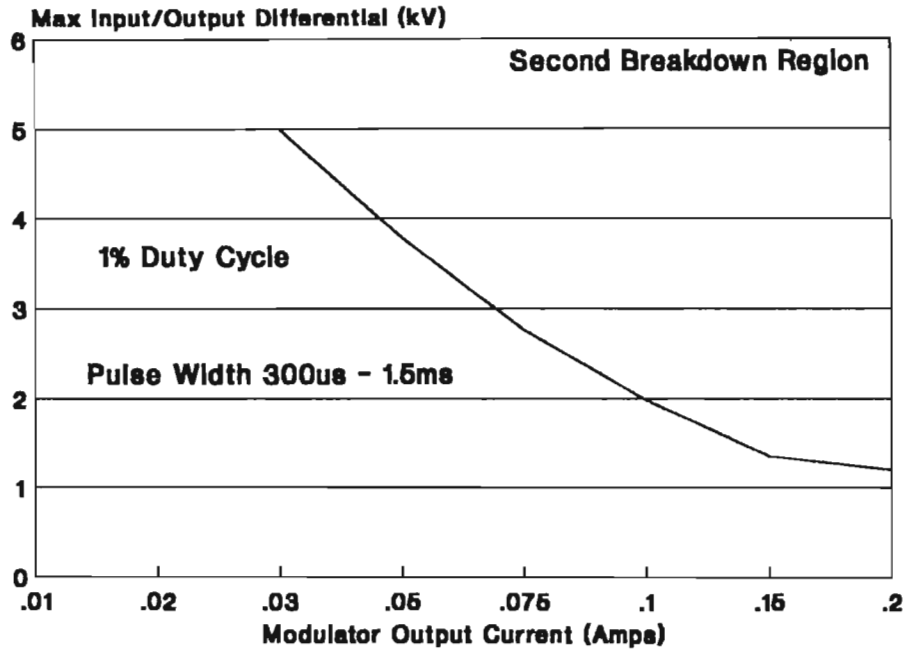

Fig.7.17: Safe operating area (second breakdown)

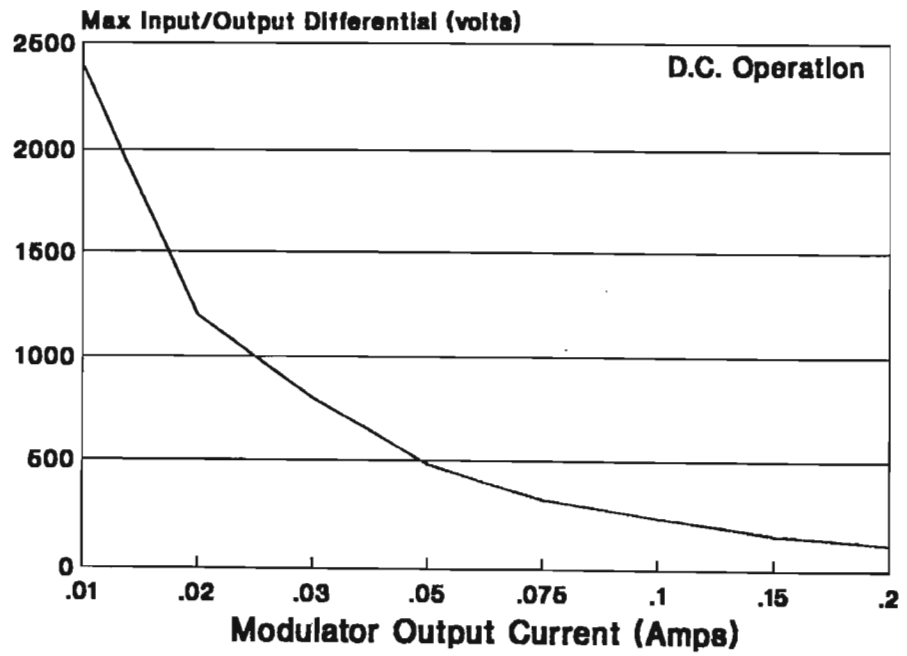

Fig.7.18: Safe operating area (d.c.)

APPENDIX A
THE PLASMA FREQUENCY

A fifth-order polynomial describing fairly accurately the current density varying with beam radius in the experimental tube has been presented:

$$P(r/r_0) = -24.04036.(r/r_0)^5 + 50.06149.(r/r_0)^4 - 28.20247.(r/r_0)^3 - .3901048.(r/r_0)^2 + 1.759072.(r/r_0) + 0.812392 \quad \ldots\ldots\ldots\ldots\ldots\ldots (2.62)$$

This normalised polynomial has a peak value of unity and a minimum value of zero at r = r_o. If J_o is the peak value of the current density then the current density at some radius r is

$$J(r/r_0) = J_0.P(r/r_0) \quad \ldots\ldots\ldots (A1)$$

It would be useful to relate the current density to the beam current which is known, and also the average current density to the peak value, J_o. Plainly,

$$I_0 = J_{ave}.\pi r_0^2 = \int_0^{r_0} J_0.P(r/r_0).2\pi r.dr$$

$$J_{ave} = 2J_0 \int_0^1 P(r/r_0) \,.\, (r/r_0) \,.\, d(r/r_0)$$

from which

$$J_0 = 3.052911 . J_{ave} = 0.9717718 . \frac{I_0}{r_0^2} \qquad \ldots\ldots\ldots\ldots\ldots\ldots (A2)$$

Therefore, generally, the current density as a function of beam current I_o, beam radius r_o, and position r in the beam can be given as

$$J(r/r_0) = 0.9717718 . \frac{I_0}{r_0^2} . P(r/r_0) \qquad \ldots\ldots\ldots\ldots\ldots\ldots (2.63)$$

The plasma frequency is given by

$$\omega_p = \left(\frac{J(r/r_0) \,.\, \eta}{u_0 \cdot \varepsilon_0} \right)^{1/2}$$

$$= 1.830212x10^8 . \frac{J(r/r_0)^{1/2}}{V^{1/4}}$$

$$= 1.80495x10^8 . \frac{I_0^{1/2}}{r_0 V^{1/4}} . P(r/r_0)^{1/2} \qquad \ldots\ldots\ldots\ldots\ldots\ldots (A3)$$

The square root of the dimensionless fifth-order polynomial $P(r/r_o)$ can easily be found and may be approximated by another fifth-order polynomial such that

$$P(r/r_0)^{1/2} = -43.10119.(r/r_0)^5 + 101.0324.(r/r_0)^4 - 79.97003.(r/r_0)^3 + 23.54151.(r/r^0)^2 - 2.50259.(r/r_0) + 1.043391 \quad \ldots\ldots\ldots\ldots\ldots\ldots (A4)$$

Of interest would be the mean plasma frequency within the beam, and this may be found by integrating the expression for the plasma frequency in (A3) over the beam radius r_o :

$$\omega_p(ave) = 1.80495x10^8 . \frac{I_0^{1/2}}{r_0 V^{1/4}} . \int_0^1 P(r/r_0)^{1/2} . d(r/r_0)$$

$$= 1.208787x10^8 . \frac{I_0^{1/2}}{r_0 V^{1/4}} \quad \ldots\ldots\ldots\ldots\ldots\ldots (A5)$$

APPENDIX B

PLASMA FREQUENCY REDUCTION FACTOR

The reduced, or effective, plasma frequency, ω_q, is an important parameter in microwave tube design, and is always less than the plasma frequency by the plasma frequency reduction factor F. The full plasma frequency ω_p is used for large plasma's, since F is then close to unity, but is reduced for electron beams of cross-section which is small in terms of the operating wavelength. The effective plasma frequency, ω_q, is related to the plasma frequency as follows :

$$\omega_q = F.\omega_p$$

The plasma frequency reduction factor F is derived from equation 9-44 in [29] as :

$$F = \left(\frac{p^2}{p^2 + \gamma^2}\right)^{1/2} \qquad \ldots\ldots\ldots\ldots\ldots\ldots (B1)$$

where the radial propagation constants γ and p are related by the transcendental equation 9-43 in [29] :

$$\gamma r.\frac{J_1(\gamma r)}{J_0(\gamma r)} = -pr.\left(\frac{I_1(pr).K_0(pa) + K_1(pr).I_0(pa)}{I_0(pr).K_0(pa) - K_0(pr).I_0(pa)}\right) \qquad \ldots\ldots\ldots\ldots\ldots\ldots (B2)$$

where a is the helix radius and r the beam radius. The radial propagation constant p relates to that region between beam and helix where no space charge is present.

The propagation constant γ relates to the region within the beam and is complex producing growth or decay in waves propagating within the beam. The transcendental equation above cannot be solved directly for γ but requires the use of iterative or graphical methods. The transcendental equation can be evaluated using polynomial approximations [41] for the Bessel functions in the normal manner.

Letting

$$T = \frac{I_1(pr).K_0(pa) + K_1(pr).I_0(pa)}{I_0(pr).K_0(pa) - K_0(pr).I_0(pa)} \qquad \ldots\ldots\ldots\ldots\ldots (B3)$$

the equation [B2] can be rewritten and expressed in the following form :

$$\frac{\gamma r}{pr} + \frac{J_0(\gamma r)}{J_1(\gamma r)}.T = 0 \qquad \ldots\ldots\ldots\ldots\ldots\ldots\ldots\ldots (B4)$$

Normally, this equation would be solved by iteratively, adjusting the value of the variable until the error is reduced to an arbitrarily small quantity. This procedure is time-consuming, even on a computer, and a direct method would be preferable if at all possible. The Bessel functions Jo(γr) and J1(γr) can be expressed as polynomial approximations in the variable γr and their ratio found :

$$J_0(\gamma r) = 1 - \frac{(\gamma r)^2}{4} + \frac{(\gamma r)^4}{64} - \frac{(\gamma r)^6}{2304} + \frac{(\gamma r)^8}{147456} - \ldots\ldots$$

$$= 1 + a_2(\gamma r)^2 + a_4(\gamma r)^4 + a_6(\gamma r)^6 + a_8(\gamma r)^8 \ldots\ldots$$

$$\ldots\ldots\ldots\ldots\ldots\ldots (B5)$$

and

$$J_1(\gamma r) = \frac{\gamma r}{2} - \frac{(\gamma r)^3}{16} + \frac{(\gamma r)^5}{384} - \frac{(\gamma r)^7}{18432} + \ldots\ldots$$

$$= \frac{\gamma r}{2}(1 + b_2(\gamma r)^2 + b_4(\gamma r)^4 + b_6(\gamma r)^6 + \ldots)$$

$$\ldots\ldots\ldots\ldots\ldots\ldots (B6)$$

Taking the ratio of $J_0(\gamma r)$ and $J_1(\gamma r)$

$$\frac{J_0(\gamma r)}{J_1(\gamma r)} = \frac{2}{\gamma r}(1 + c_2(\gamma r)^2 + c_4(\gamma r)^4 + \ldots)$$

$$\ldots\ldots\ldots\ldots (B7)$$

where by division of one series by another [41]

$$c_2 = a_2 - b_2 = -\frac{1}{8} \qquad c_4 = a_4 - a_2 b_2 + b_2^2 - b_4 = -\frac{1}{96}$$

Therefore

$$\frac{J_0(\gamma r)}{J_1(\gamma r)} = \frac{2}{\gamma r} - \frac{(\gamma r)}{4} - \frac{(\gamma r)^3}{96} - \ldots\ldots$$

$$\ldots\ldots\ldots\ldots (B8)$$

Substituting into the transcendental equation (B4) above

$$\frac{\gamma r}{pr} + \frac{2T}{\gamma r} - \frac{T.(\gamma r)}{4} - \frac{T.(\gamma r)^3}{96} = 0$$

$$\ldots\ldots\ldots\ldots (B9)$$

Multiplying and rearranging

$$\frac{T.(\gamma r)^4}{96} + \left(\frac{T}{4} - \frac{1}{pr}\right)(\gamma r)^2 - 2T = 0$$

.....(B10)

This equation is quadratic in $(\gamma r)^2$ and therefore

$$(\gamma r)^2 = \frac{-\left(\frac{T}{4} - \frac{1}{pr}\right) - \sqrt{\left(\frac{T}{4} - \frac{1}{pr}\right)^2 + \frac{T^2}{12}}}{\frac{T}{48}}$$

.....(B11)

and from this

$$\frac{\gamma^2}{p^2} = \frac{-48\left(\frac{T}{4} - \frac{1}{pr}\right) - 48\sqrt{\left(\frac{T}{4} - \frac{1}{pr}\right)^2 + \frac{T^2}{12}}}{p^2r^2T}$$

.....(B12)

Rearranging again

$$F = \sqrt{\left(\frac{p^2}{p^2 + \gamma^2}\right)} = \sqrt{\frac{p^2r^2T}{p^2r^2T - 48\left(\frac{T}{4} - \frac{1}{pr}\right) - 48\sqrt{\left(\frac{T}{4} - \frac{1}{pr}\right)^2 + \frac{T^2}{12}}}}$$

.....(B13)

APPENDIX C

DERIVATION OF THE ELECTRONIC EQUATIONS

The small-signal behaviour of the two slow waves and the fast wave propagating in the beam in the forward direction are governed by the well-known equations, [32]:

$$y^3 + by^2 - y(3x^2 + 2dx + 4QC) - 4QCb - bx^2 - 1 = 0$$

$$x^3 + dx^2 - x(3y2 + 2by - 4QC) + 4QCd - dy^2 = 0$$

$$\ldots\ldots\ldots\ldots\ldots\ldots\ldots\ldots\ldots\ldots\ldots\ldots\ldots (C1)$$

These equations are based on the assumption that gain parameter C is very small but that QC is still finite. They are derived from the circuit and electronic equations which must be simultaneously satisfied, and all terms containing C and higher powers of C are discarded in order to simplify the equations and make them more manageable, while those containing QC are retained so that the effects of space charge are still included.

It was felt that, because of the wide range of values assumed by C in the current application (due to, for example, a fairly wide range of frequencies being considered), to neglect all terms in C might lead to significant errors under certain conditions, and it was decided therefore to modify the equations to include all terms containing C while discarding those of higher powers in C. The results obtained from using the modified equations would then be compared with those from the standard forms in order to see whether any meaningful differences existed. In fact, noticeable differences were later observed when simulating the gain of the tube.

The electronic and circuit equations are stated [45] as follows :

$$i = \frac{j\beta_0 I_0}{2V_0(\Gamma - j\beta_0)^2}.E$$

$$E = -\left[\frac{\Gamma^2\Gamma_0 K_0}{\Gamma^2 - \Gamma_0^2} + \frac{2jQ\Gamma^2 K_0}{\beta_0}\right]i$$

.....(C2)

From combining the circuit and electronic equations we get

$$-1 = \left[\frac{\Gamma^2\Gamma_0 K_0}{\Gamma^2 - \Gamma_0^2} + \frac{2jQ\Gamma^2 K_0}{\beta_0}\right]\left[\frac{j\beta_0}{(j\beta_0 - \Gamma)^2}\cdot\frac{I^0}{2V_0}\right]$$

.....[C3]

By definition we have

$$C^3 = \frac{K_0 I_0}{4V0} \qquad \Gamma = j\beta_0(1 + jC\delta) \qquad \Gamma_0 = j\beta_0(1 + Cb - jCd)$$

$$\beta_0 = \frac{\omega}{u_0} \qquad \delta = x + jy$$

By substitution of the above definitions into eqn.[C3] the following is obtained :

$$\frac{2C^3\Gamma^2\Gamma_0}{(\Gamma^2 - \Gamma_0^2)}\cdot\frac{j\beta_0}{\beta_0^2 C^2\delta^2} = \frac{-2j\left[1 - C^2\delta^2 + 2jC\delta\right]\left[Cd + j(1 + Cb)\right]}{\delta^2\left[\delta + d + jb\right]\left[j(2 + Cb) + Cd - C\delta\right]}$$

and

$$\frac{4jQC^3\Gamma^2}{\beta_0}\cdot\frac{j\beta_0}{\beta_0^2 C^2\delta^2} = \frac{4QC}{\delta^2}.(1 - C^2\delta^2 + 2jC\delta)$$

Therefore

$$-1 = \frac{-2j(1 - C^2\delta^2 + 2jC\delta)(Cd + j(1 + Cb))}{\delta^2(\delta + d + jb)(j(2 + Cb) + Cd - C\delta)} + \ldots$$

$$+ \frac{4QC}{\delta^2}(1 - C^2\delta^2 + 2jC\delta)$$

$$\ldots\ldots\ldots\ldots\ldots\ldots\ldots\ldots\ldots\ldots [C4]$$

Multiplying out on both sides and discarding those terms containing C^2 and higher and retaining those containing C and QC^2 we get

$$LHS = C\delta^4 + Cb^2\delta^2 + 2b\delta^2 - Cd^2\delta^2 - 2j\delta^3 - 2jd\delta^2 - 2jCbd\delta^2$$

$$RHS = 2 + 2Cb - 2jCd + 4jC\delta + 4QC(Cd^2 - 2b - Cb^2 - 5C\delta^2 - 4Cd\delta + 2jCbd + 2j\delta + 2jd - 4jCb\delta)$$

Substituting $\delta = x + jy$

$$Re(LHS) = Cx^4 + Cy^4 + Cb^2x^2 - Cb^2y^2 + 2bx^2 - 2by^2 - Cd^2x^2 + Cd^2y^2 - 6Cx^2y^2 + 6x^2y - 2y^3 + 4Cbdxy + 4dxy$$

$$Im(LHS) = -2x^3 + 6xy^2 - 2dx^2 + 2dy^2 - 2Cd^2xy + 4bxy + 2Cb^2xy + 4Cx^3y - 4Cxy^3 - 2Cbdx^2 + 2Cbdy^2$$

$$Re(RHS) = 2 + 2Cb - 4Cy + 4QC(Cd^2 - Cb^2 - 2b - 2y + 4Cby - 5Cx^2 + 5Cy^2 - 4Cdx)$$

$$Im(RHS) = -2Cd + 4Cx + 4QC(Cbd + 2x + 2d - 4Cbx - 10Cxy - 4Cdy)$$

Combining the real parts

$$Cx^4 + Cy^4 + Cb^2x^2 - Cb^2y^2 + 2bx^2 - 2by^2 - Cd^2x^2 + Cd^2y^2 - 6Cx^2y^2 + 6x^2y - 2y^3 + 4Cbdxy + 4dxy - 2 - 2Cb + 4Cy - 4QC(Cd^2 - Cb^2 - 2b - 2y + 4Cby - 5Cx^2 + 5Cy^2 - 4Cdx) = 0 \quad \ldots\ldots\ldots\ldots\ldots [C5]$$

Expressed as a quartic equation in y

$$Cy^4 - 2y^3 - y^2(2b + 6Cx^2 - Cd^2 + Cb^2 + 20QC^2) + y(6x^2 + 4dx + 4Cbdx + 4C + 8QC - 16QC^2b) + (Cx^4 + 2bx^2 - Cd^2x^2 + Cb^2x2 - 2 - 2Cb - 4QC^2d^2 + 4QC^2b^2 + 8QCb + 20QC^2x^2 + 16QC^2dx) = 0 \quad \ldots\ldots\ldots\ldots\ldots\ldots [C6]$$

Combining the imaginary parts

$$-2x^3 + 6xy^2 - 2dx^2 + 2dy^2 - 2Cd^2xy + 4bxy + 2Cb^2xy + 4Cx^3y - 4Cxy^3 - 2Cbdx^2 + 2Cbdy^2 + 2Cd - 4Cx - 4QC(Cbd + 2x + 2d - 4Cbx - 10Cxy - 4Cdy) = 0 \quad \ldots\ldots\ldots\ldots\ldots\ldots [C7]$$

Expressed as a cubic equation in x

$$x^3(1 - 2Cy) + x^2(d + Cbd) - x(3y^2 + 2by - 4QC - Cd^2y + Cb^2y - 2Cy^3 - 2C + 8QC^2b - 5Cy) - (dy^2 + Cbdy^2 + Cd - 2QC^2bd - 4QCd - 8QC^2dy) = 0 \quad \ldots\ldots\ldots\ldots\ldots\ldots [C8]$$

If the terms containing C are discarded then the equations [C6] and [C8] become the original equations

$$x^3 + dx^2 - x(3y^2 + 2by - 4QC) - dy^2 + 4QCd = 0$$

$$y^3 + by^2 - y(3x^2 + 2dx + 4QC) - 4QCb - bx^2 - 1 = 0$$

APPENDIX D

LAUNCHING LOSS IN A TRAVELLING-WAVE TUBE

Three waves are launched at the input of a travelling-wave tube which travel in the +z direction, and they have initially equal magnitudes:

$$E_1 + E_2 + E_3 = E_0$$

and therefore

$$E_1 = E_2 = E_3 = \frac{1}{3}E_0$$

Of these three waves, one shows little change in amplitude (in fact, a slight decay), another decays exponentially, and the third grows exponentially, and of the three only the last will show amplification. The magnitude of the growing wave is thus one-third of the input wave, and the initial loss is

$$A(dB) = -20\log(\frac{1}{3}) = 9.54dB$$

This would be reasonably correct where spacecharge effects and losses in the tube could be ignored, and the tube is operated under optimal conditions and gives maximum gain, but where these effects become significant the launching loss will depart significantly from the figure of 9.54dB. In particular, where gain control may be implemented in the tube by varying the beam voltage and thus the beam velocity , the velocity parameter b will assume a value significantly different from the nominal value of zero, being either positive or negative, and this will have quite a dramatic effect on the launching loss. This may be seen in Fig.10-12 of [46]. Furthermore, the launching loss

will be somewhat affected by the signal frequency, especially where the velocity parameter b departs significantly from zero. Since the launching loss obviously will affect the small-signal gain achieved in the tube, it seemed necessary to investigate it under varying conditions.

A simplified relationship for the launching loss is given in equation (10.93)of ref[47]:

$$A(dB) = -20\log\left[\frac{(\delta_1 - \delta_2)(\delta_1 - \delta_3)}{\delta_1^2(1 + jC\delta_2)(1 + jC\delta_3)} \cdot \frac{\delta_1^2}{\delta_1^2 + 4QC(1 + jC\delta_1)^2}\right] \quad \ldots\ldots\ldots\ldots\ldots\ldots\ldots [D1]$$

This relationship was first evaluated on a computer, but the results did not appear to be entirely satisfactory in that the values for the launching loss departed quite dramatically from what was expected, judging from those shown in Fig.10-12 of ref[46]. In particular, under certain conditions, the loss reached very large proportions suggesting that "holes" could arise in the small-signal tube gain over certain ranges of tube bias. For these reasons it was decided to independently derive a relationship for the launching loss, based on some original equations (equations (10.82) to (10.84)) of ref [48]. These equations are stated here again :

$$E_1 + E_2 + E_3 = E \quad \ldots\ldots\ldots\ldots\ldots\ldots (D2)$$

$$\frac{(\Gamma_1 - j\beta_0)E_1}{(\Gamma_1 - j\beta_0)^2 + \beta_{q1}^2} + \frac{(\Gamma_2 - j\beta_0)E_2}{(\Gamma_2 - j\beta_0)^2 + \beta_{q2}^2} + \frac{(\Gamma_3 - j\beta_0)E_3}{(\Gamma_3 - j\beta_0)^2 + \beta_{q3}^2} = 0$$

$$\ldots\ldots\ldots\ldots (D3)$$

and

$$\frac{E_1}{(\Gamma_1 - j\beta_0)^2 + \beta_{q1}^2} + \frac{E_2}{(\Gamma_2 - j\beta_0)^2 + \beta_{q2}^2} + \frac{E_3}{(\Gamma_3 - j\beta_0)^2 + \beta_{q3}^2} = 0$$

.....(D4)

By definition

$$-\Gamma_1 = -j\beta_0(1 + jC\delta_1) \quad \textit{which gives} \quad \Gamma_1 - j\beta_0 = -\beta_0 C\delta_1$$

$$-\Gamma_2 = -j\beta_0(1 + jC\delta_2) \quad \textit{which gives} \quad \Gamma_2 - j\beta_0 = -\beta_0 C\delta_2$$

$$-\Gamma_3 = -j\beta_0(1 + jC\delta_3) \quad \textit{which gives} \quad \Gamma_3 - j\beta_0 = -\beta_0 C\delta_3$$

where Γ_1, Γ_2, and Γ_3 are the propagation constants respectively for the gaining slow wave, the decaying slow wave, and for the fast wave, while the δ_n are the associated propagation factors determining the growth, decay, and phase shift in the waves. The reduced plasma frequency phase constants are defined as :

$$\beta_{qn}^2 = -4QC^3\Gamma_n^2 = 4QC^3\beta_0^2(1 + jC\delta_n)^2$$

and therefore

$$(\Gamma_n - j\beta_0)^2 + \beta_{qn}^2 = \beta_0^2C^2(\delta_n^2 + 4QC(1 + jC\delta_n)^2)$$

Therefore the equations (D3) and (D4) can be written as

$$\frac{\delta_1 E_1}{\delta_1^2 + 4QC(1 + jC\delta_1)^2} + \frac{\delta_2 E_2}{\delta_2^2 + 4QC(1 + jC\delta_2)^2} + \ldots + \frac{\delta_3 E_3}{\delta_3^2 + 4QC(1 + jC\delta_3)^2} = 0$$

.....[D5]

and

$$\frac{E_1}{\delta_1^2 + 4QC(1 + jC\delta_1)^2} + \frac{E_2}{\delta_2^2 + 4QC(1 + jC\delta_2)^2} + \ldots$$

$$+ \frac{E_3}{\delta_3^2 + 4QC(1 + jC\delta_3)^2} = 0$$

$$\ldots\ldots\ldots\ldots\ldots\ldots [D6]$$

Using the notation in Eqn [D5] and multiplying through

$$(\delta_n^2) = \delta_n^2 + 4QC(1 + jC\delta_n)^2$$

$$\ldots\ldots\ldots [D7]$$

$$\delta_1 E_1 (\delta_2^2)(\delta_3^2) + \delta_2 E_2 (\delta_1^2)(\delta_3^2) + \delta_3 E_3 (\delta_1^2)(\delta_2^2) = 0$$

$$\ldots\ldots\ldots\ldots\ldots\ldots [D8]$$

Substituting in (D8)for E_2 we obtain

$$\frac{E_2}{E} = 1 - \frac{E_1}{E} - \frac{E_3}{E}$$

and therefore

$$E_1[\delta_1(\delta_2^2)(\delta_3^2) - \delta_2(\delta_1^2)(\delta_3^2)] + E_3[\delta_3(\delta_1^2)(\delta_2^2) - \delta_2(\delta_1^2)(\delta_3^2)]$$

$$= -E\delta_2(\delta_1^2)(\delta_3^2)$$

$$\ldots\ldots\ldots\ldots\ldots\ldots [D9]$$

We have also from (D6) that

$$E_1(\delta_2^2)(\delta_3^2) + E_2(\delta_1^2)(\delta_3^2) + E_3(\delta_1^2)(\delta_2^2) = 0$$

$$\ldots\ldots\ldots\ldots\ldots [D10]$$

Substituting again in (D10)for $E_2 = E - E_1 - E_3$ we obtain

$$E_1[(\delta_2^2)(\delta_3^2) - (\delta_1^2)(\delta_3^2)] + E_3[(\delta_2^2)(\delta_1^2) - (\delta_1^2)(\delta_3^2)] = -E(\delta_1^2)(\delta_3^2)$$

.....(D11)

from which

$$E_3 = -E_1\left(\frac{(\delta_2^2)(\delta_3^2) - (\delta_1^2)(\delta_3^2)}{(\delta_2^2)(\delta_1^2) - (\delta_1^2)(\delta_3^2)}\right) - \frac{E(\delta_1^2)(\delta_3^2)}{(\delta_2^2)(\delta_1^2) - (\delta_1^2)(\delta_3^2)}$$

.....(D12)

Substituting for E_3 in equation (D9) we obtain after some manipulation

$$\frac{E}{E_1} = \frac{(\delta_2 - \delta_1)(\delta_3^2) + (\delta_1 - \delta_3)(\delta_2^2) + (\delta_3 - \delta_2)(\delta_1^2)}{(\delta_1^2)(\delta_3 - \delta_2)}$$

.....(D13)

Following the same procedure and using the same equations we obtain

$$\frac{E}{E_2} = \frac{(\delta_2 - \delta_3)(\delta_1^2) + (\delta_1 - \delta_2)(\delta_3^2) + (\delta_3 - \delta_1)(\delta_2^2)}{(\delta_2^2)(\delta_3 - \delta_1)}$$

.....(D14)

and

$$\frac{E}{E_3} = \frac{(\delta_3 - \delta_2)(\delta_1^2) + (\delta_1 - \delta_3)(\delta_2^2) + (\delta_2 - \delta_1)(\delta_3^2)}{(\delta_3^2)(\delta_2 - \delta_1)}$$

.....(D15)

In each case the numerator is the same. Therefore, since

$E_n = V_n\Gamma_n$ we have for the reciprocal of the launching loss for the gaining slow wave

$$\frac{V}{V_1} = 1 + \frac{E_2\Gamma_1}{E_1\Gamma_2} + \frac{E_3\Gamma_1}{E_1\Gamma_3} \qquad \text{.....(D16)}$$

and by substituting for E_1, E_2, and E_3 in equation (D16) we obtain

$$\frac{V}{V_1} = 1 + \frac{(\delta_2^2)(\delta_1 - \delta_3)(1 + jC\delta_1)}{(\delta_1^2)(\delta_3 - \delta_2)(1 + jC\delta_2)} + \frac{(\delta_3^2)(\delta_2 - \delta_1)(1 + jC\delta_1)}{(\delta_1^2)(\delta_3 - \delta_2)(1 + jC\delta_3)} \qquad \text{.....(D17)}$$

This result differs somewhat from that presented in equation (10-90) in ref [47]. The voltage V is the total input signal and V_1 is that part of the input signal which sets up the growing slow wave. Expressed in decibels the launching loss is $20\log(V_1/V)$. Recalling that

$$\delta_n = x_n + jy_n$$

we can substitute for the δ_n in the loss equation above, using values obtained for the six roots x1, x2, x3, y1, y2, and y3 by simultaneously solving the two cubic equations. The values obtained for the δ_n will vary with signal frequency, space charge, helix loss, beam voltage and current, and tube dimensions, and the launching loss may therefore also be expected to depend to some extent on these parameters.

In the same manner the launching losses for the decaying slow wave and fast wave can be found from equations similar to (D17), derived in the same way.

From

$$\frac{V}{V_2} = 1 + \frac{E_1\Gamma_2}{E_2\Gamma_1} + \frac{E_3\Gamma_2}{E_2\Gamma_3} \qquad \ldots\ldots\ldots\ldots (D18)$$

we get for the decaying slow wave

$$\frac{V}{V_2} = 1 + \frac{(\delta_1^2)(\delta_2 - \delta_3)(1 + jC\delta_2)}{(\delta_2^2)(\delta_3 - \delta_1)(1 + jC\delta_1)} + \frac{(\delta_3^2)(\delta_1 - \delta_2)(1 + jC\delta_2)}{(\delta_2^2)(\delta_3 - \delta_1)(1 + jC\delta_3)} \qquad \ldots\ldots\ldots\ldots\ldots (D19)$$

and from

$$\frac{V}{V_3} = 1 + \frac{E_1\Gamma_3}{E_3\Gamma_1} + \frac{E_2\Gamma_3}{E_3\Gamma_2} \qquad \ldots\ldots\ldots\ldots (D20)$$

we get for the fast wave

$$\frac{V}{V_3} = 1 + \frac{(\delta_1^2)(\delta_2 - \delta_3)(1 + jC\delta_3)}{(\delta_3^2)(\delta_1 - \delta_2)(1 + jC\delta_1)} + \frac{(\delta_2^2)(\delta_3 - \delta_1)(1 + jC\delta_3)}{(\delta_3^2)(\delta_1 - \delta_2)(1 + jC\delta_2)} \qquad \ldots\ldots\ldots\ldots\ldots (D21)$$

Expressed in decibels the launching losses are given by

$$A_{Ln}(dB) = 20\log(V_n/V)$$

In Fig D-1 are some plots of the computed launching losses for the experimental tube, showing how the losses would vary with changing cathode voltage and with frequency as a parameter.

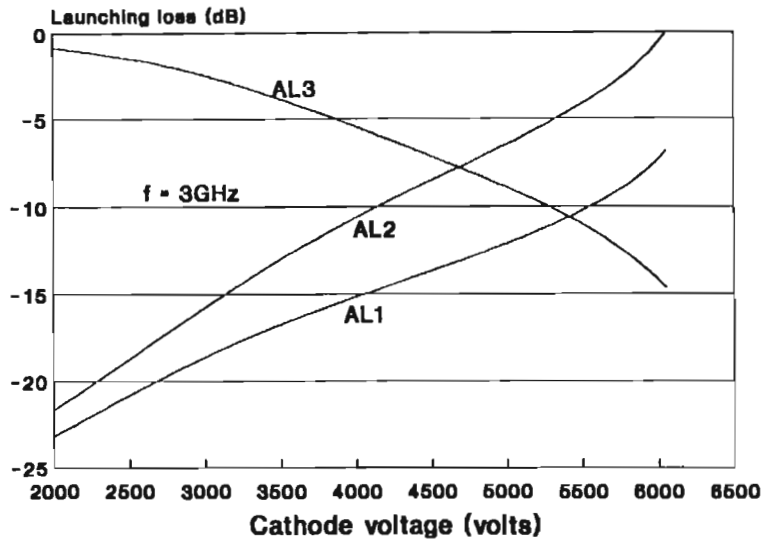

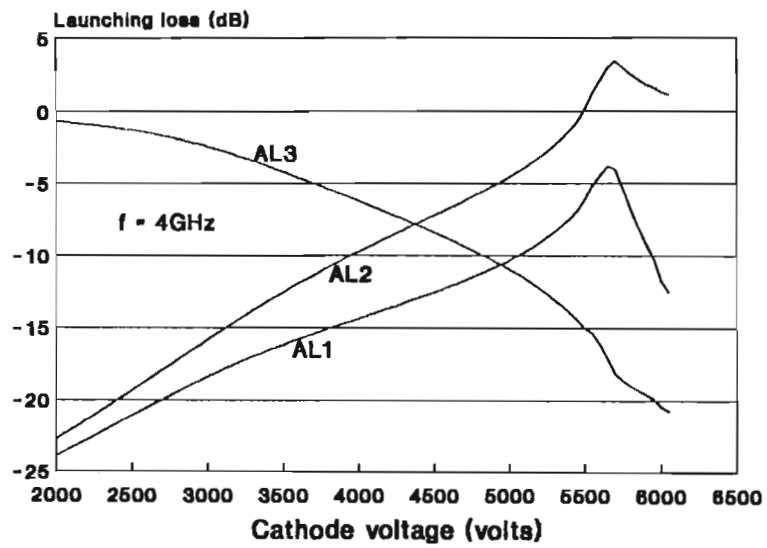

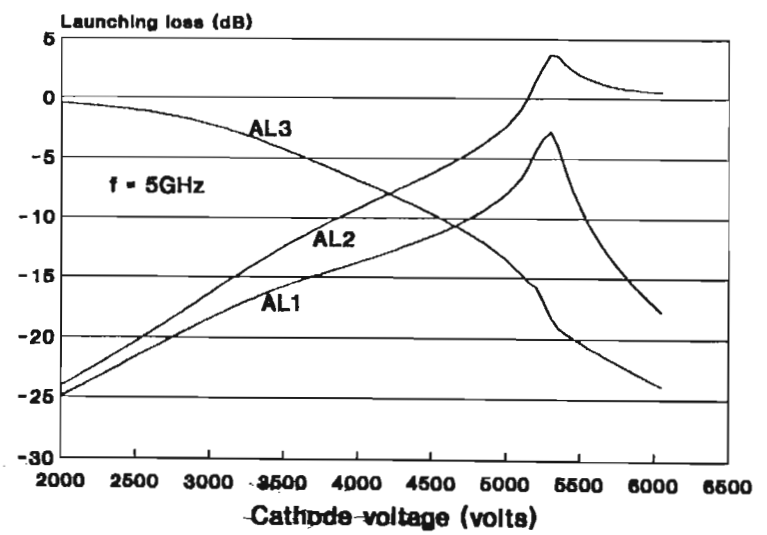

Fig D-1(a),(b),and (c): Launching losses for 3,4, and 5GHz

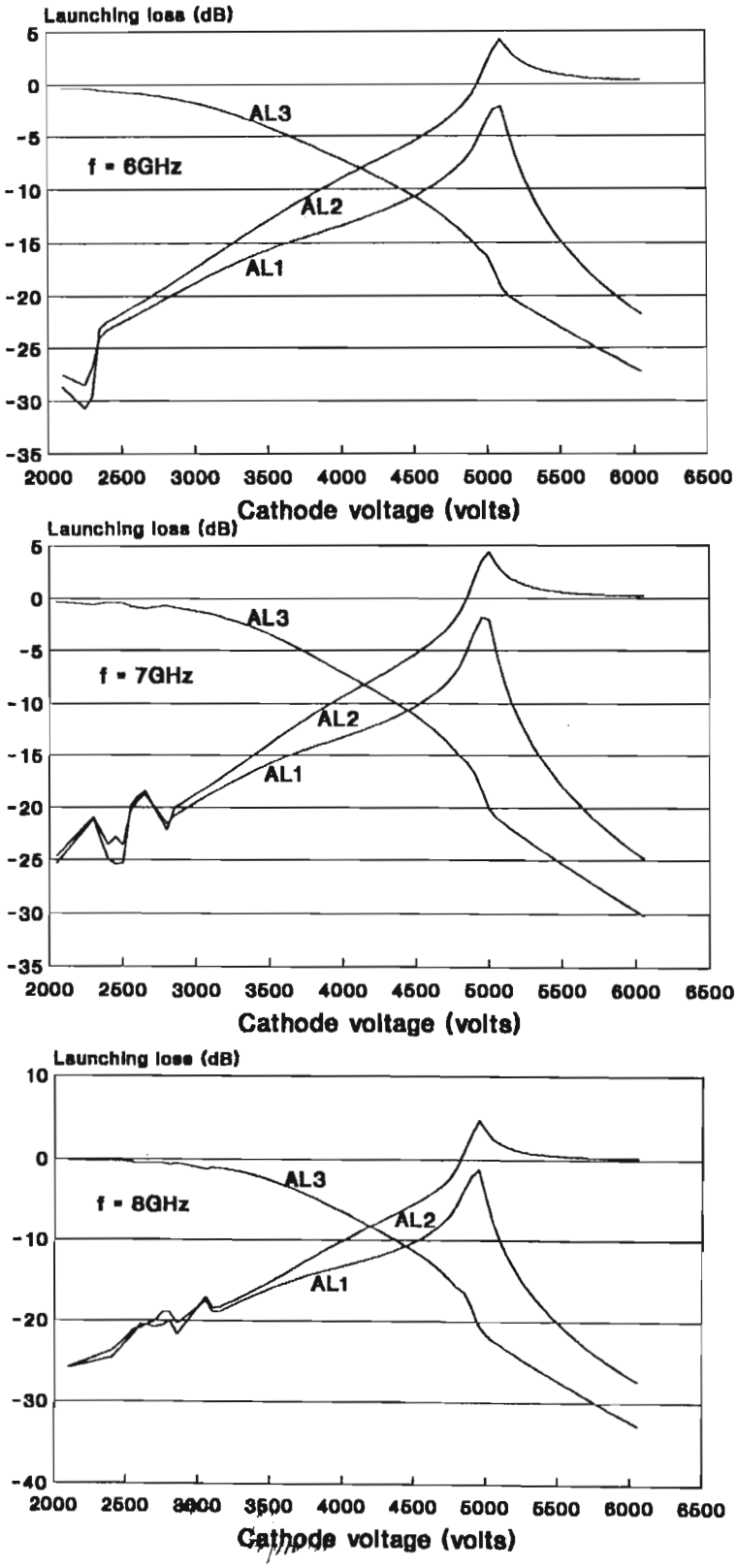

Fig D-1(d),(e),and (f): Launching losses for 6, 7, and 8GHz

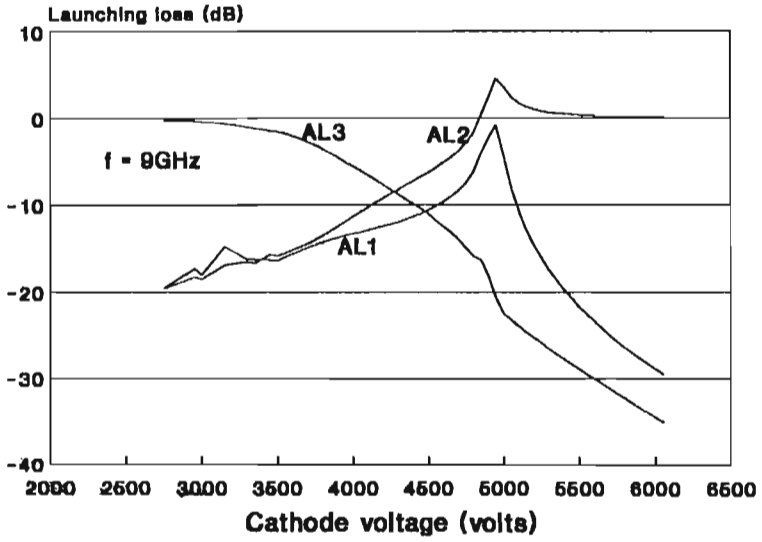

Fig D-1(g): Launching losses for 9GHz

APPENDIX E

SMALL SIGNAL TWT GAIN IN THE PRESENCE OF INTERNAL REFLECTIONS AND FEEDBACK

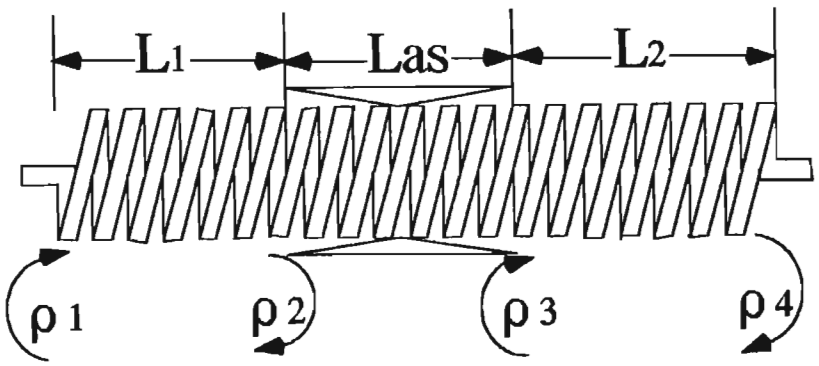

Fig E-1 : Helix with attenuator showing points of reflection

$$\rho_1 = \rho_4 = \frac{Z_0 - Z_H}{Z_0 + Z_H} \qquad \rho_2' = -\rho_2 \qquad \rho_3' = -\rho_3 \qquad \rho_3 = -\rho_2$$

Altogether, four points of reflection are identified with corresponding reflection coefficients. Reflections within the helix due, for example, to minor irregularities in pitch are ignored.

The small-signal TWT gain may be expressed more accurately by taking all three waves into account. The three waves are excited at the TWT input by the input field E, and at some point z beyond the input can be expressed as follows:

$$E_1 = A_{L1}E.\exp\left(-j\beta_0 z + \beta_0 C\delta_1 z\right) \qquad \text{(gaining slow wave)}$$

$$E_2 = A_{L2}E.\exp\left(-j\beta_0 z + \beta_0 C\delta_2 z\right) \qquad \text{(decaying slow wave)}$$

$$E_3 = A_{L3}E.\exp\left(-j\beta_0 z + \beta_0 C\delta_3 z\right) \qquad \text{(fast wave)}$$

.....(E1)

where the $\delta_n = x_n + jy_n$ are the solutions to the electronic equations and the A_{Ln} are the respective input launching losses presented as fractions of the input field E. Rearranging

$$E_1 = A_{L1}E.\exp\left(\beta_0 C x_1 z\right)\left[\cos\left(-\beta_0 z(1-Cy_1)\right)+j\sin\left(-\beta_0 z(1-Cy_1)\right)\right]$$

$$E_2 = A_{L2}E.\exp\left(\beta_0 C x_2 z\right)\left[\cos\left(-\beta_0 z(1-Cy_2)\right)+j\sin\left(-\beta_0 z(1-Cy_2)\right)\right]$$

$$E_3 = A_{L3}E.\exp\left(\beta_0 C x_3 z\right)\left[\cos\left(-\beta_0 z(1-Cy_3)\right)+j\sin\left(-\beta_0 z(1-Cy_3)\right)\right]$$

.....E2

The three waves leaving the input after launching propagate towards the output and are individually reflected back towards the input . At the input they are reflected again and combine with the input wave as they propagate toward the output.

For the three waves reflected from the interface between the input helix section and the attenuator, and which then combine with the input wave:

$$E_1' = A_{L1}\rho_1\rho_2 E.\exp\left[\beta_0 C L_1 (x_1 - d_1\right].\exp\left[-j\beta_0 L_1 (2 - Cy_1)\right]$$

$$E_2' = A_{L2}\rho_1\rho_2 E.\exp\left[\beta_0 C L_1 (x_2 - d_1\right].\exp\left[-j\beta_0 L_1 (2 - Cy_2)\right]$$

$$E_3' = A_{L3}\rho_1\rho_2 E.\exp\left[\beta_0 C L_1 (x_3 - d_1\right].\exp\left[-j\beta_0 L_1 (2 - Cy_3)\right]$$

.....E3

where β_o is the axial propagation constant for a dielectrically-loaded helix in a metal shell, L_1 is the length of the helix section from the input to the interface with the attenuator, d_1 is the helix loss factor for this section of the helix, and C is Pierce's gain parameter.

For the three waves returning after reflection from the second interface (output) of the attenuator and after reflection at the input :

$$E_1'' = A_{L1}\rho_1\rho_3 E.\exp\left[\beta_0 C\left(L_1 (x_1 - d_1) + L_{as} (x_{1a} - d_2)\right]\right.\cdot$$
$$\cdot\exp\left[-j\beta_0\left(L_1 (2 - Cy_1) + L_{as} (2 - Cy_{1a})\right]\right.$$

$$E_2'' = A_{L2}\rho_1\rho_3 E.\exp\left[\beta_0 C\left(L_1 (x_2 - d_1) + L_{as} (x_{2a} - d_2)\right]\right.\cdot$$
$$\cdot\exp\left[-j\beta_0\left(L_1 (2 - Cy_2) + L_{as} (2 - Cy_{2a})\right]\right.$$

$$E_3'' = A_{L3}\rho_1\rho_3 E.\exp\left[\beta_0 C\left(L_1 (x_3 - d_1) + L_{as} (x_{3a} - d_2)\right]\right.\cdot$$
$$\cdot\exp\left[-j\beta_0\left(L_1 (2 - Cy_3) + L_{as} (2 - Cy_{3a})\right]\right.$$

.....E4

These three waves pass twice through the interface between the attenuator and the input section of the helix and undergo a small transmission loss equal to

$$TL = (1-\rho_2^2)$$

Also, since $\rho_3 = -\rho_2$, we have :

$$E_1'' = -A_{L1}\rho_1\rho_2(1-\rho_2^2)E.\exp\left[\beta_0 C\left(L_1(x_1-d_1)+L_{as}(x_{1a}-d_2)\right)\right].$$
$$.\exp\left[-j\beta_0\left(L_1(2-Cy_1)+L_{as}(2-Cy_{1a})\right)\right]$$

$$E_2'' = -A_{L2}\rho_1\rho_2(1-\rho_2^2)E.\exp\left[\beta_0 C\left(L_1(x_2-d_1)+L_{as}(x_{2a}-d_2)\right)\right].$$
$$.\exp\left[-j\beta_0\left(L_1(2-Cy_2)+L_{as}(2-Cy_{2a})\right)\right]$$

$$E_3'' = -A_{L3}\rho_1\rho_2(1-\rho_2^2)E.\exp\left[\beta_0 C\left(L_1(x_3-d_1)+L_{as}(x_{3a}-d_2)\right)\right].$$
$$.\exp\left[-j\beta_0\left(L_1(2-Cy_3)+L_{as}(2-Cy_{3a})\right)\right]$$

.....E5

The three waves are also reflected from the output port and return to the input where they are again reflected to rejoin the input wave. These can be expressed as follows :

$$E_1''' = A_{L1}\rho_1\rho_4(1-\rho_2^2)^2E.\exp\left[\beta_0 C\left((L_1+L_2)(x_1-d_1)+L_{as}(x_{1a}-d_2)\right)\right].$$
$$.\exp\left[-j\beta_0\left((L_1+L_2)(2-Cy_1)+L_{as}(2-Cy_{1a})\right)\right]$$

$$E_2''' = A_{L2}\rho_1\rho_4(1-\rho_2^2)^2E.\exp\left[\beta_0 C\left((L_1+L_2)(x_2-d_1)+L_{as}(x_{2a}-d_2)\right)\right].$$
$$.\exp\left[-j\beta_0\left((L_1+L_2)(2-Cy_2)+L_{as}(2-Cy_{2a})\right)\right]$$

$$E_3''' = A_{L3}\rho_1\rho_4(1-\rho_2^2)^2 E.\exp\Big[\beta_0 C\Big((L_1+L_2)(x_3-d_1)+L_{as}(x_{3a}-d_2)\Big)\Big].$$
$$.\exp\Big[-j\beta_0\Big((L_1+L_2)(2-Cy_3)+L_{as}(2-Cy_{3a})\Big)\Big]$$

.....E6

Combining the contributions of the three reflected waves due to the gaining slow wave :

$$E_1'+E_1''+E_1''' = A_{L1}\rho_1 E.\exp\Big[\beta_0 CL_1(x_1-d_1)\Big].\Big[\exp\Big(-j\beta_0 L_1(1-Cy_1)\Big).\Big(\rho_2-$$
$$\rho_2(1-\rho_2^2).\exp\Big(\beta_0 CL_{as}(x_{1a}-d_2)\Big).\exp\Big(-j\beta_0 L_{as}(2-Cy_{1a})\Big)$$
$$+\rho_4(1-\rho_2^2)^2.\exp\Big[\beta_0 C\Big(L_2(x_1-d_1)+L_{as}(x_{1a}-d_2)\Big)\Big].$$
$$\exp\Big[-j\beta_0\Big(L_2(2-Cy_1)+L_{as}(2-Cy_{1a})\Big)\Big]\Big]$$

.....E7

Similarly combining the contributions of the three reflected waves due to the decaying slow wave :

$$E_2'+E_2''+E_2''' = A_{L2}\rho_1 E.\exp\Big[\beta_0 CL_1(x_2-d_1)\Big].\Big[\exp\Big(-j\beta_0 L_1(1-Cy_2)\Big).\Big(\rho_2-$$
$$\rho_2(1-\rho_2^2).\exp\Big(\beta_0 CL_{as}(x_{2a}-d_2)\Big).\exp\Big(-j\beta_0 L_{as}(2-Cy_{2a})\Big)$$
$$+\rho_4(1-\rho_2^2)^2.\exp\Big[\beta_0 C\Big(L_2(x_2-d_1)+L_{as}(x_{2a}-d_2)\Big)\Big].$$
$$\exp\Big[-j\beta_0\Big(L_2(2-Cy_2)+L_{as}(2-Cy_{2a})\Big)\Big]\Big]$$

.....E8

Combining the contributions from the three reflected waves due to the fast wave :

$$E_3' + E_3'' + E_3''' = A_{L3}\rho_1 E.\exp\left[\beta_0 C L_1 (x_3 - d_1)\right].\left[\exp\left(-j\beta_0 L_1 (1 - Cy_3)\right).\left(\rho_2 - \rho_2(1-\rho_2^2).\exp\left(\beta_0 C L_{as}(x_{3a} - d_2)\right).\exp\left(-j\beta_0 L_{as}(2 - Cy_{3a})\right) + \rho_4(1-\rho_2^2)^2.\exp\left[\beta_0 C\left(L_2(x_3 - d_1) + L_{as}(x_{3a} - d_2)\right)\right].\exp\left[-j\beta_0\left(L_2(2 - Cy_3) + L_{as}(2 - Cy_{3a})\right)\right]\right]$$

.....E9

The overall feedback signal is then the sum of the contributions of all the reflected signals recombining at the input :

$$E_f = (E_1' + E_1'' + E_1''') + (E_2' + E_2'' + E_2''') + (E_3' + E_3'' + E_3''')$$

.....E10

The feedback signal combines with the input signal, modifying the gain of the TWT. Because of the large amount of phase shift in the feedback signal relative to the input , this combination with the input signal leads to ripple in the gain-frequency characteristic of the TWT. The magnitude of the gain ripple is dependent on the magnitude of the feedback signal, while the periodicity is determined by the signal delay in the slow-wave structure.

In terms of classic feedback amplifier theory the gain of an amplifier with feedback is given by :

$$A' = \frac{A}{1 + bA}$$

.....E11

If the TWT is regarded as an amplifier with feedback then the portion Ef of the signal reaching the input is proportional to bA. In fact,

$$bA = \frac{E_f}{E}$$

.....E12

where E is the input stimulus. If the real part of bA reaches a value of -1 and the frequency is such that the imaginary part of bA is zero, then the gain of the TWT will be practically infinite and it will verge on instability. If Re(bA) is less than -1 then conditions for oscillation will be satisfied periodically in the frequency band wherever Im(bA) falls to zero.

The magnitude of the gaining slow wave at the output of the TWT can be given as :

$$E_1'''' = A_{L1}\sqrt{(1-\rho_1^2)(1-\rho_4^2)}(1-\rho_2^2)\frac{E}{1+bA}.\exp\Big[\beta_0 C\Big((L_1+L_2)(x_1-d_1) + L_{as}(x_{1a}-d_2)\Big)\Big].\exp\Big[-j\beta_0\Big((L_1+L_2)(2-Cy_1)+L_{as}(2-Cy_{1a})\Big)\Big]$$

.....E13

Similarly, the magnitudes of the decaying slow wave and the fast wave at the TWT output can be expressed respectively as :

$$E_2'''' = A_{L2}\sqrt{(1-\rho_1^2)(1-\rho_4^2)}(1-\rho_2^2)\frac{E}{1+bA}.\exp\Big[\beta_0 C\Big((L_1+L_2)(x_2-d_1) + L_{as}(x_{2a}-d_2)\Big)\Big].\exp\Big[-j\beta_0\Big((L_1+L_2)(2-Cy_2)+L_{as}(2-Cy_{2a})\Big)\Big]$$

.....E14

$$E_3'''' = A_{L3}\sqrt{(1-\rho_1^2)\,(1-\rho_4^2)}\,(1-\rho_2^2)\,\frac{E}{1+bA}\cdot\exp\Big[\beta_0 C\Big((L_1+L_2)\,(x_3-d_1) + L_{as}(x_{3a}-d_2)\Big)\Big]\cdot\exp\Big[-j\beta_0\Big((L_1+L_2)\,(2-Cy_3)+L_{as}(2-Cy_{3a})\Big)\Big]$$

.....E15

The output signal is the sum of these three signals :

$$E_{out} = E_1'''' + E_2'''' + E_3''''$$

.....E16

The decibel gain of the tube can be given as :

$$G_{ss}(dB) = 10\log\left(\frac{E_{out}\cdot E_{out}^*}{E^2}\right)$$

.....E17

Shown in Fig.E-2 are the real and imaginary feedback signal magnitudes, Re(bA) and Im(bA), for the TWT for a 4500V 35mA beam for frequencies between 5 and 6GHz. The magnitude of Re(bA) does not fall below -0.6 and the tube is stable. In Fig.E-3 the ripple in the gain characteristic can easily be seen. The ripple is quite severe because of the considerable amount of feedback.

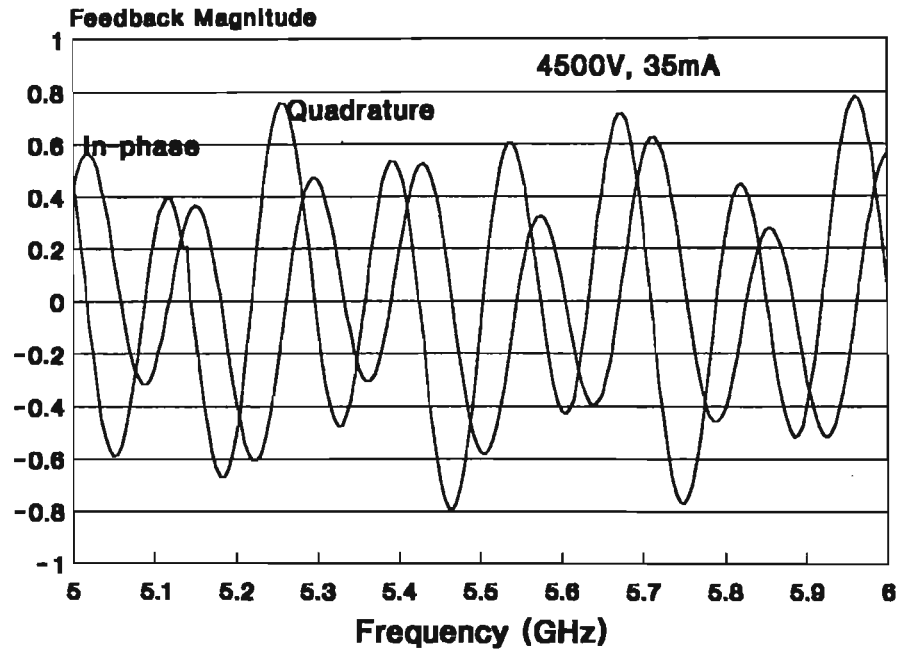

Fig E-2 : Internal feedback for 4500V beam

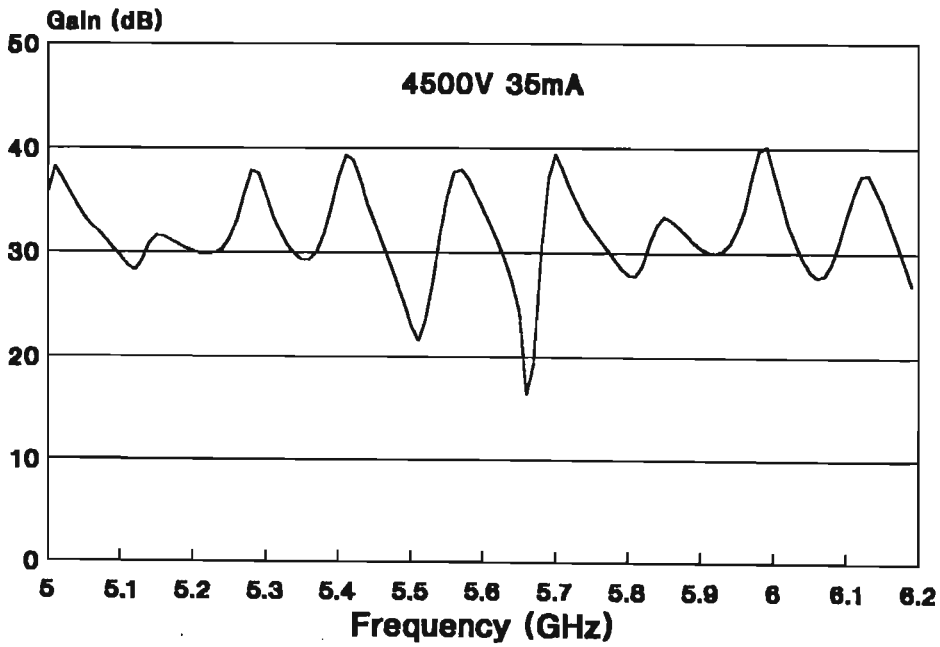

Fig E-3 : Gain ripple for 4500V 35mA beam

LIST OF REFERENCES

[1] Kompfner, R, "Travelling-wave valve - new amplifier for centimetric wavelengths",*Wireless World,* vol.52, pp369-372, November, 1946

[2] Staprans, A, *Linear Beam Tubes*, ch.22 of *Radar Technology*, E Brookner(ed.), Artech House, Dedham, Mass.,1977

[3] Skolnik, M I, *Introduction to Radar Systems*, McGraw-Hill Kogakusha Ltd, Tokyo,1980 pp.206-208

[4] Skolnik, M I, *Introduction to Radar Systems*, McGraw-Hill Kogakusha Ltd, Tokyo,1980 ch.11, pp.420-434

[5] Siemens Data Book, *Travelling-Wave Tubes*, 1986/1987, pp.183-234

[6] Siemens Data Book, *Travelling-Wave Tubes*, 1986/1987, pp.95-130

[7] Skolnik, M I, *Introduction to Radar Systems*, McGraw-Hill Kogakusha Ltd, Tokyo,1980 pp.206

[8] Pierce, J R, *Travelling Wave Tubes*, New York : Van Nostrand, 1950, p.1

[9] Vassilopoulos, N,"The Development of an Experimental Low Profile, Broadband Travelling Wave Tube Amplifier,"Ph.D Thesis,University of Natal, unpublished

[10] Foulis, B D, "A Gridless, Variable Perveance, Pierce Electron Gun," Ph.D.Thesis, University of Natal, unpublished

[11] Hutter, R G E, *Beam and Wave Electronics in Microwave Tubes,* New York : van Nostrand, 1965, p.188

[12] Pierce, J R, *Travelling Wave Tubes*, New York : Van Nostrand, 1950, p.134

[13] Pierce, J R, *Travelling Wave Tubes*, New York : Van Nostrand, 1950, p.135

[14] Gilmour,A S,Jnr, Gillette,M R, Chen,J-T "Theoretical and Experimental TWT Helix Loss Determination", *IEEE Transactions on Electron Devices,* Vol. ED-26, No.10, p.1582, Oct 1979

[15] Hutter, R G E, *Beam and Wave Electronics in Microwave Tubes,* New York : van Nostrand, 1965, p.121

[16] Jain,P K, Murty,K V R, Joshi,S N, Basu, B N, "Effect of Finite Thickness of the Helix Wire on the Characteristics of the Helical Slow-Wave Structure of a Travelling-Wave Tube", *IEEE Transactions on Electron Devices,* Vol. ED-34, No.5, p.1210, May 1987

[17] Jain,P K, Basu, B N, "The Inhomogeneous Loading Effects of Practical Dielectric Supports for the Helical Slow-Wave Structure of a TWT", *IEEE Transactions on Electron Devices,* Vol. ED-34, No.12, pp.2643-2648, Dec 1987

[18] Gilmour,A S,Jnr, Gillette,M R, Chen,J-T "Theoretical and Experimental TWT Helix Loss Determination", *IEEE Transactions on Electron Devices, Vol. ED-26, No.10, p.1583,* Oct 1979

[19] Jain,P K, Basu, B N, "The Effect of Conductivity Losses on Propagation Through the Helical Slow-Wave Structure of a Travelling-Wave Tube", *IEEE Transactions on Electron Devices,* Vol. ED-35, No.4, pp.549-558, April 1988

[20] Hutter, R G E, *Beam and Wave Electronics in Microwave Tubes,* New York : van Nostrand, 1965, p.193

[21] Pierce, J R, *Travelling Wave Tubes*, New York : Van Nostrand, 1950, pp.20,27

[22] Pierce, J R, *Travelling Wave Tubes*, New York : Van Nostrand, 1950, pp.17-23

[23] Tien, P K, "Travelling-Wave Tube Helix Impedance", *Proc IRE*, Nov 1953, pp.1617-1623

[24] Singh, V P, Murty, K V R, Basu, B N, "Interaction Impedance from the Equivalent Circuit Parameters of a Dielectric-Loaded Helical Slow-Wave Structure of a Travelling-Wave Tube", *IEEE Transactions on Electron Devices*, Vol. 35, No 4, April 1988, pp. 563-566.

[25] Jain, P K, Basu, B N, "A Theory of the Attenuator-Coated Helical Slow-Wave Structure of a Travelling-Wave Tube", *IEEE Transactions on*

Electron Devices, Vol 35, No 10, October 1988, pp.1750-1757

[26] Pierce, J R, *Travelling Wave Tubes*, New York : Van Nostrand, 1950, Appendix II, pp.229-232

[27] Hutter, R G E, *Beam and Wave Electronics in Microwave Tubes*, New York : van Nostrand, 1965, p.201

[28] Hutter, R G E, *Beam and Wave Electronics in Microwave Tubes*, New York : van Nostrand, 1965, p.163

[29] Hutter, R G E, *Beam and Wave Electronics in Microwave Tubes*, New York : van Nostrand, 1965, pp.168-169

[30] Branch, G M,& Mihran, T G,"Plasma Frequency Reduction Factors in Electron Beams", *IRE Trans.*, Vol. ED-2, 1955, pp. 3-11

[31] Hutter, R G E, *Beam and Wave Electronics in Microwave Tubes*, New York : van Nostrand, 1965, p.209

[32] Hutter, R G E, *Beam and Wave Electronics in Microwave Tubes*, New York : van Nostrand, 1965, p.194

[33] Pierce, J R, *Travelling Wave Tubes*, New York : Van Nostrand, 1950, p.120

[34] Hutter, R G E, *Beam and Wave Electronics in Microwave Tubes*, New York : van Nostrand, 1965, pp.194-197

[35] Hutter, R G E, *Beam and Wave Electronics in Microwave Tubes*, New York : van Nostrand, 1965, p.197

[36] Basu, B N,"Equivalent circuit analysis of a dielectric-supported helix in a metal shell", *Int.J.Electronics*, 1979, Vol 47, No 3, pp 311-314

[37] Ramo, S, Whinnery, J R, & van Duzer, T, *Fields and Waves in Communication Electronics*, John Wiley & Sons, N York, 1965, pp 303-304

[38] Ramo, S, Whinnery, J R, & van Duzer, T, *Fields and Waves in Communication Electronics*, John Wiley & Sons, N York, 1965, pp 186-188

[39] Everitt, W L, & Anner, G E, *Communication Engineering*, McGraw-Hill, N York, 1956, p 480

[40] Gittins, J F, "Power Travelling-Wave Tubes", English Universities Press, London, 1964, p 90

[41] *Handbook of Mathematical Functions*, Ed. Abramowitz,M & Stegun,I A, Dover Publications, New York, 1965, pp.15,378-379

[42] Hansen,J S,(with Lange,G A, Rostad,A S & Woods,R L) "System Aspects of Communications TWTAs", *Hughes Aircraft Company Electron Dynamics Division Application Note*, August 1982

[43] Belohoubek,E F,"Helix support structure for ultra-wideband travelling-wave tubes", *RCA Rev.*, Vol.26,pp. 106-117, 1965

[44] Stokes, A W, "Magnetic Focusing of Electron Beams for Linear Beam Tubes", M.Sc. Thesis, University of Natal, July 1990

[45] Hutter, R G E, *Beam and Wave Electronics in Microwave Tubes*, New York : van Nostrand, 1965, p.184

[46] Hutter, R G E, *Beam and Wave Electronics in Microwave Tubes*, New York : van Nostrand, 1965, p.206]

[47] Hutter, R G E, *Beam and Wave Electronics in Microwave Tubes*, New York : van Nostrand, 1965, p.205

[48] Hutter, R G E, *Beam and Wave Electronics in Microwave Tubes*, New York : van Nostrand, 1965, p.204

[49] Jain,P K, Basu, B N, "The Inhomogeneous Dielectric Loading Effects of Practical Helix Supports on the Interaction Impedance of the Slow-Wave Structure of a TWT", *IEEE Transactions on Electron Devices*, Vol. ED-39, No.3, pp.727-733, March 1992